Radial Turbine - Diffuser Interaction

Effect of tip gap

Luis Matabuena

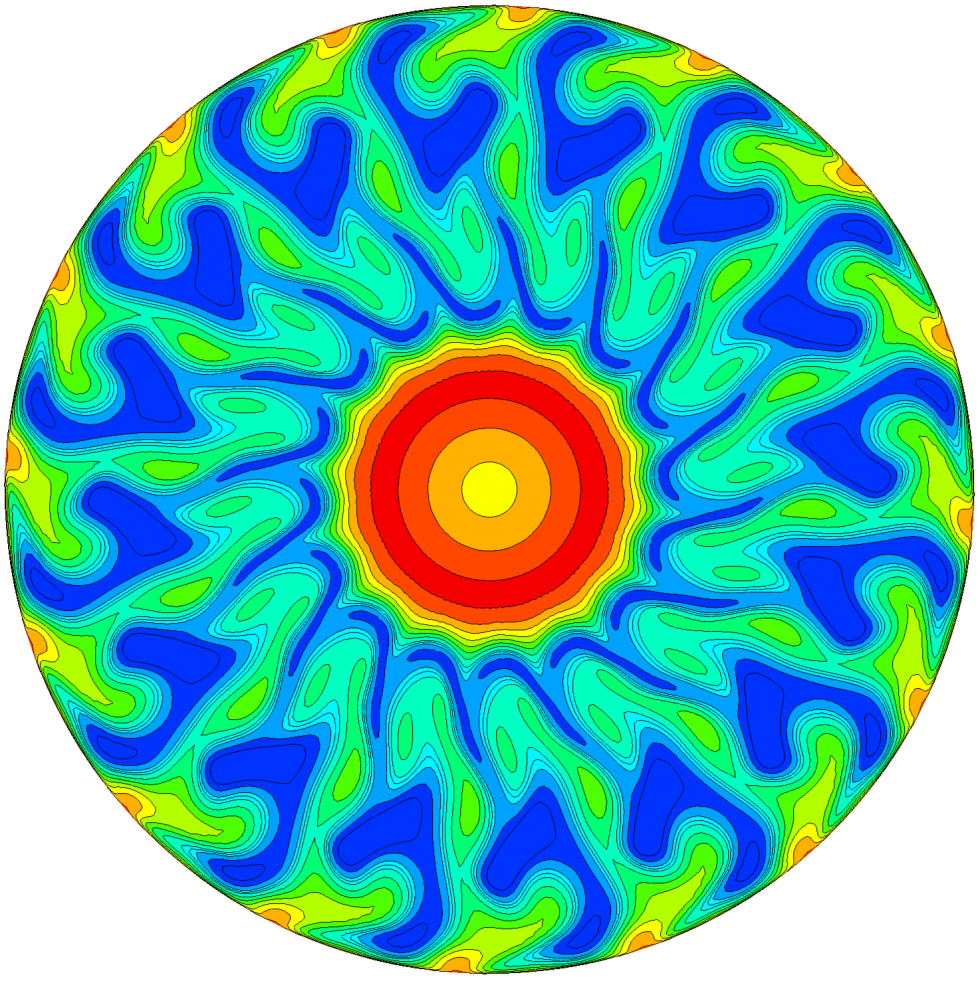

TU Delft

Radial Turbine - Diffuser Interaction

Effect of tip gap

Thesis report

by

Luis Matabuena

to obtain the degree of Master of Science
at the Delft University of Technology
to be defended publicly on August 25^{th}, 2023 at 14:00

Thesis committee:	
Chair:	Prof.dr.ir Piero Colonna
Supervisors:	Dr. Matteo Pini
	Matteo Majer
External examiner:	Dr. Richard P. Dwight
Place:	Lecture Hall B, Faculty of Aerospace Engineering, Delft
Project Duration:	September, 2022 - July, 2023
Student number:	5610338

An electronic version of this thesis is available at `http://repository.tudelft.nl/`.

Faculty of Aerospace Engineering · Delft University of Technology

Copyright © Luis Matabuena, 2023
All rights reserved.

Abstract

This document contains the final Master Thesis Report to obtain the Master of Science on Aerospace Engineering (Flight Performance & Propulsion - Propulsion & Power) at the Delft University of Technology. The research work characterises the interaction of a radial inlet turbine with a downstream diffuser through the size of the rotor tip gaps.

In the implementation of power turbines it is common to add a diffuser downstream of it to lower the rotor exhaust pressure and thus increase power extraction for the same boundary conditions. However, diffusers are bulky and take a lot of space in the assembly. This lowers the power density of the machine, increases installation weight in transport applications, and installation costs in ground based operations. Researchers noticed that the non-dimensional static pressure recovery (C_p) of this device was higher when operating downstream of a turbine than with uniform inlet conditions. The publications in this field are relatively scarce, and thus there is a knowledge gap with immediate practical application.

Some researchers have focused on the interaction of turbine vortical structures with the boundary layer of the diffuser. They have found out that under this conditions the boundary layer can support steeper pressure gradients without detaching. This is only applicable to very aggressive diffusers that would stall in isolation. Notably, all the publications in this field deal with axial machines, and, as the current study will show, the situation changes considerably when applying the theory to radial turbines.

This work studies another side of the problem. The research focuses on stable diffusers, and thus there is no boundary layer that needs reinforcement. Turbine rotor tip gaps generate an increase of entropy and reduce turbine power generation. However, these gaps also cast powerful vortexes that affect the diffuser flowfield. This project studies the effect of the tip gap configuration on the pressure recovery of the diffuser, in order to better understand the trade-offs and support the design process. Tip gap sizes are usually determined from mechanical constraints. This work provides insight into the real cost of a tip gap by analysing the assembly turbine + diffuser, and thus it guides the designer into where to focus his efforts when working with these constraints.

The general conclusion of the project is that there is a range of tip gap sizes where the performance of the diffuser in enhanced. In this range, the performance cost in the rotor for increasing the tip gaps is partially compensated by a better pressure recovery in the diffuser. Furthermore, it has been discovered that in a radial turbine the leading edge tip gap (axial) is more influential than the trailing edge (radial) one. This information will guide engineers when choosing the bearings for the machine and dealing with design trade-offs.

Moreover, a novel study in radial turbine flow structures is carried out. Not a lot is known about the vortical structures in these machines, and this work provides a first qualitative description about origin and behaviour of this vortexes. Different flow modes are identified and related to simple parameters available in 0D designs. The combination of this information with previous tip gap flow models, and diffuser-vortex interaction models, will allow the obtention of improved losses models including the effect of the diffuser from the conceptual design stage. This work not only provides useful design guidelines, but also sets down the basis for future research leading to a better understanding and modelling of radial inflow turbines.

Acknowledgements

There is a lot of people that comes to mind when finishing such an important period in my education. From high-school teachers, to professors in every stage of my university period, and , of course, all the way through all of those friends and amazing people I have met along the process. They will be always in my mind and, I hope, also in my life.

In the elaboration of this work the involvement of TUDelft's Aerospace Faculty Turbomachinery group has been invaluable, specially the labor of **Matteo Majer**. He was always available and helping me to keep in track with the project (I can only hope someone can take a look at all of those interesting side-lines that appeared along the way). Without his regular feedback, and all the other punctual inputs from the group, this thesis wouldn't have achieved this quality. There must be also a mention to TUDelft HPC *DelftBlue* team, which was very involved in everything they could assist me with and made possible this project.

I would like to mention all the friends that support me along this journey. Those that I left in Madrid and I feel as close as two years ago, and those new ones that came along in Delft. There is an especial place among them to **Charo**, who has been at my side for the hardest period in my studies.

The last mention is, how could it be otherwise, to my **parents** and **sister**. They gave me all the tools that have brought me here, the passion for learning, the attention to detail, the curiosity that drives me...

Gracias mamá, gracias papá. No estaría aquí sin vosotros.

Contents

Nomenclature

Abbreviations

Abbreviation	Definition
AR	Area Ratio
B	Blockage parameter
CFD	Computational Fluid Dynamics
HPC	High Performance Computer
HSV	Horse-Shoe Vortex
LE	Leading Edge
LES	Large Eddy Simulation
RANS	Reynolds Averaged Navier-Stokes
RIT	Radial Inflow Turbine
SAS	Scale Adaptive Simulation
SST	Shear Stress Transport
TE	Trailing Edge
UIM	Unified Integral Method
URANS	Unsteady Reynolds Averaged Navier-Stokes

Symbols

Symbol	Definition
C_p	Pressure Coefficient
$C_{p,id}$	Loss Coefficient
C_p^*	Kinetic Energy Coefficient
C_p^{**}	Maximum C_p for a given length
k_{loss}	Maximum C_p for a given AR
ξ	Kinetic Energy Coefficient
ξ_{NU}	Non-uniform Kinetic Energy Coefficient
ξ_{bulk}; ξ_B	Bulk Kinetic Energy Coefficient
α	Kinetic-Energy-flux velocity-profile
δ^*	Boundary Layer displacement thickness
A_{eff}	Diffuser Effective Area
Σ	Stabilization Coefficient
$\vec{omega}$	Vorticity
γ	Metal blade angle / Specific heat capacity ratio
ϵ	Tip Gap Size
ϵ_{Avr}	Average Tip Gap Size
Δ_ϵ	Percentage change of Tip Gap Size
ϵ_{LE}	Leading Edge Tip Gap Size
ϵ_{TE}	Trailing Edge Tip Gap Size

Symbol	Definition
t	Blade thickness
R	Pressure to scraping parameter
λ	Tip Gap aspect ratio
λ^*; λ_{crit}	Critical Tip Gap aspect ratio
Re	Reynolds Number
M	Mach Number
β_{tt}	Total to total Pressure Ratio
β_{ts}	Total to static Pressure Ratio
β^T	Turbine Pressure Ratio
β^{Sys}	Flange to Flange Pressure Ratio

List of Figures

List of Tables

Introduction

A *turbomachine* is a device in which energy is transferred to or from a fluid by the dynamic action (*work*) of one or more *rotating* blades[1]. A turbine is a kind of *Turbomachine* that extracts energy from a stream of fluid. These devices are very important technological elements due to their presence in most energy systems, as for example marine and aeronautical propulsion systems, ground-based power generation, or even power recovery systems in common vehicles, such as turbocharged cars. For this reason enhancing their performance and affordability is of utmost importance to make fossil-fuel energy systems greener, as well as boosting the diffusion of renewable technologies.

There are several kinds of turbines, and they are usually classified with respect to their geometry. It is possible to find *axial turbines*, where the working fluid always flows parallel to the rotation axis; *radial inflow turbines* (RIT), where the flow enters the device inwards and perpendicular to the rotation axis (i.e. radially) and exits in the axial direction; and *mixed flow turbines*, a compromise between the previous two. The investigation that follows regards RITs.

The relevance of these devices results in a number of techniques to improve system performance. One of these is the usage of a diffuser downstream of the turbine. A diffuser is an increasing cross section pipe whose effect on the flow is to decelerate it and thus produce a static pressure raise. It increases turbine power output for a given static back pressure because it allows to achieve lower pressures at the rotor outlet. This increases the pressure ratio across the machine, and thus improves power extraction for the same system boundary conditions. Note that the usage of a diffuser only leads to a net gain when the objective of the whole *system* is shaft-power generation and there is no need of *kinetic energy* downstream of the turbine. This is the case of a *power turbine* in a turbo-shaft, an auxiliary power unit (APU), or a ground-based power generation gas turbine.

Furthermore, it has been shown that it is possible to enhance diffuser performance by a proper matching with the turbine outflow. Fariokhi (1987, [2]) and Willinger et Al. (1998, [3]), for instance, investigated by different methods the effect of non-uniform flows on the diffuser and the performance cost of generating them with an axial turbine; or Sieker et Al. (2008, [4][5]) and Mimic [6] carried out experimental, numerical and theoretical studies of the performance of an annular diffuser downstream of an axial turbine. This last group proves that the main interaction mechanism is due to vortexes casted at the tip of the blades. The general conclusion is that turbine outflow can effectively improve diffuser performance, but overall system efficiency is decreased. However, the interaction with a RIT has never been studied before. Additionally, there are no reliable methods to predict the effect of a general turbine on the diffuser during the conceptual design stage. The closest tool is the one in [6], and it only applies to off-design behaviour of a single turbine design. This research work intends to obtain the knowledge required to eventually lead to such a generalised method, in the context of Radial Inflow Turbines:

> *The primary objective of this research project is* ***to characterize the interaction of a radial inflow turbine with a downstream unstalled conical diffuser through tip-gap-related flow structures.***

This will be achieved by answering the following research questions:

1. What is the potential impact of a diffuser in turbine work extraction, and under which conditions is this device more relevant?
2. Which is the simplest set-up able to capture realistic diffuser flow-fields and integral performance?
3. What is the effect of tip gap size and distribution on the integral performance of the diffuser?
4. What is the physical interaction mechanism between turbine and diffuser?

[1] *turbo*, from Latin *turbinis* means ”that spins” or ”that swirls” [1]

1 Literature Review

1.1. Diffuser Technology

Diffusers have been investigated for a long time, the first reported usage dating back from the roman empire [7]. They have clear practical industrial applications, but they are also the simplest set up providing an adverse pressure ratio. This makes them wide spread devices, and the understanding of the basic phenomena is quite advanced.

There are several types of diffusers: *planar* or 2D diffusers (a channel with two parallel walls and two diverging walls), *conical* diffusers (a hollow frustum of cone), and *annular* diffusers (a short of conical diffuser with a blocking element in the middle, resulting in an annular flow-path). In the following, the discussion will be directed mostly towards conical diffusers. However, it is impossible to avoid introducing some references to 2D cases (mostly used for basic research) and annular diffusers (the most common one in the industry due to the morphology of the axial machines).

1.1.1. Diffuser Performance charts

Kline et Al. (1959, [8]) identified the basic geometrical parameters for conical diffusers were identified as: *area ratio*, AR, the *non-dimensional length*, L/D_1, and the *wall angle*, δ. AR is the only driver of the pressure recovery with idealised flows, and δ is a function of the other two parameters, Figure 1.1.

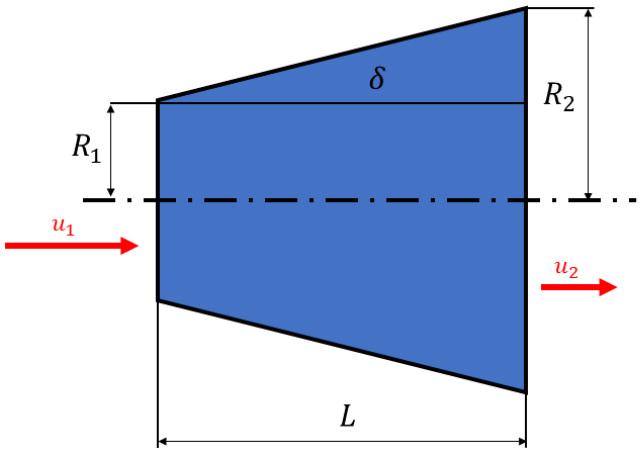

$$D_1 = 2R_1;\ D_2 = 2R_2$$

$$AR = \frac{A_2}{A_1} = \frac{D_2^2}{D_1^2}$$

$$\tan(\delta) = \frac{1}{2}\frac{\sqrt{AR} - 1}{L/D_1}$$

Figure 1.1: Basic parameters of a conical diffuser.

Furthermore, the performance of a diffuser is given through several non-dimensional coefficients:

$$C_p = \frac{P_2 - P_1}{P_{1t} - P_1} \tag{1.1}$$

$$k_{loss} = \frac{P_{1t} - P_{2t}}{P_{1t} - P_1} \tag{1.2}$$

The first one is the *pressure recovery coefficient*, and the second one is the *loss coefficient*. Note that the denominators of these expressions represent all the dynamic pressure, including compressibility effects and swirl. Some modern publications [9] include a *kinetic energy coefficient*:

$$\xi = \frac{P_{2t} - P_2}{P_{1t} - P_1} \tag{1.3}$$

in such a way that:

$$C_p + \xi + k_{loss} = 1 \tag{1.4}$$

This relation allows the discussion of the cause of low C_p both due to *inefficient* diffusion (losses, k_{loss}) and *insufficient* diffusion (ξ). This relation between coefficients is useful when analysing the evolution of the flow along the length of the device. At the inlet $\xi = 1$, $C_p = 0$ and $k_{loss} = 0$, and then ξ "converts" into the other performance coefficients.

Another commonly used metric is the diffuser effectiveness, ε (sometimes also represented by η, which is arguably misleading). This is defined as:

$$\varepsilon = \frac{C_p}{C_{p,id}} \tag{1.5}$$

where $C_{p,id}$ is an ideal reference. Usually it is taken as an isentropic, uniform, incompressible, non-swirling flow and then $C_{p,id} = 1 - \frac{1}{AR^2}$. However, the expression should be adapted to the relevant case including swirl and compressibility effects if needed. It is always assumed that the flow is *uniform* and isentropic. Note that it is possible to obtain $\varepsilon > 1$ [10], as it will be discussed in Section 2.1.

The first publication regarding diffuser performance dates back to Kline et al. (1959) [8]. They tested several planar diffusers and identified the different operation regimes. These are *fully attached flow*, *transitory stall*, *stable stall* and *jet flow*, Figure 1.2. They also found that *optimal diffusers* are operating in the transitory stall regime.

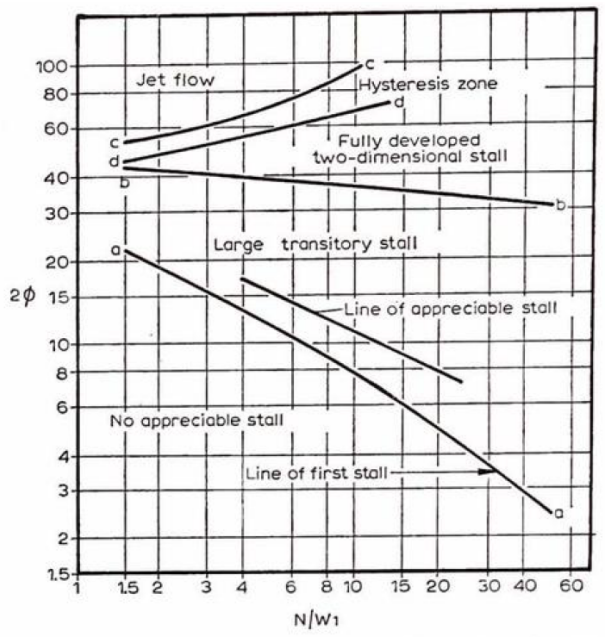

Figure 1.2: Different flow regimens for planar diffusers (Sovran & Klomp, 1967 [10]). N is the length of the diffuser and ϕ is the angle of the walls.

After them, Sovran (1967) [10] compiled and performed a considerable amount of experimental cases and crafted one of the first *performance charts* (an example is shown in Figure 1.3). These charts identify the locus of *optimal designs* as C_p^* (maximum pressure recovery for a given L/R_1) and C_p^{**} (Maximum pressure recovery for a given AR). These tests were performed with high Reynolds[1] number and low

[1]Based on the inlet diameter.

Mach number. It was determined that the effect of Reynolds number is negligible. The inlet conditions corresponded to naturally developed turbulent boundary layers through pipes. In addition, they provide a theoretical discussion about the effects of the blockage parameter B:

$$(1 - B_j) = \frac{A_{eff}}{A_j} \approx 1 - \frac{4\delta_j^*}{D_j} \tag{1.6}$$

where δ_j^* is the boundary layer displacement thickness at station j, and A_{eff} is the effective flow area such that $A_{eff} = \frac{\dot{m}}{\rho u_{max}}$. However, they do not test different inlet profiles, and thus the diffuser performance is characterized without fully including the effect of inlet conditions.

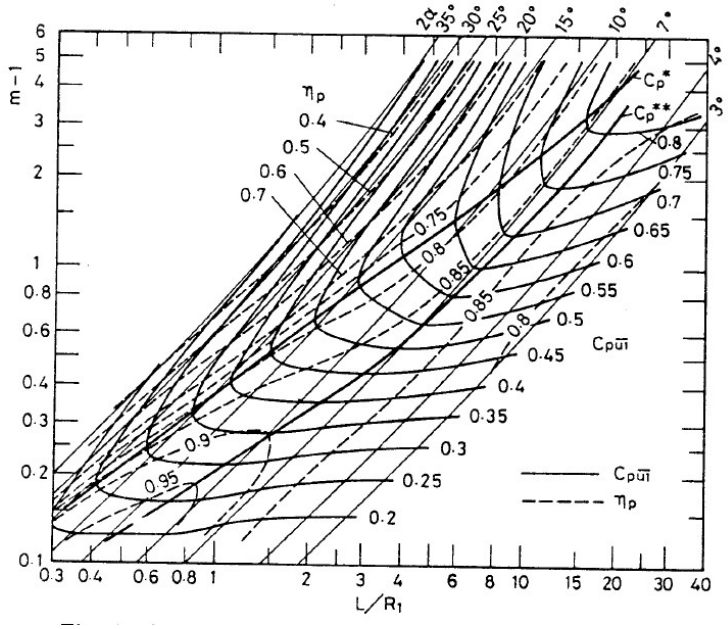

Figure 1.3: Performance chart for conical diffusers (Ishikawa & Kakamura 1989 [11]). Low turbulence intensity (0.5% at the core, 6% at the BL), low blockage ($B_1 = 0.04$): Almost uniform inlet conditions. m is the area ratio and α is the semi-cone angle.

During this early period higher turbulence levels were assumed to improve the performance[2], but there was no clear consensus regarding the blockage effect. Other authors discuss that turbulence level does not affect the locus of the optimal geometries in a chart as Figure 1.3, but it changes the C_p value (Sovran (1967, [10])). Although higher blockage is intuitively associated with thicker boundary layers closer to separation, Senoo & Nishi (1977, [13]) proved that higher blockage values limited the boundary layer growth and prevented separation. Nowadays it is known that blockage factor is a meaningful parameter only for similar velocity profiles, but this is not researched until years later.

The discussion about non-swirling, boundary-layer-like inlet conditions is closed by Ishikawa & Kakamura (1989, [11]). They address the inconsistency between the classical experimental results by conducting a comprehensive test campaign in conical diffusers with highly controlled inlet conditions. The differences between previous cases are attributed to turbulence intensity and inlet blockage. All of this early experimental knowledge, and several low order computation methods and augmentation techniques are summarized by Japikse in reference [7].

1.1.2. Additional Research on Diffusers

As the simple pipe-like flow inlet conditions were being understood, some publications modifying this inlet profile appeared. Usually it was in the context of augmentation methods. For instance, Nicoll & Ramaprian (1970, [14]) or Back & Cuffel (1982, [15]) investigated wall jets to reenergize the boundary layer. However,

[2]This idea was definitely proven by Stevens & Williams (1980 [12]), who experimentally isolated the effect of turbulence and found that higher turbulence intensity close to the walls can greatly improve C_p with only minor penalization in k_{loss}

some other authors investigated the importance of the turbine outflow and the wall-jet-like structures that arose (for instance Kruse et al. (1983, [16]) or Farokhi (1987, [2])). These studies focused on delaying boundary separation, and thus they concluded that performance improvements are more noticeable for diffusers in incipient stall conditions.

Some other publications explored the effect of swirl (Vassiliev et al. (2003, [17])), but this is usually done in the context of strut stall. The research group of Vassiliev continues with a numerical investigation of the impact of inlet conditions in diffuser performance [18]. It is concluded that the Reynolds number and total temperature profile do not affect diffuser performance. However, Mach number changes the effectiveness[3]. The total pressure and turbulence intensity radial profiles are the most influential parameters, and better performance is found with non-uniform flows. Swirl effects are difficult to asses, as they interact strongly with struts. However, it is noted that that in annular sections there is an optimal swirl: it can prevent detachment in the outer wall; but too much swirl will cause boundary layer separation at the inner wall. This will be explained by Seume & Sieker (2008, [5]): swirl can transport turbulent kinetic energy outwards. The conclusion is that moderated swirl enhances diffuser performance at a fixed inlet turbulence intensity. However, there is not a method to predict the maximum amount of swirl allowable.

In the last years the *Department of Turbomachinery and Fluid Dynamics*, in Leibniz University Hannover, is the most active group researching non-uniform inlets and turbine-diffuser interaction. With several publications ([4][5][6][9][19][20][21]) they experimentally, numerically and theoretically investigate the effect of realistic axial turbine outflows including wakes, vortexes, and swirl. Their results are presented in Section 1.2.

1.1.3. Diffuser Augmentation Methods

There has been several attempts throughout the years to achieve shorter diffusers with better performance. Additionally, a diffuser produces a relatively simple flow suitable for testing novel flow control concepts. This implies that there is a great amount of publications treating the topic of diffuser augmentation. The main objective is to achieve steeper pressure gradients while keeping the boundary layer attached. The main methods are the following [7]:

- **Boundary layer suction:** By suctioning (and thus removing) the boundary layer it is possible to avoid stall. There has been multiple research lines about suctioning the boundary layer both at the inlet or somewhere inside the diffuser. This method is effective, but it has not found a lot of practical application due to the added complexity[4].
- **Wall jet injection:** In this methods the boundary layer is *re-energised* by injecting a high energy jet close to the wall. The performance of the diffuser can be doubled (including the pumping power) by these techniques [14]. These methods have not found direct practical implementations, but some researchers have used these data sets to model the effect of the turbine tip gap leakage flow [2].
- **Ribs & fins:** These methods attach protrusions to the walls or create annular chambers causing small recirculation bubbles. It is though that these controlled separations substitute a large, full-scale boundary layer detachment, and thus improve performance in the region of transitory stall (Figure 1.2).
- **Flowfield inserts:** Some researchers block the diffuser flow-path both totally or partially with screens. These increase turbulence intensity and make the flow more uniform. These methods allow the control of the flowfield in the diffuser, but this causes high of total pressure losses. They are applied in basic research experimental installations, but they have not found an industrial application.
- **Surface treatments:** Under this topic there are two techniques: Adding *roughness* to the walls and introducing *vortex generators*. The first method changes the boundary layer structure and can modify the separation point. The usage of vortex generators shows a great increase in performance [24]. This technique is very relevant for this thesis, as turbine tip gap vortexes are the primary interaction mechanism between turbine and diffuser[6].

Most investigations about vortexes in diffusers [24][25] use traditional vortex generators as those

[3] The changes in effectiveness with Mach number are due to $C_{p,id}$ increasing slightly while C_p is practically constant.

[4] A side line of this research is the so called *Vortex controlled diffusers* [7][22][23]. These diffusers use suction to create a controlled vortex in the corners of a sudden expansion. Effectively, this creates a ”fluid wall” and allows for better performance in the diffusion process. Although this has not found practical applications, the author of this text thinks that this concept might be interesting if the flowfield at the hub of the turbine is to be improved (Section 5.2).

implemented for external aerodynamics. These studies found that counterrotating pairs of vortexes are more effective, and that the spacing between the vortex generators is an important parameter.

Another way of obtaining coherent vortexes is by the use of plasma actuators. Grundmann et Al. (2011, [26]) evaluated the effect of different vortical structures in a diffuser. They tested both annular and axial vortexes, and they found that in their case axial vortexes were more efficient. They attributed this to the mass flow entrainment. However, they also report that their axial vortexes were stronger than the annular ones due to the experimental set up, so the comparison is not totally equivalent. The vortical structures found in turbine outflows have both axial and circumferential components due to the outlet swirl angle.

1.2. Turbine-Diffuser Interaction

The literature about turbine diffuser interaction is scarce and it only deals with axial machines. Even tough the concepts are analogous for radial and axial machines, the flow structures are completely different, and thus the generality of the results is not clear.

The first work on this is by Farokhi (1987, [2]). They did an analytical study of the effects of an unshrouded last stage in an axial low pressure turbine (LPT) ahead of the diffuser. Rotor losses will grow with increasing tip gaps, but diffuser performance will be also enhanced. They used experimental data from diffusers with wall jet injection, and tip gap loss models for axial turbines. They theoretically derive the effect of diffuser performance on turbine power extraction and thus they link these two effects. The conclusion is that the loss in efficiency due to the tip losses always outweights the gain by diffuser enhancement. Farokhi continues this research with CFD methods (Blanco et al. 2014 [27]), and highlights the necessity of retaining pitch-wise flow structures to correctly capture the interaction with the diffuser.

Willinger & Haselbacher (1998 [3]) also made some work on this topic. They used a wind tunnel to test a linear cascade with different tip gaps. They extract cascade performance data and the flowfield from the experimental set up. Then, this is used as the boundary condition for a CFD computation ($k-\varepsilon$ RANS) of a typical industrial diffuser. They find out that for practical tip gap sizes ($1-4$% of the chord), the performance of the assembly does not change: the diffuser compensates for extra losses in the rotor. However, the tip gap flow structure is affected by the scraping effects due to the relative motion of the casing, so the results of the linear cascade cannot be generalized to rotating cascades.

The active work in this field by the Leibniz group ([4][5][6][9][19][20][21]) has already been introduced in Section 1.1 . The experimental test rig mentioned consists on a motorized wheel where they can mount cylinders or blades (Figure 1.4). The inlet to this wheel allows controlling the swirl angle. Downstream of this assembly they have an annular diffuser that converts into conical after suddenly removing the middle section. Their first work on the topic studies the blockage effect of wakes without any other effect as blade loading or tip vortexes. To achieve this, they use the wheel with cylinders (Figure 1.4). They find out that for rotation speeds higher than 1000 rpm the diffuser with the spoke wheel performs better than without it. This effect is mainly attributed to the *interaction* of swirl with the turbulent wakes. Higher rotational speed increases swirl too much and the recirculation zone downstream of the sudden expansion induces too much blockage. The following publications include the more realistic effect of blades. They use symmetrical airfoils (NACA 0020) with twist distribution such that at design conditions all the blade is unloaded (Figure 1.4). For high rotational speeds the rotor behaves as a compressor and for low ones as a turbine[5]. They find great changes in performance when the blade is loaded, what makes them conclude that *it is the tip vortex what mostly affects the performance of the diffuser and the swirl is just a transport agent*. They also find out that this effect is beneficial for turbine outflows, but not for compressors. They also study the vortex formation process and discover that it is highly unsteady: the same blade can cast or not a coherent vortex, and they always observed less vortexes than blades, the ratio of these not being a whole number. For this reason they conclude that one blade passage steady simulations might not be enough to capture all the phenomenology. However they don't investigate further the origin of these asymmetry and there is not enough information to deduce the flow pattern upstream of the rotor. Finally, it is pointed out that turbulence in the wake region is not isotropic, as usually assumed by numerical models. The effects of this are not investigated.

The next set of publications, those by Mimic et al., are summarised in a PhD thesis [6]. They develop

[5]This behaviour is related to the fact that in this study mass flow is fixed. The axial velocity is always the same, and thus changing the rotational speed directly changes the incidence angle to the blades.

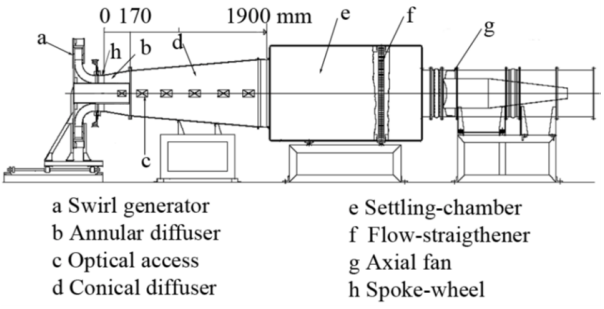

a) Experimental test rig to study turbine-diffuser interaction.

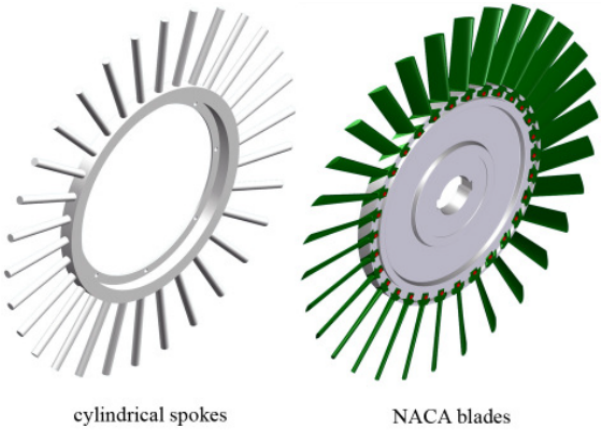

b) Different wheels tested in the papers.

Figure 1.4: Experimental set up in Leibniz University[5].

a parameter to characterize the vortex effect based on stage design parameters. This parameter is the *stabilization number*, $\Sigma = \frac{\psi f}{\phi^2}$. In this expression f is the reduced frequency and it is related to number of blades and rotational speed, ψ is the loading coefficient, and ϕ is the flow coefficient. They correlate experimental C_p and k_{loss} changes with this parameter, proving that indeed it is the tip vortex due to blade loading what stabilises the diffuser. However, they point out that their correlation is not universal and could be extremely dependent on the exact turbine. In their last publication they expand the results to different diffuser angles, showing that the correlation they obtain can be applied to different diffuser designs (with the same turbine). They also find out that steeper diffusers are more sensitive to this Σ. CFD computations are performed with SST-SAS models (Section 3.2). They are not able to numerically predict the value of C_p, but the ΔC_p due to Σ changes is correctly captured in every case. Finally, they provide a chart that can modify the typical performance maps to take into account the effect of the turbine on that diffuser. Presumably this chart is turbine dependent, and that dependency is unknown. They also provided the interaction model discussed in Section 3.2.

2

Theoretical Basis

2.1. Diffuser Performance Metrics

The basic performance metrics and diffuser flow characteristics were introduced in Section 1.1.1. These are:

$$C_p = \frac{P_2 - P_1}{P_{1t} - P_1}$$

$$K_{loss} = \frac{P_{1t} - P_{2t}}{P_{1t} - P_1}$$

$$\xi = \frac{P_{2t} - P_2}{P_{1t} - P_1}$$

$$C_p + k_{loss} + \xi = 1$$

Respectively, pressure coefficient, loss coefficient, and kinetic energy coefficient.

For the shake of completeness, the expressions of ideal C_p are given here. Under the assumption of incompressible flow, mass continuity gives $u_1 A_1 = u_2 A_2 \rightarrow AR = \frac{A_2}{A_1} = \frac{u_1}{u_2}$. Assuming no total pressure losses and using $P_t = P + \frac{1}{2}\rho u^2$:

$$C_{p,id} = \frac{P_2 - P_1}{P_{1t} - P_1} = 1 - \frac{1}{AR^2} \tag{2.1}$$

Another kind of (idealized) diffusion process is a sudden expansion with mixing [28]. In this case there will be total pressure losses, so an extra equation is needed: second Newton's law, $F = \frac{\Delta p}{\Delta t} \rightarrow A_2(P_1 - P_2) = u_2 \rho u_2 A_2 - u_1 \rho u_1 A_1$. Using this, and the previous considerations about mass continuity, it is obtained:

$$C_{p,exp} = \left.\frac{P_2 - P_1}{P_{1t} - P_1}\right|_{SuddenExp.} = 2\left(\frac{1}{AR} - \frac{1}{AR^2}\right) \tag{2.2}$$

Finally, when combining two diffusers and using the first inlet area as a reference, $AR = \frac{A}{A_0}$, it is obtained:

$$C_p(x) = \begin{cases} C_p^I(AR) & if \quad x \leq x_{interface} \\ \\ C_p^I(AR_{interface}) + \left(\frac{1}{AR_{interface}}\right)^2 C_p^{II}(AR/AR_{interface}) & if \quad x_{interface} < x \end{cases} \tag{2.3}$$

Where C_p^I and C_p^{II} are written in terms of their own area ratio, and the quantities labeled $interface$ are evaluated where both diffusers meet. Note that this only applies in the incompressible case, as it is using $P_t - P = \frac{1}{2}\rho u^2$.

Regarding the effect of non-uniform flows, Sovran & Klomp (1967, [10]) analysed an arbitrary velocity

---

[1] $$\overline{P_t} = \frac{1}{\dot{m}} \int \left(P + \frac{1}{2}\rho u^2\right) d\dot{m} = P + \frac{1}{2}\rho \overline{u}^2 \frac{1}{\dot{m}} \int \frac{u^2}{\overline{u}^2} d\dot{m} = P + \overline{q} \frac{1}{\rho \overline{u} A} \int \frac{u^2}{\overline{u}^2} \rho u dA = P + \overline{q} \frac{1}{A} \int \frac{u^3}{\overline{u}^3} dA = P + \alpha \overline{q}$$

profile in the incompressible regime with uniform static pressure. Under this conditions, the mass averaged total pressure is given by:

$$\overline{P_t} = P + \alpha\overline{q} \tag{2.4}$$

where $\overline{q}$ is the mass averaged dynamic pressure, $\overline{q} = \frac{1}{2}\rho\overline{u}^2$; $\overline{u} = \frac{\dot{m}}{\rho A}$; and α is the *kinetic-energy-flux velocity-profile*[1]:

$$\alpha = \frac{1}{A}\int\left(\frac{u}{\overline{u}}\right)^3 dA = \frac{\overline{u^2}}{\overline{u}^2} \tag{2.5}$$

The physical meaning of α is the ratio between the area average kinetic energy in the flow and the kinetic energy in an uniform flow with the same mass-flow. Note that $\alpha \geq 1$. Writing C_p for this non-uniform incompressible flow yields:

$$C_p = \frac{P_2 - P_1}{P_{1t} - P_1} = \frac{(P_{2t} - \alpha_2\overline{q_2}) - (P_{1t} - \alpha_1\overline{q_1})}{\alpha_1\overline{q_1}} = \frac{\alpha_1\overline{q_1} - \alpha_2\overline{q_2}}{\alpha_1\overline{q_1}} - \frac{P_{1t} - P_{2t}}{\alpha_1\overline{q_1}} = 1 - \frac{\alpha_2/\alpha_1}{AR^2} - k_{loss} \tag{2.6}$$

Combining with Equation 2.1:

$$C_p = C_{p,i} - \frac{\alpha_2/\alpha_1 - 1}{AR^2} - k_{loss} \tag{2.7}$$

This equation clearly shows that deviations in C_p from the ideal case are due to losses and non-uniformities [10]. K_{loss} is always positive, and thus it always reduces C_p. However, the non-uniformity term can take any sign. When the flow uniformity progressively increases due to mixing ($\alpha_2 < \alpha_1$), C_p can be greater than the ideal case.

Sovran & Klomp use Equation 2.7 to introduce the difference between *inefficient* diffusion (loss in C_p due to high k_{loss}) and *insufficient* diffusion (loss in C_p due to velocity profile). Years later, Mimic continued the development of this concept with the relation $C_p + k_{loss} + \xi = 1$. They study the sensitivity of a diffuser to augmentation methods and stall (Figure 2.1, [21]). Their work shows that the main effect of stall in diffuser is to reduce the effective area (A_{eff}), and thus reducing diffusion (ξ is greater). They find that this effect is more important than entropy generation, and thus steep diffusers show a greater sensitivity to stall position ($\frac{\partial C_p}{\partial x_{sep}}$).

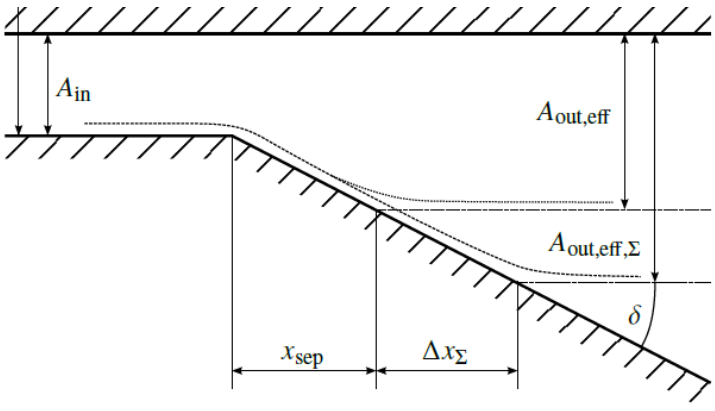

Figure 2.1: Effect of changing the stalling point in the effective area, A_{eff} of a diffuser. Recovered from Mimic et. Al, 2018 [21].

In the present work, both the *kinetic energy coefficient* and the *kinetic-energy-flux velocity-profile* concepts will be merged in two newly defined parameters. Noting the importance of ξ, it is separated in two terms: ξ_{bulk} and ξ_{NU} (non-uniform) such that:

$$\xi = \xi_{bulk} + \xi_{NU} \tag{2.8}$$

This allows the split of different effects in the discussion about tip gap influence on diffuser performance (Section 4.2). It is possible to rewrite Equation 1.4 as $1 = C_p + k_{loss} + \xi_{bulk} + \xi_{NU}$. This clearly shows that the non-dimensional energy in the diffuser is constant and can be split in *pressure potential energy*, C_p; *losses*, k_{loss}; *bulk kinetic energy*, ξ_{bulk}; and *kinetic energy in non-uniformities*, ξ_{NU}. Based on this energy representativeness, ξ_{bulk} is computed as follows:

1. Obtain bulk velocity defined as $u_{bulk} = \frac{\dot{m}}{\rho A}$, where ρ is an averaged value.
2. Obtain a total temperature based on *bulk kinetic energy*: $T'_t = T + \frac{u^2_{bulk}}{2C_p}$.
3. Obtain the associated total pressure: $P'_t = P\left(\frac{T'_t}{T}\right)^{\frac{\gamma}{\gamma-1}}$.
4. Use the regular ξ definition:

$$\xi_{bulk,j} = \frac{P'_{jt} - P_j}{P_{1t} - P_1}$$

A comparison with Equation 2.4 shows:

$$\alpha_j = \frac{\xi_j}{\xi_{bulk,j}}$$

Note that the definition of ξ_{bulk} and ξ_{NU} holds for compressible flows and non-uniform static pressure distributions, unlike α.

2.2. Basic turbomachinery concepts

This section is a sallow introduction to basic concepts and nomenclature to follow the discussion in a more streamlined way.

2.2.1. Coordinate system in a turbomachine

A turbomachine is a component that exchanges *mechanical work* with the working fluid. As such, it is important to track the different flow velocities and directions. It is the change in these magnitudes what informs the engineer about the momentum exchanges and, through Newton's second law, forces over the device.

The rotational nature of turbomachines makes quite natural the use of cylindrical coordinates. These are constituted by an axial direction, identified as x or z, a radial direction perpendicular to this one, identified as r, and the angle between the radial axis and a reference direction, θ. These coordinates (x, r, θ) generate a local vector basis $\mathcal{B} = \{\vec{u}_x, \vec{u}_r, \vec{u}_\theta\}$, where $\vec{u}_x$ is parallel to the longitudinal axis, $\vec{u}_r$ is parallel to the local radius, and $\vec{u}_\theta = \vec{u}_x \times \vec{u}_r$.

However, in the most general setting the flow is not always aligned with these coordinates. Traditionally, the flow has been described by using a coordinate system relative to the blades and with directions given by the local flow characteristics. One of the first ideas[29] was to define coordinate surfaces related to the local flow. These surfaces (Figure 2.2) were identified as $S1$, a stream-surface emanating from circumferential seed-lines; $S2$, a stream-surface emanating from span-wise seed-lines and $S3$, a surface perpendicular to the flow. Although this system has a strong theoretical basis, is inconvenient due to its dependencie on the flowfield. The most common reference system nowadays is a simplifications of this. The coordinate planes are not stream-surfaces, but geometrical constructions. The surface $S1$ is substituted by the *blade to blade* plane (B2B), a revolution surface whose generatrix is a constant span line[2]; the surface $S2$ is substituted by the *meridional plane*, a plane containing $\vec{u}_x$ and $\vec{u}_r$; and finally $S3$ is substituted by a surface locally perpendicular to the two previous, and called *secondary plane*.

[2]Note that this is almost a cylinder in axial machines and a bell in radial ones, Figure 2.2 b.

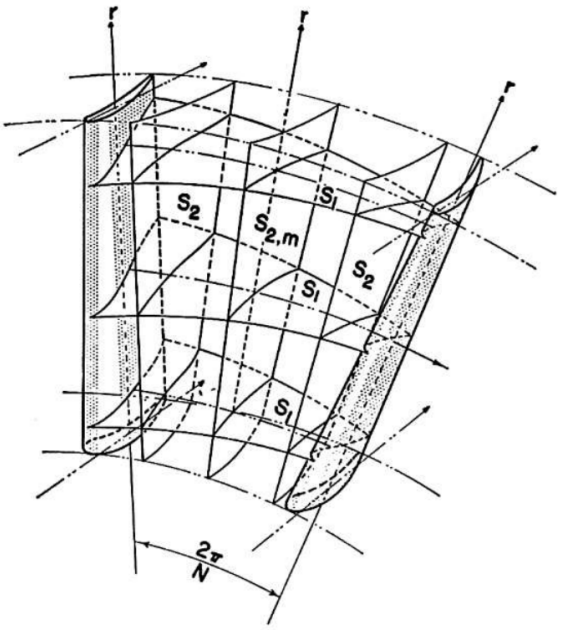

a) Schematic of $S1$ and $S2$ surfaces in an axial blade row (Chung-Hua Wu, 1952 [29]).

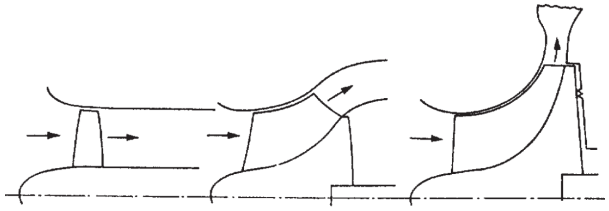

b) Different meridional gas paths in axial, mixed-flow and radial compressors (Dixon, 2013 [1]). The concept is analogous in turbines.

Figure 2.2: Description of the flowpath in turbomachines.

2.2.2. Secondary flows

Turbomachines generate complex flow-fields, notably unsteady and tridimensional. Usually the unsteady effects are disregarded by means of a temporal averaging procedure and studying the flow in a relative frame. However, the enclosed nature of the flow and the high deflections it is subjected to makes it unavoidable to work with 3D flows. More accurately, turbomachine flows are a subset of the field of *internal flows*. In this kind of flows, the fluid is surrounded by walls and their influence is very relevant. One of the most typical flow phenomena is known as *secondary flows*.

Secondary flows are defined as *"cross-flow plane (secondary) circulations which occur in flows that were parallel at some upstream station"*[28]. Relating this to the coordinate system introduced before, these secondary flows would introduce velocities with a projection on the $S3$ surface. The term secondary does not imply that these effects are small[3], but it only makes reference to the fact that these flow structures are not aligned with what is supposed to be the main flow. Secondary flows are always related to non-uniformities (mostly, but not exclusively, due to boundary layers), and they are explained through 2 complementary views.

The first of them is related to *vorticity*. This is a quantity defined as $\vec{\omega} = \nabla \times \vec{v}$ and it is related to the rotation of a fluid particle (great discussions can be found in references such as [28]). If the Navier-Stokes (NS) equations are re-written in terms of this quantity, it is possible to prove that *vortex-lines*[4] cannot begin or end in the flowfield and they are convected by the main flow. This explains, for instance, the existance of *horse-shoe vortexes* (HSV), Figure 2.3: The vortex lines from the incoming boundary layer get stuck in the leading edge of the blade and they role up into coherent vortexes.

The second line of though is related to force balances. This argumentation is purely based on Newton's second law. Let some flow turn in a blade cascade. This turning implies a change in linear momentum direction, and thus a force perpendicular to the streamline. This is provided by a pressure gradient such that the main flow is in equilibrium trough the turn. Now, let a lower-momentum particle, like one in a boundary layer, enter that same passage. It is going to be subjected to the same pressure gradient. As this particle has less *inertia*, the same force will deflect it more, and thus the flow in the endwalls tends to

[3] As "second order effect" might suggest.

[4] A concept analogous to streamlines, it is a line tangential to the vorticity vector field.

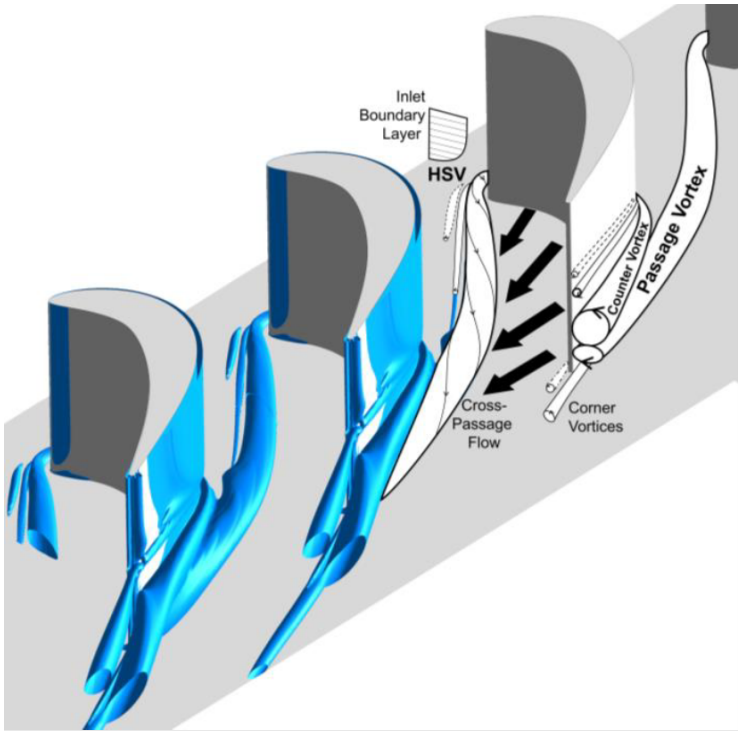

Figure 2.3: Axial turbine typical flow structures (Coull, 2016 [30]).

be convected to the suction sides of the blades [31]. The opposite will happen with a particle with greater momentum than the average, for instance scraping flow: the higher inertia of this structure will imply that the pressure gradient is not strong enough to turn it[5].

2.2.3. RIT tip gap flows

Between the rotating blades (rotor) and the casing, there must be some clearance to avoid rubbing the blades against the stationary parts. This clearance is known as the *tip gap*, and it generates complex flow patterns related to mixing losses and a strong coherent vortex known as the *tip gap vortex*[6].

This gap over the blade effectively connects the pressure and the suction side generating a jet. This jet has a high tangential velocity component that mixes out with the rest of the fluid without generating power. There are several models to predict the performance loss due to this mixing process. However, this jet also creates a shear layer that roles up into a vortex. There is not a lot of literature about this phenomena and it is not trivial to predict the strength of such a vortex. Furthermore, the radial machine has a thinner and longer-chord blade, what makes the flow structure quite different from the axial counterpart [32][33].

In addition, the relative movement of the blades and the casing generates a *scraping flow*. This is a tangential boundary layer in the relative reference system, which rolls into a *scraping vortex* partially sealing the leakage. In some situations, the scraping can be so strong that flow is dragged from suction side to pressure side, totally cancelling the classical tip gap leakage[33].

These two vortexes, the tip gap vortex and the scraping vortex, interact strongly between them and with the meridional curvature of the channel in a radial machine. This behaviour is crucial to the understanding of turbine diffuser interaction.

The prominent publications in this fields are those by Dambach & Hodson (University of Cambridge) in 1998 and 2001 ([32][33]). They perform an experimental study in a large radial machine with different tip gap configurations and make detailed measurements inside the gap, Figure 2.4. They are the first

[5]Note that this view also explains the HSV: the static pressure is uniform in a boundary layer, but there is a gradient of stagnation pressure (lower at the wall). When the boundary layer hits the leading edge of the blade, it slows down and recovers the stagnation pressure, generating a static pressure gradient. Then, the flow is convected towards the lower static pressure at endwall in the LE vicinity. This movement rolls up a vortex: the HSV.

researchers to report flow from the suction side migrating to the pressure side due to scraping. Based on their results, they define 3 regions in the radial rotor:

1. **Inducer:** In this region the casing relative velocity is high, and the loading of the blade is low. The pressure difference is not high enough as to overcome scraping and flow can go from suction to pressure side dragged by the casing.
2. **Mid section:** In this region the loading of the blade is maximum and the scraping is becoming weaker. It is in this section were the highest tip leakage mass flow rate is found. There is an strong interaction of both scraping and pressure-driven leakage.
3. **Exducer:** In the last portion of the rotor both loading and scraping reduce, and the tip gap flow is dominated only by pressure forces.

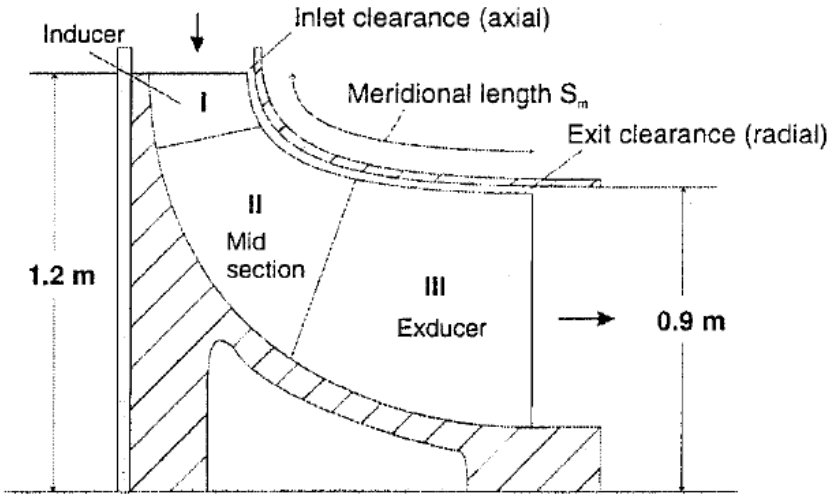

Figure 2.4: Radial turbine different regions regarding tip gap flow characteristics. From Dambach et al., 2001[33].

They report that the turbine performance is more sensitive to changes in radial (trailing edge) gap because the scraping flow is sealing the axial gap at the leading edge of the blade. They also detect the necessity of including scraping effects in any modeling attempt for tip gap leakage in radial machines.

Two parameters are provided to characterize the flow over the tip. The first of them is the ratio of the pressure effects and the scraping effects:

$$R = \frac{\Delta P_{over-tip}}{\frac{1}{2}\rho U^2 \cos^2 \gamma} \tag{2.9}$$

Where ρ is the local density, U is the local casing relative velocity ($U = \Omega \cdot r$), and γ is the local blade angle with respect to the radial direction (Figure 2.5 a, $U_n = U \cos\gamma$). When this ratio is greater than one, the pressure driven flow will dominate. When this parameter is less than one, scraping effects and pressure driven effects will compete.

The second parameter is:

$$\lambda = \frac{\epsilon}{t} \tag{2.10}$$

where ϵ is the gap size and t is the blade thickness at the tip. This is the aspect ratio of the gap. In their paper[33], Dambach & Hodson discuss the existence of a λ_{crit} such that $\lambda < \lambda_{crit}$ presents a different flow regime than $\lambda > \lambda_{crit}$ (Figure 2.5 b). In slender tip gap passages the leakage flow mixes out in the interior of the gap cavity. However, for relatively higher (or *shorter*) gaps, there is a region of flow that emanates from the gap as an *isentropic jet*. This jet is more energetic and it is likely to affect the casting of the tip gap vortex. The value of λ_{crit} is unknown and potentially is is a function of Re. Nonetheless they report $\lambda \approx \frac{1}{5}$ or $\frac{1}{6}$ in their case.

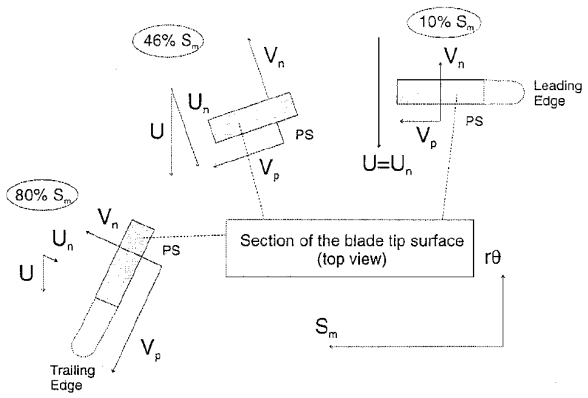

a) Schematic of the scraping velocity at different streamwise stations of a radial turbine.

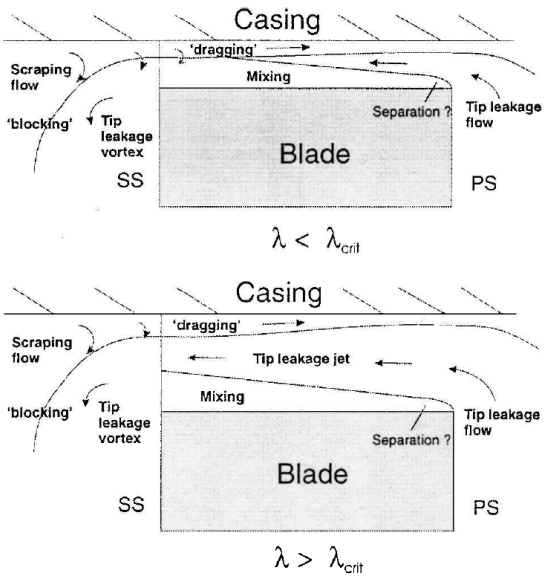

b) Different tip gap flow patterns.

Figure 2.5: Figures supporting the tip gap parameters. Recovered from Dambach et al 2001 [33].

The authors treat the problem as local, and they disregard the effect of scraping and tip gap vortexes casted further upstream of the location. The present study adress this effect in Section 4.3. One major piece missing in the tip gap flow study is understanding and modelling the vortex casting process. This reference is a major milestone, but there is more work to do.

One important general result is that the existence of the tip gap does not modify the static pressure distribution in the tip region, so this data can be used as an input to an explicit tip gap leakage model.

2.2.4. RIT flow structures

The study of flow structures has been gaining interest due to the introduction of 3D computational methods in the study of turbomachines. In order to better understand the 3D *vortical structures* and *secondary flows*, researchers have recognised, named, and characterized some recurrent structures. This field is greatly developed in axial machines (Figure 2.3) and it is the theoretical basis for several 3D design methods. However, this knowledge has not been transferred to the radial counterparts.

The first reference, to the knowledge of the author, about secondary flows in RITs is that of Zangeneh et al. (1988, [31]). They run coarse[6] CFD computations in a radial turbine and study the secondary flows as boundary layer cross-flow due to loading and inertia forces. This is argued applying vorticity, $\vec{\omega}$, transport equations. They explain the high loss ”wake” usually found in the suction side shroud corner[7] as a combination of accumulation of this low momentum cross-flow and tip gap leakage flow. A conclusion of the paper is the importance of modelling the tip gap flows to predict losses in radial machines. They do not report about vortical structures.

[6]Coarse by today's standards: 16 thousand nodes, $y^+ \sim O(30)$.

[7]A description of this high entropy region is provided in the results of this text, Figure 4.27

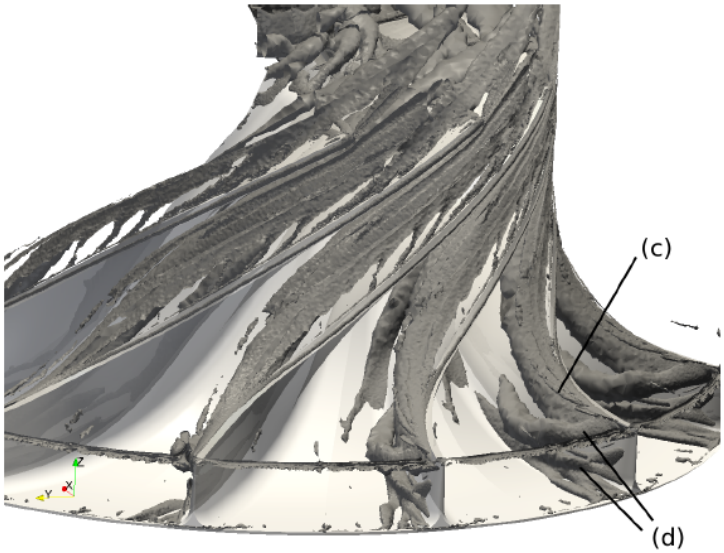

Figure 2.6: Radial turbine flow structures (Marsan & Mareau, 2015 [34]). Isocontours of the Q-criterion are shown as a method to locate the vortex cores.

Apart from this, one of the few studies in RIT flow structures is that by Marsan & Mareau (2015, [34]). These researchers analyse the different flow structures comparing steady and unsteady simulations. They report that the differences between steady state (RANS) and time average quantities of unsteady simulations (URANS) are confined to a small region at the inlet of the rotor. Figure 2.6 shows their result for the steady case. In this image, the label c identifies the *tip leakage vortex* and the label d are vortical structures similar to HSV, but also related to boundary layer separation. These vortical structures are generated at the leading edge and they migrate to the pressure surface. The dependency with design parameters or operation conditions is not analysed in this work.

The present text will deepen in these vortex dynamics and it will relate the structures to diffuser performance (Section 4.3)

2.3. Thermodynamics Applied to Turbomachinery

Along this section the basic thermodynamics principles will be laid down in such a way that the effect of the diffuser is clearly apparent.

2.3.1. Basic thermodynamic relationships

Energy equation

A turbine is a device that extracts power from a stream of fluid. A simple analysis can be done with the first law of thermodynamics for an open control volume Ω:

$$\frac{dE_\Omega}{dt} = \dot{m}_{in}\cdot(h_{in} + \frac{1}{2}v_{in}^2) - \dot{m}_{out}\cdot(h_{out} + \frac{1}{2}v_{out}^2) + \dot{Q}_{in} + \dot{W}_{in} \tag{2.11}$$

Where E_Ω is the total energy of the system, $\dot{m}_{in}$ is the incoming mass flow into the control volume, h_{in} is the specific enthalpy of the flow entering the volume, $\frac{1}{2}v_{in}^2$ is the incoming kinetic energy to the volume, $\dot{Q}_{in}$ and $\dot{W}_{in}$ are the heat and work absorbed by the system per unit time, and all the quantities labeled "out" are leaving the volume. It is customary [1] to assume that the turbine is adiabatic ($\dot{Q} = 0$) and that it is operating is steady state ($\dot{E}_\Omega = 0$, $\dot{m}_{in} = \dot{m}_{out}$). In this situation it is useful to use the *specific work*, $w = \dot{W}/\dot{m}$, and to write the energy that the turbine is extracting from the flow as:

$$w_{out} = \left(h_{in} + \frac{1}{2}v_{in}^2\right) - \left(h_{out} + \frac{1}{2}v_{out}^2\right) = -\Delta h_t \tag{2.12}$$

Where the quantity *specific total enthalpy*, h_t, has been introduced as the combination of enthalpy and kinetic energy. Note that in a turbine the total enthalpy of the flow decreases, and thus the specific work of

the turbine is defined as positive. This is an arbitrary choice.

Total quantities
Total quantities are the magnitudes (pressure, temperature, and density) that the system would achieve if it is decelerated by and *isentropic* process without any energy exchange. For an ideal gas, enthalpy is a function only of temperature ($h = C_p \cdot T$, with C_p the specific heat capacity of the material). Applying this to the previous requirements of total state makes the definition of total temperature, T_t, trivial:

$$h_t = C_p T_t = C_p T + \frac{1}{2} v^2 = h \rightarrow T_t = T + \frac{1}{2C_p} v^2 \tag{2.13}$$

The restriction of isentropic implies (in an ideal gas):

$$\Delta s_{1\rightarrow 2} = 0 \rightarrow \left(\frac{P_2}{P_1}\right)^{\frac{\gamma-1}{\gamma}} = \frac{T_2}{T_1} \tag{2.14}$$

Where γ is the specific heat ratio, $\gamma = C_p/C_v$. Then, all the total properties of an ideal gas are defined as:

$$\left(\frac{\rho_t}{\rho}\right)^{\gamma-1} = \left(\frac{P_t}{P}\right)^{\frac{\gamma-1}{\gamma}} = \frac{T_t}{T} = 1 + \frac{\gamma-1}{2} M^2 \tag{2.15}$$

With M as the Mach number, $M = v/a$, where $a = \sqrt{\gamma R_g T}$ is the velocity of sound and R_g is the gas constant in $[J/(K \cdot kg)]$. Equation 2.15 is known as the isentropic relationships. Note that in an ideal gas the ratio of total and static magnitudes only depends on the local Mach number.

Rothalpy
The most basic tool to design a turbomachine, or to discuss the origin of its *mechanical power*, is the Euler equation [1]. This equation links thermodynamics with angular momentum exchange:

$$\Delta h_t = w = \Omega \cdot (R_2 v_{2t} - R_1 v_{1t}) \tag{2.16}$$

where $w = \frac{\dot{P}}{\dot{m}}$ is the specific power exchanged with a streamtube, sub-indices 1 and 2 are, respectively, inlet and outlet of the stage, Ω is the rotational speed, R is the radius, and v_t is the tangential velocity in the absolute frame. This expression clearly shows that the power output of a turbine is related both to flow deflection and a change in radius. This second component is very relevant in radial machines, as it will allow greater power extractions without high aerodynamic loading.

Introducing $U_j = \Omega \cdot R_j$ and $w_{jt} + U_j = v_{jt}$[8], where w is the velocity in the relative frame, it is possible to rewrite Equation 2.16 as:

$$h_{2t} + \frac{w_2^2}{2} + \frac{U_2^2}{2} - \frac{v_2^2}{2} = h_{1t} + \frac{w_1^2}{2} + \frac{U_1^2}{2} - \frac{v_1^2}{2}$$

$$I_2 = h_{2t,\ rel} + \frac{U_2^2}{2} = h_{1t,\ rel} + \frac{U_1^2}{2} = I_1 \tag{2.17}$$

Where $h_{t,\ rel}$ is the specific total enthalpy in the rotating frame. Under the assumptions deriving Euler's equation[9], $I = h + \frac{w^2}{2} + \frac{U^2}{2}$ is a conserved quantity called *rothalpy* [29].

Entropy production and $h - s$ diagram
Entropy is a thermodynamic property defined as:

$$ds = \frac{\partial Q_{rev}}{T} \tag{2.18}$$

[8]This follows from basic geometry relationships, refer to a turbomachinery specific book such as [1].

[9]Notably, Equation 2.16 is disregarding any viscid effects. The viscid forces from the casing can do work in the relative frame, and thus they can change rothalpy (Lyman, 1993[35]).

where Q_{rev} is the heat exchanged during a reversible process. For an ideal gas, this equation can be integrated into:

$$\Delta s_{1\to 2} = C_p \ln\left(\frac{T_2}{T_1}\right) - R_g \ln\left(\frac{P_2}{P_1}\right) \tag{2.19}$$

Entropy is tightly linked to concepts such as *reversibility* and *efficiency*. Turbine efficiency is defined as the ratio of the actual energy extraction of the machine and the theoretical energy extraction with the same pressure drop and $\Delta s = 0$. It is possible to show that the isentropic expansion extracts the most energy possible. It is usual to plot thermodynamic processes in $h - s$ diagrams (Figure 2.7). These plots show the entropy in the horizontal axis and the energy (in an ideal gas, temperature) in the vertical axis. It is also customary to add constant pressure lines, that regarding Equation 2.19 are diverging exponentials:

$$T(s)|_{P_0} = T_{ref} \exp\left\{\frac{s - s_{ref}}{C_p}\right\} \tag{2.20}$$

Where P_0 is the constant pressure, T_{ref} is a given reference temperature and s_{ref} is the entropy of the reference state, $s_{ref} = s(T_{ref}, P_0)$. The black lines are isobaric lines labeled in bar. This graph clearly shows that, for a given pressure ratio, the power extraction (proportional by the difference in temperatures) is reduced when entropy is generated in the process.

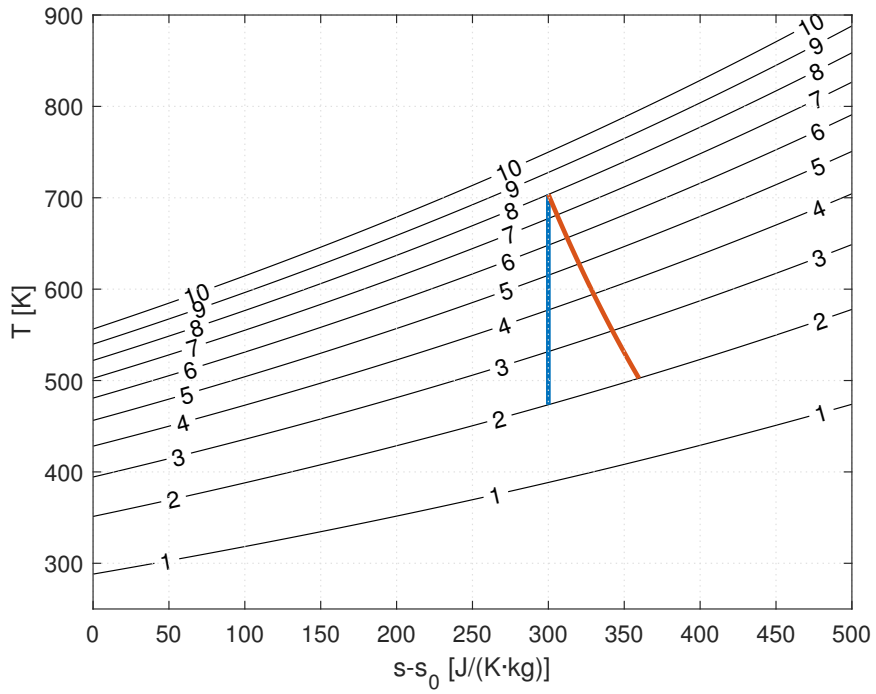

Figure 2.7: Example of an $T - s$ diagram for an ideal fluid with $C_p = 1004.5\ J/(K{\cdot}kg)$ (Representative of air). Isobaric lines labeled in bar. The blue evolution is an isentropic expansion while the orange one is an evolution of polytropic efficiency $e_p = 0.85$.

2.3.2. Turbine efficiency metrics

The most common efficiency metric on a turbine is the *total to total efficiency*, η_{tt}. This is the ratio between the work extracted by the turbine and the work that would have been extracted with the same total pressure drop in an isentropic process:

$$\eta_{tt} = \frac{w_{real}}{w_{is}} = \frac{T_{1t} - T_{2t}}{T_{1t} - T_{2t,is}} = \frac{1 - \frac{T_{2t}}{T_{1t}}}{1 - \left(\frac{P_{2t}}{P_{1t}}\right)^{\frac{\gamma-1}{\gamma}}} \tag{2.21}$$

This formula is evaluating the efficiency of a *macroscopic* process. It is also useful to define the performance of an infinitely small (differential) expansion. This will result in a *polytropic efficiency*[10], e_p:

$$e_p = \frac{\partial w_{real}}{\partial w_{is}} = \frac{\frac{dT}{T}}{\frac{\gamma-1}{\gamma}\frac{dP}{P}} \rightarrow \frac{T_2}{T_1} = \left(\frac{P_2}{P_1}\right)^{e_p \frac{\gamma-1}{\gamma}} \tag{2.22}$$

Substituting Equation 2.22 into Equation 2.21 it is possible to obtain the relation between them as a function of pressure ratio:

$$\eta_{tt} = \frac{1 - \left(\frac{P_{2t}}{P_{1t}}\right)^{e_p \frac{\gamma-1}{\gamma}}}{1 - \left(\frac{P_{2t}}{P_{1t}}\right)^{\frac{\gamma-1}{\gamma}}} \tag{2.23}$$

These efficiency metrics are making one implicit assumption: the kinetic energy at the outlet of the turbine is used. However, if this exhaust energy *is wasted*, it is not equivalent to compare machines in terms of η_{tt}. This difference is also relevant when the boundary condition downstream of the machine is a static pressure, like a subsonic jet open to the atmosphere. In these cases the most meaningful parameter is the *total to static pressure ratio*, β_{ts}. For these reasons, another metric of efficiency is introduced: the *total to static efficiency*, η_{ts}:

$$\eta_{ts} = \frac{w_{real}}{w_{is} + e_k} = \frac{T_{1t} - T_{2t}}{T_{1t} - T_{2t,is} + \frac{v_{out}^2}{2C_p}} \approx \frac{T_{1t} - T_{2t}}{T_{1t} - T_{2,is}} = \frac{1 - \frac{T_{2t}}{T_{1t}}}{1 - \left(\frac{P_2}{P_{1t}}\right)^{\frac{\gamma-1}{\gamma}}} \tag{2.24}$$

Where e_k is the *specific kinetic energy* at the outlet, $e_k = \frac{1}{2}u_{out}^2$. Note that this is the ratio between the real work and the work extracted in an isentropic expansion when the outlet velocity is zero. This expression depends on the total to static pressure ratio, and for a given machine it is always true that $\eta_{ts} < \eta_{tt}$.

2.3.3. Impact of the diffuser on the thermodynamic processes

Diffusers are employed when the physical boundary condition of the turbine is given as a fixed *static* pressure at the outlet[11]. Through the diffuser the static pressure increases, and thus this device allows the extraction of more energy by lowering the pressure at the outlet of the turbine. This is clearly illustrated in Figure 2.8.

In this example, the turbine without a diffuser reaches the static pressure of 1 bar at the outlet, and thus its total pressure at the outlet is $1.19\ bar$. The kinetic energy at the outlet of the turbine ($M = 0.5$) is $18.8\ J/(kg{\cdot}s^{-1})$, and the efficiencies are $\eta_{tt} = 0.907$ and $\eta_{ts} = 0.700$. When a diffuser is added (Assuming $C_p = 0.5$ and $k_{loss} = 0.15$), the static pressure at the outlet of the turbine drops to $P = 0.915$, achieving a lower total pressure at the outlet of $P_t = 1.09\ bar$. Now, the kinetic energy at the outlet of the turbine is $18.4\ J/(kg{\cdot}s^{-1})$, and at the outlet of the diffuser it is $6.3\ J/(kg{\cdot}s^{-1})$. The efficiencies of the assembly with the diffuser are $\eta_{tt} = 0.877$ and $\eta_{ts} = 0.835$.

The results of this very simple exercise are summarised in Table 2.1. They show that for a fixed static pressure at the outlet, the usage of a diffuser can yield an increase of 17% on power output for the same inflow conditions. Note that this is achieved due to a higher η_{ts} even when η_{tt} is reduced by the diffuser. It has been assumed that $e_p = 0.9$ in both cases. The higher expansion ratio will increase η_{tt} of the turbine (Equation 2.23).This implies that the loss in total to total efficiency is due to the entropy generation in the diffuser.

[10] In the expression:

$$\partial w_{real} = C_p T \frac{dT}{T}$$

$$\partial w_{is} = C_p T \frac{dT|_{\Delta s=0}}{T} = R_g T \frac{dP}{P} = C_p T \frac{\gamma - 1}{\gamma}\frac{dP}{P}$$

[11] Note that another boundary condition might be a choked section downstream of the device.

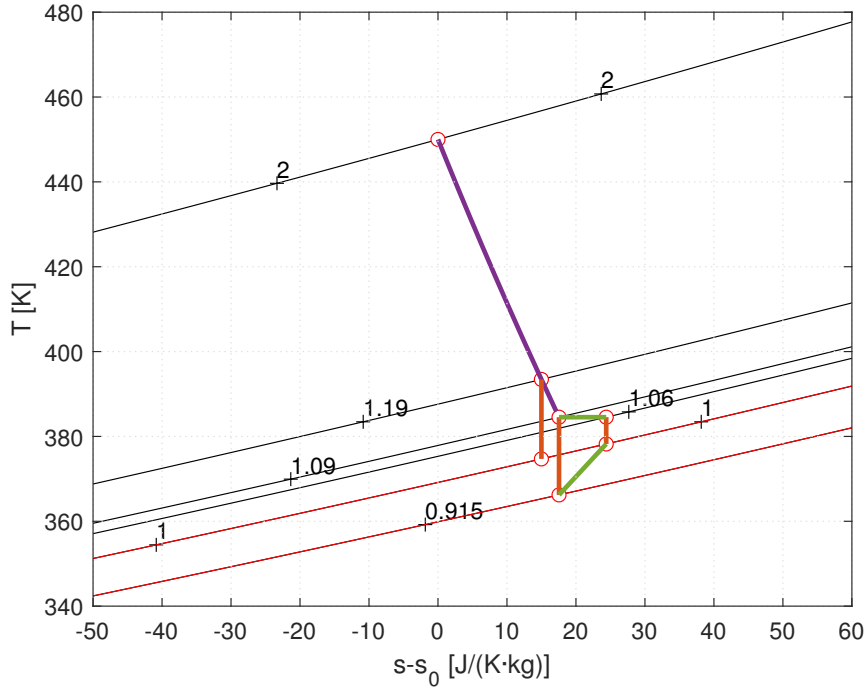

Figure 2.8: $T - s$ diagram for a turbine expansion between an upstream total pressure $P_{0t} = 2\ bar$ and a fixed outlet static pressure $P_2 = 1\ bar$. $e_p = 0.9$, pressure labels in bar, $M_{out} = 0.5$. Black isobars are total pressure, whereas red isobars are static pressure. Orange lines represent kinetic energy. The purple line is the expansion in the turbine, and the green lines are the evolution through the diffuser. The diffuser is modeled as $C_p = 0.5$ and $k_{loss} = 0.15$

2.4. 0D Turbine-Diffuser Interaction Model

This study[12] intends to show the influence on $\tilde{w} = \frac{w}{\widehat{C_p} T_{4t}}$ of the diffuser. The assumptions along this section are:

- Ideal gas,
- flow properties in a given section can be characterized by a single (averaged) value,
- constant polytropic efficiency e_p, regardless the expansion ratio, and
- the total to static expansion ratio, β_{ts}^{Sys}, of the *system* is a fixed boundary condition.
- Chocked stator

The nomenclature followed is such that station 4 is the inlet to the stator, station 41 is the throat of the stator, station 5 is the outlet of the rotor, and station 6 is the outlet of the diffuser. This implies $\beta_{ts}^{Sys} = \frac{P_{4t}}{P_6} = const.$.

Combining Equation 2.12 and Equation 2.22 it is obtained:

$$\tilde{w} = \frac{w}{\widehat{C_p} T_{4t}} = 1 - (\beta_{tt}^T)^{-\frac{\gamma-1}{\gamma} e_p} \tag{2.25}$$

In this expression $\widehat{C_p}$ is the heat capacity at constant pressure, and $\beta_{tt}^T = \frac{P_{4t}}{P_{5t}}$ is the total to total expansion ratio of the *turbine*. $\beta_{tt}^{Sys} = \frac{P_{4t}}{P_{6t}}$ is the total to total expansion ratio of the assembly including the diffuser. It is easy to see that $\beta_{ts}^{Sys} \geq \beta_{tt}^{sys} \geq \beta_{tt}^T$.

The expansion ratio of the assembly can be written as:

$$\beta_{ts}^{Sys} = \frac{P_{4t}}{P_6} = \frac{P_{4t}}{P_{5t}} \frac{P_{5t}}{P_5} \frac{P_5}{P_6} = const. \tag{2.26}$$

[12] This proposal is new to the knowledge of the author. Strongly based on the work by Farokhi[2], this version expands on the three parameters defining the diffuser (C_p, k_{loss} and ξ) to provide a solid framework about the trade-off happening in the diffuser.

Table 2.1: Numerical results of the example proposed in Figure 2.8 ($e_p = 0.9$, $C_p = 0.5$, $k_{loss} = 0.15$).

	Without Diffuser	**With Diffuser**	**Comparison**
$M_{turbine}$	0.5	0.5	-
β_{ts}	2	2	-
$\beta_{tt,turbibe}$	1.68	1.83	$\Delta = +0.15$ (+9%)
$\beta_{tt,System}$	1.68	1.89	$\Delta = +0.21$ (+12.5%)
w $[kJ/(kg{\cdot}s^{-1})]$	56.2	65.8	$\Delta = +9.6$ (+17%)
$e_{k,outlet}$ $[J/(kg{\cdot}s^{-1})]$	18.8	6.3	$\Delta = -12.5$ (−66%)
η_{ts}	0.700	0.877	$\Delta = +0.177$
η_{tt}	0.907	0.835	$\Delta = -0.072$

Recognizing in this expression $\frac{P_{4t}}{P_{5t}} = \beta_{tt}^T$, $\frac{P_{5t}}{P_5} = g(M_5)$ (Equation 2.15), and applying the definition of C_p (Equation 1.1), β_{tt}^T can be obtained as:

$$\beta_{tt}^T = \frac{\beta_{ts}^{Sys}}{g(M_5)}\left[1 + C_p\left(g(M_5) - 1\right)\right] \rightarrow \frac{\beta_{tt}^T}{\beta_{ts}^{Sys}} = \frac{1}{g(M_5)} + C_p\left(1 - \frac{1}{g(M_5)}\right) \tag{2.27}$$

This shows that for a given M_5, β_{tt}^T will increase linearly with C_p, and it is independent of the other diffuser parameters. A plot of this behaviour is shown in Figure 2.9 a. Note that $g(M_5)$ is a monotonic function, so the higher the turbine outlet mach number is, the more sensitive the machine is to a diffuser. However, for a given C_p and β_{ts}^{Sys}, β_{tt}^T will be smaller for higher M_5. The sensitivity of the turbine to C_p is weighted by M_5 because this is a measure of outlet *kinetic energy*[13]. On the other hand, higher M_5 implies more dynamic pressure at the outlet of the rotor, what explains why β_{tt}^T is reduced for a given C_p.

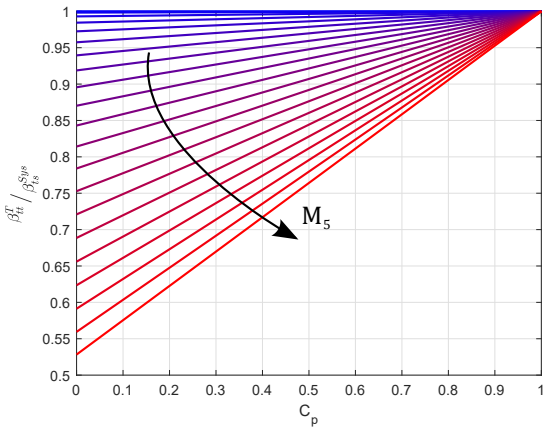

a) Relation between β_{tt}^T and β_{ts}^{Sys} (Equation 2.27)

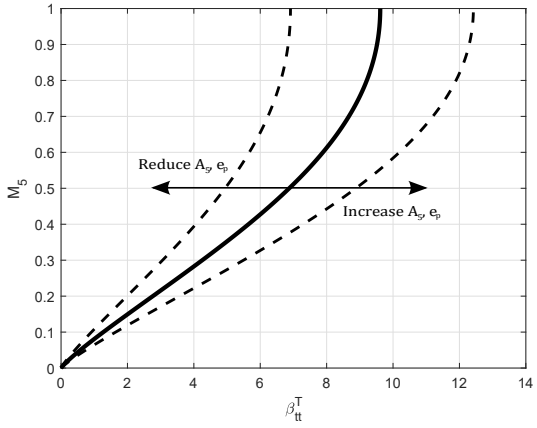

b) Relation between β_{tt}^T and M_5 in the present model (Equation 2.29).

Figure 2.9: Graphic representation of the basic relationships shaping the interaction model. Reference values based on typical RIT: ${}^{A_5}/_{A_{41}} \approx 7.2$, $e_p = 0.9$.

Note that changes in C_p for a given turbine and boundary conditions will also change M_5.This can be evaluated imposing conservation of mass and assuming that $\dot{m}$ does not change with C_p. Using the non-dimensional mass-flow:

$$\tilde{\dot{m}}_5 = \dot{m}\frac{\sqrt{R_g T_{5t}}}{P_{5t} A_5} = f(M_5) = \sqrt{\gamma} M_5 \left(1 + \frac{\gamma - 1}{2} M_5^2\right)^{-\frac{\gamma+1}{2(\gamma-1)}} \tag{2.28}$$

[13]Note that $M^2 = \frac{v^2}{\gamma R_g T} = \frac{2\widehat{C_p}}{\gamma R_g}\frac{\frac{1}{2}v^2}{\widehat{C_p}\cdot T} = \frac{2}{\gamma - 1}\frac{e_k}{h}$

Relating it to upstream conditions, and using Equation 2.22:

$$\tilde{\dot{m}}_{41} = \dot{m}\frac{\sqrt{R_g T_{41t}}}{P_{41t}A_{41}} = f(M_{41}) = \tilde{\dot{m}}_5 \frac{A_5}{A_{41}}\frac{P_{5t}}{P_{41t}}\sqrt{\frac{T_{4t}}{T_{5t}}} = \frac{A_5}{A_{41}}(\beta_{tt}^T)^{\frac{\gamma-1}{2\gamma}e_p - 1} f(M_5) \tag{2.29}$$

Assuming that the stator is chocked[14] ($M_{41} = 1$), this expression will always equate a constant, $\tilde{\dot{m}}_{41} = \sqrt{\gamma}\left(\frac{\gamma+1}{2}\right)^{-\frac{\gamma+1}{2(\gamma-1)}}$. Then, this is an implicit expression for the dependence of M_5 and β_{tt}, and it is shown in Figure 2.9 b. This relation shows how a diffuser changes turbine outlet mach number: if β_{tt}^T increases, M_5 also increases. Note that this expression of mass-flow is only valid for uniform flows without swirl. Even if a turbine is designed like this, changes in M_5 will modify swirl angle, so this should be taken only as a trend and not as a proper computed value.

It is possible to evaluate the expected delta in performance due to the addition of a diffuser. Defining the helper function $h(C_p, M_5)$:

$$h(C_p, M_5) = \left[\frac{1}{g(M_5)} + C_p\left(1 - \frac{1}{g(M_5)}\right)\right]^{-\frac{\gamma-1}{\gamma}} \tag{2.30}$$

the non-dimensional specific work, $\tilde{w}$ is:

$$\tilde{w} = 1 - h(C_p, M_5)(\beta_{ts}^{Sys})^{-\frac{\gamma-1}{\gamma}} \tag{2.31}$$

And the effect of the diffuser can be evaluated as:

$$\frac{\Delta\tilde{w}}{1-\tilde{w}_0} = 1 - \frac{h(C_p, M_5)}{h(C_p = 0, M_{5,0})} \tag{2.32}$$

where $M_{5,0}$ is the turbine outlet mach number without diffuser ($P_5 = P_6$). Note that M_5 is a function of $M_{5,0}$ and C_p.

Figure 2.10 shows the results of this model. The colored contours in the plot are the expected improvement after the addition of the diffuser expressed as $\frac{\Delta\tilde{w}}{\tilde{w}_0}\frac{\tilde{w}_0}{1-\tilde{w}_0}$. The horizontal axis represents diffuser pressure recovery, and the vertical axis is the outlet Mach number for the turbine operating without diffuser, $M_{5,0}$. The black lines are contours of M_5 number ***after*** the addition of the diffuser. Note that C_p always increases M_5, and it could even choke the rotor[15]. The message of this plot is that higher C_p will always increase power output, and this enhancement is more noticeable if the turbine outlet has high mach number. This is because, if the Mach number is low, the diffuser does not have kinetic energy to recover. Finally, note that the percentage gain of power, $\frac{\Delta w}{w_0}$, is the value read from the contours scaled by $\frac{1}{\tilde{w}_0} - 1$. For high power machines ($\tilde{w}_0 \approx 1$), the effect of the diffuser is very small. The opposite is true for small machines: a modest $\tilde{w}_0 \approx 0.23$ ($\beta_{tt}^R \approx 2.5$) can easily increase its power output by 10%.

The results are:

- The addition (or modification) of a diffuser changes turbine working conditions, specifically outlet Mach number and swirl angle.
- For a given turbine and mass flow, higher C_p will increase rotor outlet Mach number approaching sonic conditions.
- The effect of a diffuser is less noticeable for high pressure ratio machines. However, it can provide a considerable fraction of the total power in a low pressure ratio device.
- The diffuser requires high kinetic energy at the inlet (Mach number) to make a substantial addition to the performance of the machine.
- For a given machine operating with a diffuser, an increase in M_5 will reduce $\beta_{tt}^T / \beta_{ts}^{Sys}$.
- The performance enhancement is only related to C_p. The rest of diffuser performance metrics only modify how challenging it is to achieve the desired C_p.
- It is necessary to consider the characteristics of the diffuser when designing the turbine[16]. It is a coupled problem.

[14] This assumption is questionable for very low pressure ratio turbines, but it is confirmed in most cases with practical application.

[15] The consistency of the model for such high mach numbers is questionable.

[16] And this text will show that it is necessary to consider the turbine when analyzing the diffuser.

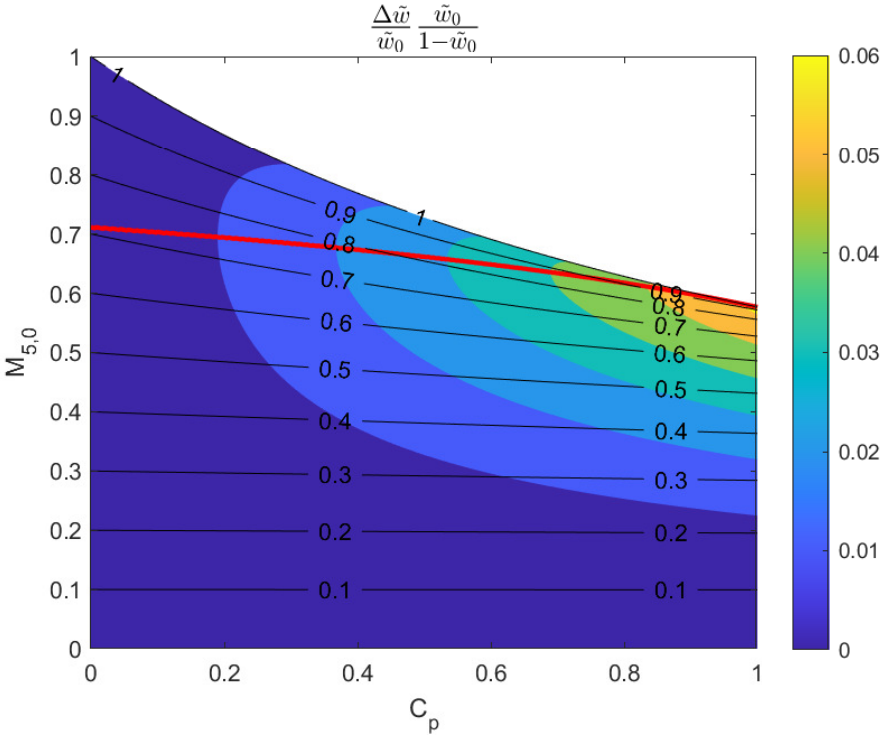

Figure 2.10: Map of diffuser effect on work extraction when compared to an isolated turbine. The vertical axis is the outlet Mach number *before* the addition of the diffuser, the colored contours are proportional to the improvement after the addition of the diffuser and the black lines are contours of mach number after the addition of the diffuser. The red bold line is the locus of maximum enhancement for a given C_p.

2.4.1. Research Question 1

Research Question 1

What is the potential impact of a diffuser in turbine work extraction, and under which conditions is this device more relevant?

Figure 2.10 shows that the percentage gain in energy extraction can be as high as 10% under the proper conditions. Furthermore, this enhancement is greater for small pressure ratios and high outlet Mach numbers. The work enhancement by the diffuser is independent of the total stage pressure drop, and thus it is relatively bigger for low pressure ratio machines. Furthermore, the diffuser will be more noticeable if rotor outlet Mach number, M_5, is high. Lastly, it has been proven that the only diffuser parameter affecting turbine work extraction (for a given β_{ts}^{Sys}) is the *pressure recovery coefficient*, C_p.

3

Methodology

3.1. Organization of the Project

The objective of the project is to characterize the interaction of a radial turbine and a diffuser, and possibly condense this into a low order interaction model[1]. However, between the starting point and this objective there were several unknowns that should be adressed.

The first step was to carry out a literature review on diffuser computational techniques, summarised here in Section 3.2. Then, several possibilities involving low order design tools where explored, but they did not provide the results expected. It was at this point when it was decided to limit the scope of the project to on-design conditions and only analysing the effect of tip gap size for a given geometry with CFD. The selection of tip gap distribution as the primary parameter is based on literature research, and studying one geometry at on-design conditions is a limitation derived from time constraints.

The research will be done by means of CFD methods. The selected solver is *Ansys CFX* due to its maturity, user expertise, and robust turbomachinery meshing tool (*Turbogrid*). When using these computational tools it is necessary to study the effect of the modelling effort on the results. For this reason, the first stage is intended to compare different modelling approaches and provide a fixed reference for the rest of the project. Stage 2 is the main body of the investigation where most of the results are generated. Lastly, stage 3 applies the conclusions of S2 to different test cases to asses the generality of the results. This is shown schematically in Figure 3.1.

3.1.1. Stage 1: Effect of the interface rotor-diffuser

Project stage 1 (S1) objective is to determine the influence of modeling on the results. Several modelling approaches where compared:

[1] As a mater of fact, the implementation of this low order model was started as a streamline curvature Matlab solver. However, when it was realized the deep lack of knowledge about the outlet flow structure and their relation to turbine design parameters the low order model was abandoned (it was missing too many inputs and it was not going to add anything to a regular UIM, Section 3.2).

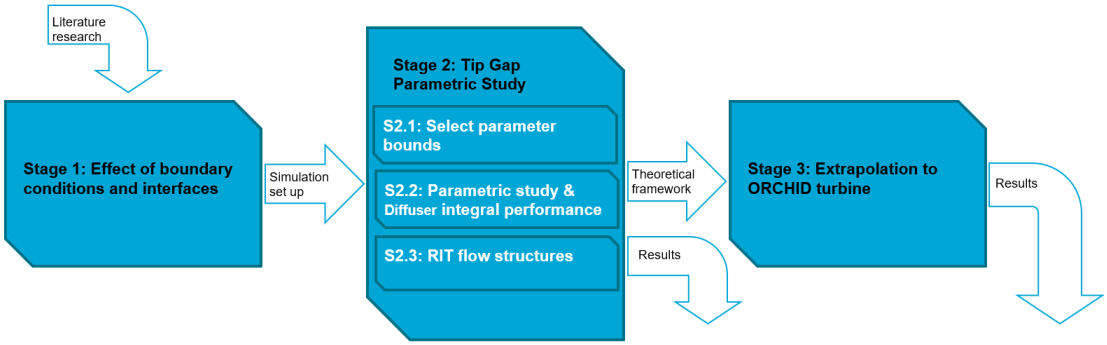

Figure 3.1: Schematic of the structure of the thesis work in terms of project stages (S)

- Isolated diffuser with uniform boundary conditions.
- Isolated diffuser with boundary conditions extracted from a rotor simulation.
- Coupled simulation Rotor+Diffuser with mixing plane interface.
- Coupled simulation Rotor+Diffuser with frozen rotor interface.
- Coupled simulation Stator+Rotor+Diffuser with mixing plane at the Stator-Rotor interface.

In this stage the averaging algorithms (Section 3.4) are implemented and tested, and the basic post-processing workflow is established.

3.1.2. Stage 2: Tip Gap parametric Study

Project stage 2 (S2) objective is to determine the influence of tip gap size distribution on the performance of the diffuser. This is done through 3 sub-tasks:

1. Detect the ranges of interest and draw basic conclusions to drive a comprehensive study.
2. Set up a test matrix based on previous conclusions. Run simulations[2] and post-process results: Analyse diffuser integral parameters.
3. Analyse turbine flow structures and seek relations to the obtained diffuser performance trends.

All of these activities will be done applying the results of S1.

3.1.3. Stage 3: Generalization

Stage 3 (S3) objective is to determine the generality of the previous results. To achieve this, a in-house design for a high pressure ratio, dense organic fluid turbine is analysed (Section 4.5.1). The operating regime (both fluid and Mach number) and design considerations of this machine are very different to the baseline study case, and thus it is a good test for the conclusions obtained from S2.

3.2. Diffuser Calculation Techniques

Low order methods

The challenge in obtaining low order models of diffusers is always related to the boundary layer behaviour in an adverse pressure gradient. Optimal diffusers are operating with stalled regions, but, even if the flow is attached, boundary layer growth must be accurately predicted due to the great impact it has on the effective flow area, A_{eff}.

There is an extensive selection of literature about this topic, and a comprehensive summary can be found in the review by Johnston (1998, [37]). Most methods can be grouped under the name of *Unified Integral Methods* (UIM) and they were greatly developed by the Stanford research group during the last century. An uniform inviscis core is assumed and an integral model of the boundary layer is solved simultaneously. The most refined methods can compute beyond the stall point, and they are more accurate than modern high order simulations when they are properly calibrated. However, these methods are restricted to a specific kind of flowfield, and they rely on a lot of data. The great advantage of these methods is that they are quick, what allows extensive parametric studies.

One of the latest additions to this family of tools is is by Mimic (2020)[6]. They implement a code very similar to those described by Johnston[37] and include the effect of tip vortexes coming from an upstream turbine. They adapt the diffuser computation method from Bardina [38], including the effect of a Lamb-Oseen Vortex. This is done by computing the strain-rate distribution of the vortex and assuming that the vortex is located with its maximum shear stress point at the edge of the boundary layer. This viscous force is incorporated into the integral momentum equation. In addition, some correlations are used to include the transfer of mass-flow between the vortex and the boundary layer. The model is highly calibrated (vortex decay, entreinment rate, effect of vortex friction...) to match the experimental results. Note that they did not measure the vortex decay in the experimental rig. The vortex strength is adjusted following the Σ correlations they found in previous publications [20][21][9](Section 1.2). Once the model is calibrated, they make a sensibility study with this low order model and determine that the main stabilising effect is the mass entraeinment.

[2]The newest TUDelft High Performance Computer (DHPC), DelftBlue [36], was an indispensable tool to carry out this task.

However, this model is not in agreement with some experimental results introduced previously (Section 1.1.3, on the effect of plasma-induced vortexes[26]). One of the main hypothesis deriving the model is that the only component of the vortex affecting the boundary layer development is the circumferential one. This is analogous to classical wall-jet experiments, and they propose that the viscous forces between vortex and boundary layer ”drag” the later. However, it is not clear that boundary layer stabilization phenomena can be explained by completely neglecting the axial component of vorticity.

Due to the lack of data it was not possible to develop such a method in this work.

Computational Fluid Dynamics

Diffuser flows are challenging and thus they are usually used for bench-marking turbulence models. The first Computational Fluid Dynamics (CFD) specific publication found is by Vassiliev et al. (2002, [39]). They test several turbulence models (all of them variations of $k-\varepsilon$) with Fluent's 2D steady state solver. They present correct grid convergence studies and the boundary layers are solved without wall functions. They use experimental boundary layer profiles as inlet boundary conditions and both velocity and turbulence quantities vary along the radius. They point out that the detailed flowfield structure is very sensitive to the turbulence model employed, and the accurate value of C_p is not predicted by any model. However they find that the ΔC_p caused by small geometrical or operation conditions perturbations is accurately predicted. This same group will perform another study in annular diffusers with struts[17] and they will conclude that even tough the flowfield is not accurately predicted, integral performance coefficients can be consistently estimated by CFD using $k-\varepsilon$ models.

Later, Kozulovic and Röber (2006, [40]) establish $k-\omega$ as a superior turbulence model for internal flows and also develop a variation to take into account the changes in turbulence due to streamline curvature. The matching with experimental data that they achieve is remarkable.

The work presented in Kluß et al. (2009)[41] is very pertinent for the topic of this project. They intend to replicate the effects of the wakes and secondary flows of the turbine over the diffuser. To do this, they simulate the experimental set up introduced in Figure 1.4 and Section 1.2 (with the cylindrical spokes) with Ansys CFX-10.0. They compare different modelling approaches and grids. Several turbulence models are compared: $k-\varepsilon$, $k-\omega$ SST (Shear Stress Transport) and SAS-SST (Scale Adaptive Simulation). They detect that $k-\varepsilon$ is the least accurate model for internal flows. On the other hand, SST is the most precise model. When the flow detaches in the diffuser, even Unsteady Reynolds Average Navier-Stokes (URANS) simulations fail to capture the time dependencies of the large eddies. Given that Large Eddy Simulations (LES) are too expensive, they employ a SAS approach[3]. They conclude that when the spoke wheel (Figure 1.4) is not included SST is the best approach and the extra cost of SAS is not justified. However, when the spoke wheel is introduced $SST-SAS$ is the only model able to predict the trends and an unsteady model is required[4]. The implications of these results are that, for non-stalling blades with thin wakes, it is not necessary to use scale resolving methods. Lastly, they point out that mixing plane models are unable to predict the phenomenology, and at least frozen rotor approaches are needed.

In the following years some authors continue using $k-\varepsilon$ models with relative success (Vassiliev, 2010 [18]). However the majority of the authors (for instance, [42][27][43][44]) use $k-\omega-SST$ Reynolds Average Navier-Stokes (RANS) models. Mimic [6] is the only researcher using SST-SAS, and he is related to the same group of Kluß. However, every researcher points out that the accurate prediction of the separation point is challenging and they only do steady state simulations.

The general conclusion is that no RANS model will be able to accurately predict the separation point and conditions for a diffuser. However, the sensibility of integral performance metrics to geometry perturbations is captured. Regarding the best turbulence model to use, any well calibrated model for that specific flow will perform similarly, but $k-\omega-SST$ RANS is generally accepted as the best *off-the-shelf* choice. This turbulence model is the one employed in this research.

[3] SAS is a combination of LES and URANS models, reducing the computational cost

[4] Note that the cylinders have thick wakes with more vorticity and large scale vortexes than a real, non-stalled blade. The advantages of the unsteady simulations are not clear in a more realistic case. They point out that the phenomena they are seeing is the mixing of the wakes. The simulated case does not have tip vortexes, and [4] show that the vortex could be more influential.

3.3. CFD set-up

The CFD solver selected for the project is *Ansys CFX*. This solver is a product of the simulation software company *Ansys*. It is marketed as a turbomachinery specific solver, and it integrates seamlessly with the meshing tool *Turbogrid*, the preprocessing tool *Ansys-pre* and the postprocessing tool *Ansys-post*.

All simulations carried out are RANS (Reynolds Averaged Navier-Stokes). This is a simplification of the Navier-Stokes equations that makes a time average and solves a steady problem in a relatively coarse mesh *modelling* turbulence. The result of these kind of simulations are very sensitive to the turbulence model applied. In the case of internal flows the typical choice is the *Shear Stress Transport* model (SST). This model, created in the nineties by Menter [45], is a combination of two previous *two-equations* models: $k-\varepsilon$ is used in the free-stream far away from the walls and $k-\omega$ is activated near the boundary layers. The name ”two equation model” makes reference to the fact that the turbulence is modelled by means of two additional transport equations that are solved simultaneously with the Navier-Stokes equations.

The grid close to the walls was fine enough[5] as to solve all velocity gradients without using wall models. See Figure 3.2, $y^+ < 5$ in all the computational domain and $y^+ < 2$ in every region of interest. y^+ takes maximum values at the inlet of the rotor where the shear stress due to scraping is maximum. Table 3.1 gives numerical results for y^+ for a typical simulation. The fluid is modelled as an ideal gas with constant viscosity.

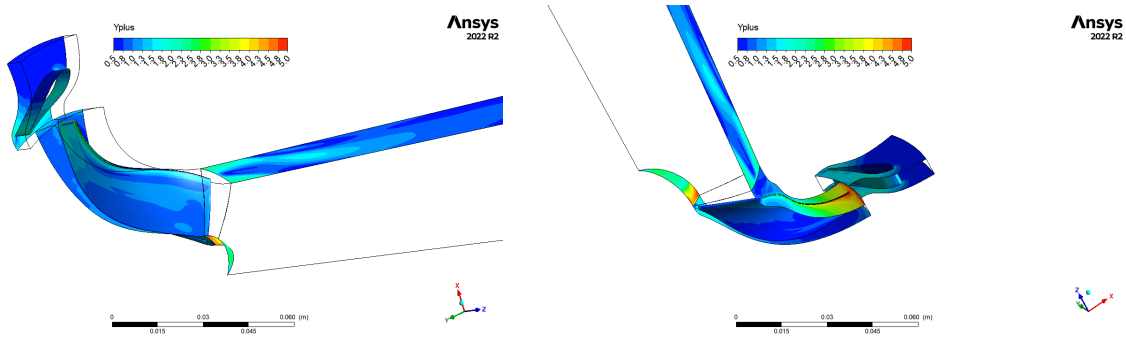

Figure 3.2: Value of y^+ in all solid walls. Typical result for the parametric study on the T-100 turbine.

Table 3.1: Values of y^+ in a typical run of the T-100 turbine (This is uniform tip gap equal to 4% leading edge span).

		min	Avr	max
Stator	Hub	0.019	0.83	2.25
	Shroud	0.019	0.84	2.25
	Blade	0.019	1.22	2.59
Rotor	Hub	0.01	0.959	2.17
	Shroud	0.45	2.44	7.07
	Blade	0.01	1.01	5.97
Diffuser	Wall	0.06	1.32	3.22
	Spinner	0.75	3	5.4

The numerical settings were the same in every simulation. Ansys offers three options for the numerical discretization of advection terms and turbulence transport equations: *First Order*, *High Resolution* and *blend*

[5]This is assessed with the size of the first computational cell in *boundary layer inner units*. The turbulent boundary layer height is measured in terms of $y^+ = \frac{y u_\tau}{\nu}$, with ν the dynamic viscosity of the fluid and $u_\tau = \sqrt{\frac{\tau_w}{\rho}}$ the boundary layer characteristic velocity. τ_w is the shear stress at the wall. Turbulent boundary layer measurements show that bellow $y^+ \approx 3$ the *viscous sublayer* is found. Here $u^+ = \frac{u}{u_\tau} = y^+$ and thus no more computational cells are required to solve the velocity gradient.

Table 3.2: Summary of *Ansys* numerical settings used throughout the project.

Option	Value
Advection Scheme	*High Resolution*
Turbulence Numerics	*First Order*
Min Iterations	1000
Max RMS	$5{\cdot}10^{-6}$
Time Scale Control	*Auto*
Length Scale Control	*Conservative*
Boundary Conditions	$(P_t, T_t)\ -\ (P)$
Turbulence BC	*Medium (Intensity 5%)*

factor. Every option is an upwind discretization of the gradients. First Order is the standard discretization, which introduces a lot of numerical dissipation in discontinuities as shockwaves. On the other hand, High order implements an (unknown) non linear blending factor between a first order and a second order upwind scheme. This option resolves better discontinuities but it might be prone to numerical oscillations. The third option allows the user to set a fixed uniform blend factor. High Resolution scheme was used for the advection terms and First Order was used in the turbulence transport equations. Ansys hides CFL number to the user. The options *Auto time scale* and *Conservative length scale* were chosen. The code will manage CFL number based on these settings. Lastly, a maximum root mean square (RMS) value was selected for all residuals as convergence criterion. This was $rms < 5{\cdot}10^{-6}$. A minimum number of a thousand iterations was also provided to ensure the departure from initial conditions[6]. The boundary conditions were given as P_t and T_t at the inlet and P at the outlet. The exact values of these are discussed in Section 3.5. Turbulence boundary conditions are provided as *"medium (Intensity 5%)"* All of this information is summarised in Table 3.2.

Ansys CFX offers different *domain interfaces* for turbomachinery application. These are:

- **Periodic Interface:** Two boundaries of a domain are periodic if they simulate infinite repetition of this domain. This imply that fluxes leaving one boundary will enter the domain through the other boundary. In turbomachinery this is used to model the whole annulus by only computing one blade channel.
- **Conservative Interface Flux:** This interface is used to join to grids that are not aligned. The solver interpolates one grid onto the other and the simulation proceeds as if these interfaces were a single grid surface. This is used in the tip gap cavity (Section 3.5) as an *Internal Interface*.
- **Sliding Interface:** This is similar to the previous interface. It is used between stator and rotor cascades in unsteady simulations. At every time-step, the flow is interpolated from one domain to the other.
- **Frozen Rotor:** This is a steady state model for turbomachinery applications. The steady flowfield is solved for a given angular offset between domains. All flow structures are convected through this interface. This model will be used in the Rotor-Diffuser interface in this work.
- **Mixing Plane:** It is the most common interface between turbomachinery rows in steady state. The mixing plane makes a pitch-wise average of the flow. The structures are not convected between blade rows, but this model is intended to simulate the time average result of an unsteady case. In this work this option will be always used for the Stator-Rotor interface.

The different usage in the project, and effects of the interface model in the rotor-diffuser boundary are discussed in Section 4.1.

[6] Along the project very similar configurations will be tested and thus previous results will be used as initial conditions. A minimum number of iterations is required to allow the propagation of the small changes along the computational domain.

3.4. Averaging methods

Turbomachinery flow-fields, and in general *internal flows*, are characterised by highly non-uniform flows [28]. This posts a practical problem to engineers, as they seek a low order representation of the problem, possibly with a single value characterising it. In the process of averaging the complexity of the flow is reduced. Some characteristics are conserved through the averaging methods and other information is lost. This is unavoidable: no uniform flow will contain all the information from the original case [46]. The challenge is choosing the correct method and knowing which information can be obtained in every situation. This section is based on Greitzer's *Internal Flow* book[28].

3.4.1. Area Average

Averaging magnitudes weighting them by area is a straightforward idea and quite convenient in experimental set ups. The algorithm is:

$$\overline{\psi}^A = \frac{1}{A}\int \psi dA \tag{3.1}$$

Note that this method will conserve the pressure forces. However, this procedure does not conserve energy between the non-uniform state and the averaged flow. A major flaw of this scheme is that it gives high importance to big regions with relatively small flow, and thus it misrepresents their influence on the physical problem. Note that in general the averaged quantities do not follow fundamental laws between them: area averaging two different stations can violate the conservation of mass or momentum, and equations of state are not guaranteed to be matched in the averaged quantities[7]. Finally, area averaged quantities conserve volumetric flow, but not mass-flow.

3.4.2. Mass Flow Average

Weighting the average with the mass flow represents the physical process of convection. The method is:

$$\overline{\psi} = \frac{1}{\dot{m}}\int \psi \rho \vec{u}\cdot d\vec{A} \tag{3.2}$$

Note that this expression conserves the flow of energy: $\dot{m}C_p\overline{T_t} = C_p\int T_t\rho\vec{u}\cdot d\vec{A}$. However, the pressure forces are not captured accurately. This averaging method is widely used because it carries the concept that it is *matter* what *contains* the fluid properties. This characteristic eases the tracking of total quantities. Regarding the static ones, pressure is usually almost uniform due to force balances, and static temperature non-uniformities are highly correlated to energy fluxes. This makes these properties easier to represent with any averaging procedure. Lastly, the averaged velocity conserves momentum flux in uniform density flows[8].

3.4.3. Mixed Out Average

This method differs from the previous ones in the sense that it is not a direct averaging of the flow. This average computes the flow properties after a prescribed process of mixing, and thus it is representative of the state that would be obtained after *physically* removing the non-unniformities. Note that mixed out averages generate an increase of entropy, so that the obtained averaged entropy is not representative of the one in the *real* flow.

It is necessary to define how the mixing will happen. In this text it is assumed that this happens at constant area. Equilibrium implies that there is no inner viscis forces:

$$u_x(r,\theta) = U_0 \tag{3.3}$$

$$u_\theta(r,\theta) = B\cdot r \tag{3.4}$$

i.e. a solid body rotation. Note that cylindrical coordinates are used in the following. A uniform static temperature distribution is also required for equilibrium:

$$T(r,\theta) = T_0 \tag{3.5}$$

[7] $\overline{\rho}^A = \frac{1}{A}\int\rho\cdot dA = \frac{1}{A}\int\frac{P}{R_gT}\cdot dA \neq \frac{\frac{1}{A}\int P\cdot dA}{R_g\frac{1}{A}\int T\cdot dA} = \frac{\overline{P}^A}{R_g\overline{T}^A}$

[8] This is, uniform temperature low subsonic flows, which are quite common in practice.

Lastly, the static pressure distribution must balance radial forces:

$$\frac{\partial P}{\partial r} = \rho \frac{u_\theta^2}{r} = \frac{P}{R_g T_0} B^2 r \rightarrow P(r) = P_0 \exp\left\{ \frac{B^2 (r^2 - r_0^2)}{2 R_g T_0} \right\} \tag{3.6}$$

where r_0 is an inner radius that generalises the model to annular sections, and P_0 is the pressure at this point. Note that the expression can be simplified in the incompressible case.

The total quantities are obtained from:

$$T_t(r) = T_0 + \frac{U_0^2 + B^2 r^2}{2 C_p} \tag{3.7}$$

$$P_t(r) = P(r) \left(\frac{T_t(r)}{T} \right)^{\frac{\gamma}{\gamma - 1}} \tag{3.8}$$

Total and static density are computed from an equation of state, and entropy can be computed as $s = s_0 + C_p \ln\left(\frac{T}{T_0}\right) - R_g \ln\left(\frac{P}{P_0}\right)$. Note that some of the mixed out properties are non-uniform in this formulation. This is due to the retention of the angular velocity. If $B = 0$, all properties become uniform. This is a new addition to the model by the author and will be backed up in the next paragraph. When a property is non-uniform, the mass averaged value of the mixed out variable will be taken.

In order to recover information from the flow, it must be required the conservation of some properties. The previous flow model has 4 parameters. These are: U_0, B, P_0 and T_0. These are found by imposing four conservation laws between the mixed out state and the original flow: conservation of mass, conservation of energy flux (total enthalpy), conservation of linear momentum, and conservation of angular momentum[9]. Respectively:

$$\dot{m} = \int_{r_0}^{R} \rho(r) U_0 2\pi r dr \tag{3.9}$$

$$\dot{m} \overline{T_t} = \int_{r_0}^{R} T_t(r) \rho(r) U_0 2\pi r dr \tag{3.10}$$

$$\int (\rho u_{ax}^2 + P) dA = \int_{r_0}^{R} (\rho(r) U_0^2 + P(r)) 2\pi r dr \tag{3.11}$$

$$\int (\rho \cdot u_\theta \cdot r \cdot u_{ax}) dA = \int_{r_0}^{R} \rho(r) \cdot B \cdot U_0 \cdot r^2 \cdot 2\pi r dr \tag{3.12}$$

where the left hand sides are evaluated in the original flow, and the definitions of the mixed out state are substituted in the right hand side. These 4 equations form a non-linear integro-algebraic system of equations that is solved numerically. Note that the condition of constant area comes from setting up the limits of the integrals, r_0 and R, in such a way that it matches the original flow path. It is possible to integrate them analytically by dropping out the conservation of angular momentum and compressibility[28].

The great advantage of this averaging procedure is that it has strong physical basis. However, it is costly and the entropy generation in the mixing process can mask information about the original flow.

3.4.4. Comparison between averaging methods

In general, *area average* is easy to implement and thus it is common in experimental studies where the data might be sparse; *mass flow average* keeps the concept of convection and energy conservation and thus it is usually thought as the ”correct procedure” in power applications[46], and *Mixed-Out average* is computationally costly and introduces a lot of modifications to the flow, but gives information about a plausible future state. *Mass flow average* is the most common metric in literature and represents the flow adequately in the situations found along this document. However, a lot can be inferred from comparing the results between the other methods.

[9]Note: these conservation equations imply that the mixing happens without energy exchange or forces: the walls are inviscid and it is the fluid viscosity and heat conductivity what makes the flow uniform.

Area Average VS. Mass Flow Average

The comparison of these averages can give information about the existence of big, low momentum zones (i.e. recirculation zones). An example of this is shown in Figure 3.3. Area average introduces non-physical effects and the *valley* in $\overline{P_t}^A$ exactly correlates to the length of the recirculation bubble, clearly visible in b) as a dark blue region. The difference between $\overline{P_t}^A$ and $\overline{P_t}$ is informative about the size of the separated region. Note that in general $\overline{P_t}^A < \overline{P_t}$. This is because mass average gives more weight to high energy parts of the flow, thus the portion of the flow at higher P_t.

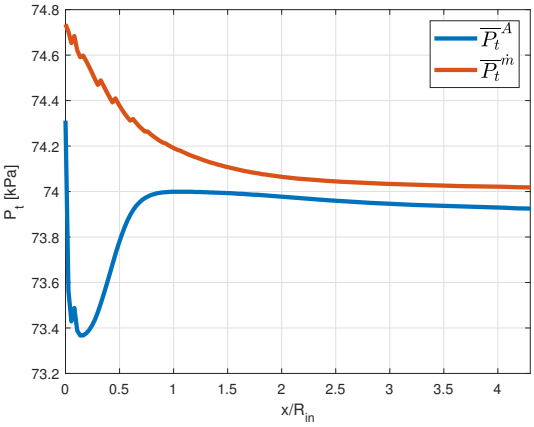

a) Difference in averaged total pressure along the diffuser.

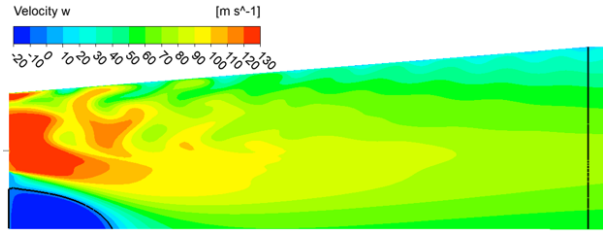

b) Axial velocity contours in an $S2$ plane. The bold black line shows $u_{ax} = 0$.

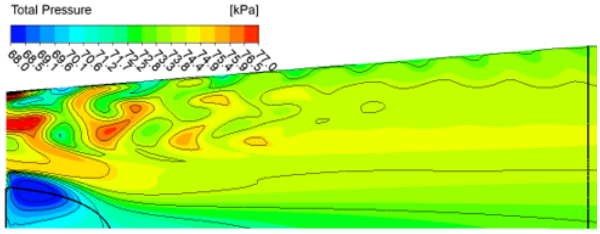

c) Total pressure contours in $S2$ plane. Red spots are high energy regions related to the intersection of coherent vortexes from the turbine.

Figure 3.3: Example of the different averaging results. The test case is introduced in detail in Chapter 3. The simulation is a radial turbine with a conical diffuser starting with an abrupt change in cross-section. RANS $k - \omega - SST$ turbulence model with frozen rotor interface.

Mass Flow Average VS. Mixed Out average

Mass flow averaged values provides an energetically accurate *snapshot* of the state of the fluid. This implies that mass averaged values represent the current entropy and enthalpy convection in the flow. On the other hand, a mixed out average *computes* the flow state resulting at the end of the mixing process.

The mixed out average of entropy at any given axial location along a mixing pipe will be very similar[10] because all mixing losses are taken into account always. However, the mass flow average will change between axial stations due to physical mixing. Then, the comparison of these two averages will reveal the mixing progress.

Figure 3.4 provides an example of this. Diffuser loss coefficient, k_{loss}, is shown. Area average can locate the recirculation zone. Regarding mixed out average, the value of k_{loss} is lower than that obtained by mass average. This is because K_{loss} is a total pressure loss with respect to the inlet conditions. Note how the difference between mass average and mixed out increases: these are the real mixing losses. Mixed out average includes the total mixing loss in every location, but mass averaging only considers the mixing losses that have already incurred. The difference between them is proportional to the mixing losses. The most meaningful metrics are given by mass averaged quantities, but the comparison of this with other averages provides insight into the processes happening in the flow.

[10] Assuming that the main effect in the real problem is mixing, heat transfer and friction is negligible

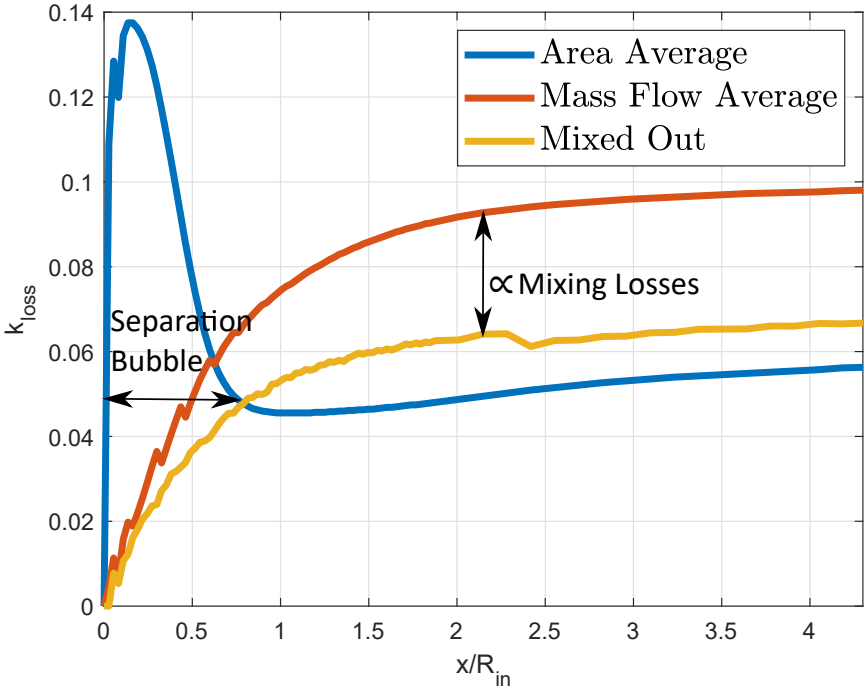

Figure 3.4: Comparison of k_{loss} with different averaging methods for the test case introduced in Figure 3.3.

3.5. Test case turbine

All work in S1 and S2 (Section 3.1) was done with the radial inlet turbine used in the Sundstrand Power Systems T-100 Multipurpose Small Power Unit. This machine was designed and tested by Jones (1996, [47]). This is a well studied open literature test case with comprehensive experimental data and which has been used as a CFD benchmark by other researchers, such as Sauret (2012, [48]).

Design Characteristics

In his paper, Jones [47] reports about the design objectives and methods followed of the T-100 RIT, as well as the experimental results. However, for this work the geometrical parameters of the turbine are taken from the paper by Sauret [48]. They reconstruct Jones' geometry and match every geometrical parameter with Bezier curves up to 1% error. This digitized data is provided by the authors. The interested reader is redirected to this reference to analyse the differences between the simulated geometry and the original Jones' design.

T-100 auxiliary power unit (APU) design objective is to provide 50 HP ($37\ kW$) wit a turbine inlet temperature (TIT, or T_{4t}) of $1056\ K$ and a mass-flow of $0.328\ kg/s$. This could be upgraded to 75 HP by increasing TIT and modifying the stator of the turbine. To provide this performance, the turbine will have to deliver $120kW$ ($365.9\ kJ/kg$) with 106588 rpm and a total to static pressure ratio of $\beta_{ts} = 5.73$. All design parameters are summarised in Table 3.3. The size of the different elements of the original machine[11] are reported in Table 3.4 and Figure 3.5 a. At design conditions, the stator is almost chocked ($M_{Stator,out} = 0.986$), the rotor is fully subsonic ($M_{w,in} = 0.26$, $M_{w,out} = 0.71$, see reference [47] to see blade Mach number distribution), and the outflow from the turbine is almost axial and subsonic ($M_{out} = 0.38$). Velocity triangles are shown in Figure 3.5 b, note that the blades at the inlet are radial and the incidence is $i = 31.4°$. The reader is redirected to the original references ([47][48]) to see the rationale behind this design decisions and the computation procedure. Detailed thickness distribution plots an another geometrical parameters are reported there too.

[11] Diffuser length is incorrect in reference [48]. They report $L = 157.5\ mm$. Unfortunately, this was not noticed at the moment of setting up the simulations and all the work exposed here is for a diffuser of $L = 157\ mm$ and $\phi = 4.61$ deg.

Table 3.3: Design objectives and duty coefficients for Jones' design. Partially recovered from [48].

Design Parameters		**Duty coefficients**	
Ω [RPM]	106588	$\psi_2 = \frac{w}{U_2^2}$	0.9
T_{4t} $[K]$	1056	$\phi_2 = \frac{v_{2m}}{U_2}$	0.2
P_{4t} $[kPa]$	580.4	α_3 $[deg]$	+1.3
$\dot{m}$ $[kg/s]$	0.328	$R_3/R_{2,mid}$	0.45
β_{tt}	5.6	v_{3m}/v_{2m}	1.51
β_{ts}	5.73		
# Stator Blades	19		
# Rotor Blades	16		
U_2 $[m/s]$	650		

Table 3.4: Original sizes of the T-100 turbine. Adapted from [48]. All lengths in $[mm]$, areas in $[mm^2]$, and angles in $[deg]$.

Stator		**Rotor**		**Diffuser**	
$R_{in} \equiv R_1$	75.1	$R_{in} \equiv R_2$	58.2	R_{in}^{Shroud}	36.8
R_{out}	63.5	h_{in}	6.35	R_{in}^{Hub}	15.2
h_{in}	6.35	h_{out}	21.6	R_{out}	49.5
h_{out}	6	L_{Rotor}	38.9	Axial Length	118.6
Chord	22.9	Total Throat Area	1909.7		
Total Throat Area	491	TE Thickness	0.76	L/R_1	3.26
TE Thickness	0.51	$R_{Scalloping}$	38.4	AR	2.2
		Clearances:		Wall Angle	6
		Axial (ϵ_{LE})	0.4		
		Radial (ϵ_{TE})	0.23		
		Seal Plate	0.33		

The geometry simulated is not an exact match with the original Jones design. The main differences are:

- The scalloping of the rotor was totally omitted.
- The stator blade height was kept constant with $h_{stator} = 6.4\ mm$.
- Inlet flow angle to the stator was $\alpha_1 = 0$ (Jones [47] reports α_1 between 20° and 40°, Sauret [48] does not mention this parameter).
- Seal plate clearance is not modelled.
- Diffuser axial length: $L = 157.5\ mm$. This implies $L/R_1 = 4.3$ and $\phi_{wall} = 4.61$. This was not intentional and due to an misleading picture in Sauret's paper [48]. Jones [47] does not directly report the diffuser length.
- The boundary conditions of the CFD were representative of the *test* conditions and not of *design* conditions.

These differences should not affect the validity of the results, and they simplified the set up of the model. The simulated sizes and boundary conditions are reported in Table 3.5. Note that these are *test* conditions in [47]. Corrected rotational speed:

$$\omega_{corr} = \omega \sqrt{\frac{T_{t,ref}}{T_{4t}}} \tag{3.13}$$

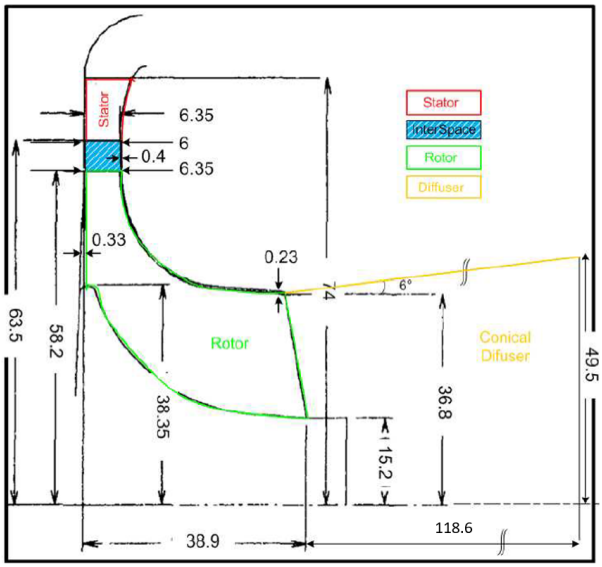

a) Meridional view of the T-100 turbine. Adapted from [48].

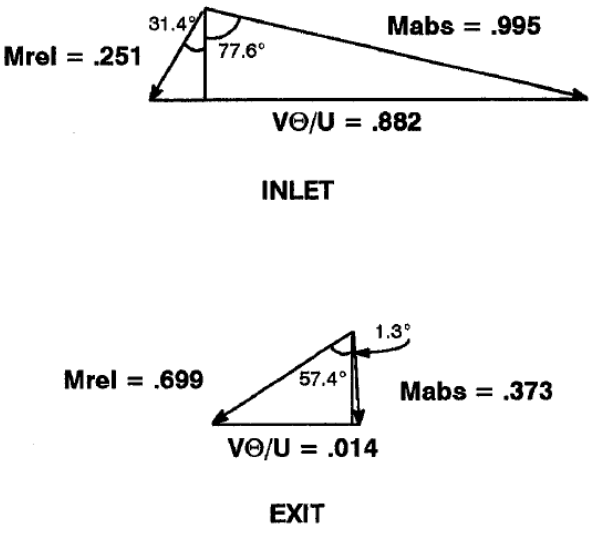

b) Rotor velocity triangles. Recovered from Jones (1996, [47]). Values are in close agreement with those of Sauret[48].

Figure 3.5: Design of T-100 radial inlet turbine.

and corrected mass-flow:

$$\dot{m}_{corr} = \dot{m}\frac{P_{t,ref}}{P_{4t}}\sqrt{\frac{T_{4t}}{T_{t,ref}}} \tag{3.14}$$

are matched to give the same $\dot{m}$, pressure ratio, and Mach numbers as in on-design conditions. Figure 3.6 and Figure 3.7 show the blade geometry used in this work.

Table 3.5: Final simulation geometry and boundary conditions. All lengths in $[mm]$, areas in $[mm^2]$, and angles in $[deg]$.

Stator		**Rotor**		**Diffuser**		**Boundary Conditions**	
R_1	74.0	R_2	58.2	R_{in}^{Shroud}	36.8	$P_{t,in}$	$413.6\ kPa$
R_{out}	63.5	h_{in}	6.35	R_{in}^{Hub}	15.2	$T_{t,in}$	$477.6\ K$
h_{all}	6.35	h_{out}	21.6	R_{out}	49.5	α_0	0 deg
				Axial Length	157.5	P_{out}	$72.4\ kPa$
R_{BC}	85.0	$R_{Mixing\ Plane}$	60.0			Turbulence	*Medium (Intensity 5%)*
		$L_{Diffuser\ Interface}$	41.0	L/R_1	4.3	RPM	71700
				AR	2.2		
				Wall Angle	4.61		

CFD mesh

Both rotor and stator grids are structured O-grids generated with *Turbogrid*. The stator domain (Figure 3.10 d) has 562 thousand nodes (539 thousand hexahedral elements) and the rotor grid (Figure 3.10 a-c) has around 1.82 million nodes (1.77 million hexahedral elements). The size of the rotor grid varies with tip gap size, the bigger this is the more nodes it has. *Turbogrid* allows the modelling of the tip gap as a linear distribution were leading edge (LE) and trailing edge (TE) gap sizes are an input (Section 3.7). The grid in the tip gap cavity is generated as two extra blocks with an interpolating interface between them. This interface follows the blade length. The refinement needed to resolve the tip gap cavity affects the whole rotor domain (Figure 3.10 c). A grid convergence study for a model with nominal tip gaps and without

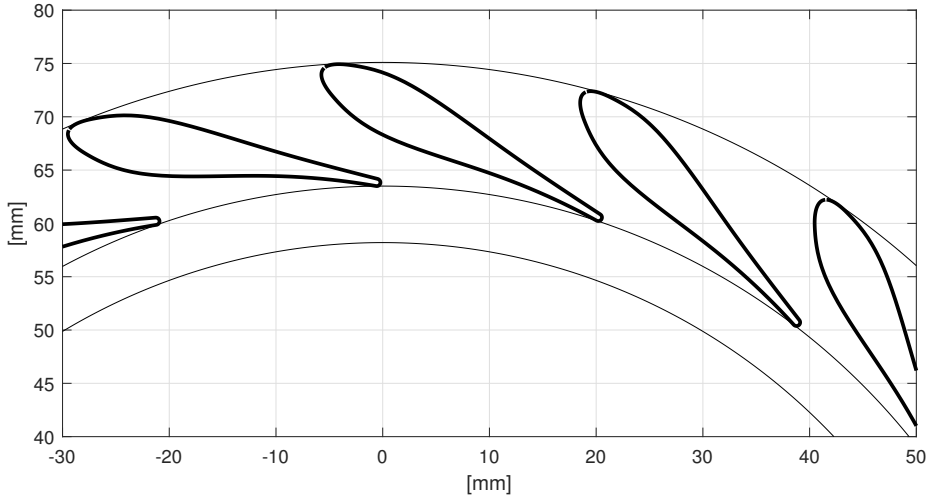

Figure 3.6: Stator geometry used in this work. The stator is a straight prism. Thin black lines represent stator inlet radius ($75.1\ mm$), stator outlet radius ($63.5\ mm$) and rotor inlet $58.2\ mm$.

diffuser is shown in Figure 3.8. The grid used in the rotor is fine enough as to predict efficiency in a ± 0.5% error band from the finest grid tested (with 2 times more nodes). See Appendix A for more information about this and the spatial order of convergence.

In every case only one stator blade and one rotor blade are simulated.

3.6. Test case diffuser

Design characteristics

The diffuser was taken from the data in Sauret (2012, [48]). This resulted in a diffuser 30% longer than that employed by Jones [47]. The design of the diffuser is very simple, being a conical pipe with inlet radius of $R_1 = 36.8\ mm$ and an outlet radius of $R_2 = 49.5\ mm$. However, the outlet of the turbine is an annular section, and in the original design [47] there is no hub casing or *spinner*. This implies that the diffuser is not purely conical, but it starts as a *dump diffuser* followed by a *conical diffuser*.

During initial testing, it was detected that the hub region is the major source of entropy and losses in the diffuser. For this reason it was decided to include an *spherical spinner* at the hub of the rotor. This element is part of the diffuser mesh, and it is given a rotating wall boundary condition. The spherical shape was chosen because it was a simple element with no parameters.

The diffuser is modelled as $\frac{1}{16}$ sector of the annulus (equal to the rotor pitch in order to ease *frozen rotor* interfaces). The computational domain is elongated 2 diffuser lengths (approximately 3 outlet diameters) downstream of the diffuser outlet to avoid boundary conditions influence on the results. The grid was stretched here to provide numerical dissipation and damp any unstable mode[6]. This extension is treated as a regular viscis wall.

CFD mesh

The grid of both diffuser models is an structured hexahedral grid generated with *ICEM*. Special care was taken to resolve the boundary layers close to the walls (Figure 3.2). The original diffuser mesh has 362 thousand elements, whereas the mesh including the spinner has 583 thousand, 36 thousand of them in the diverging section. A grid convergence study for this element is shown in Figure 3.9. k_{loss} is the best metric to asses convergence as it depends on processes more difficult to predict, such as mixing and shear layers. On the other hand, C_p depends less on the grid and it is practically insensitive to it at employed level of refinement. k_{loss} is matched with a 7% error with respect to the finest mesh, but this big relative error is due to the small value of the coefficient. More details about the grid dependencies of the present

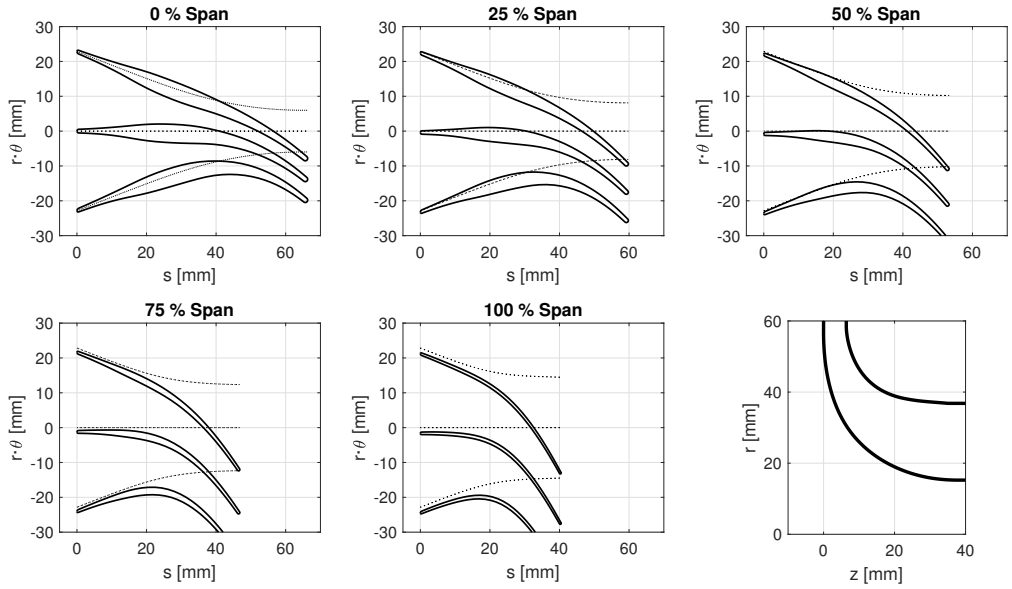

Figure 3.7: Rotor blades geometry used in this work. tangential displacement $r \cdot \theta$ is plotted against meridional distance. Dotted lines are references such that $\theta = const.$. Note that this projection deforms the angles, but it gives an impression of the real gas path magnitude.

work can be found in Appendix A. Figure 3.11 and Figure 3.12 show the details about the grid. A simulation including stator, rotor, and diffuser has around 3 million elements.

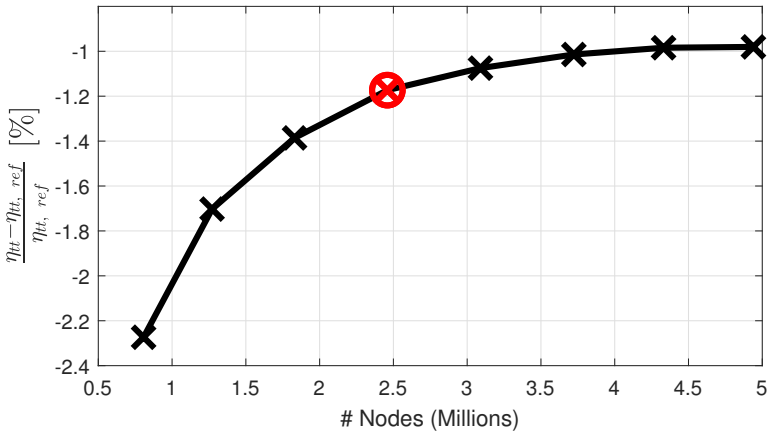

Figure 3.8: Grid independence study for the T-100 turbine. Domain without diffuser. The red cross shows the grid settings used along the project. More information can be found in Appendix A.

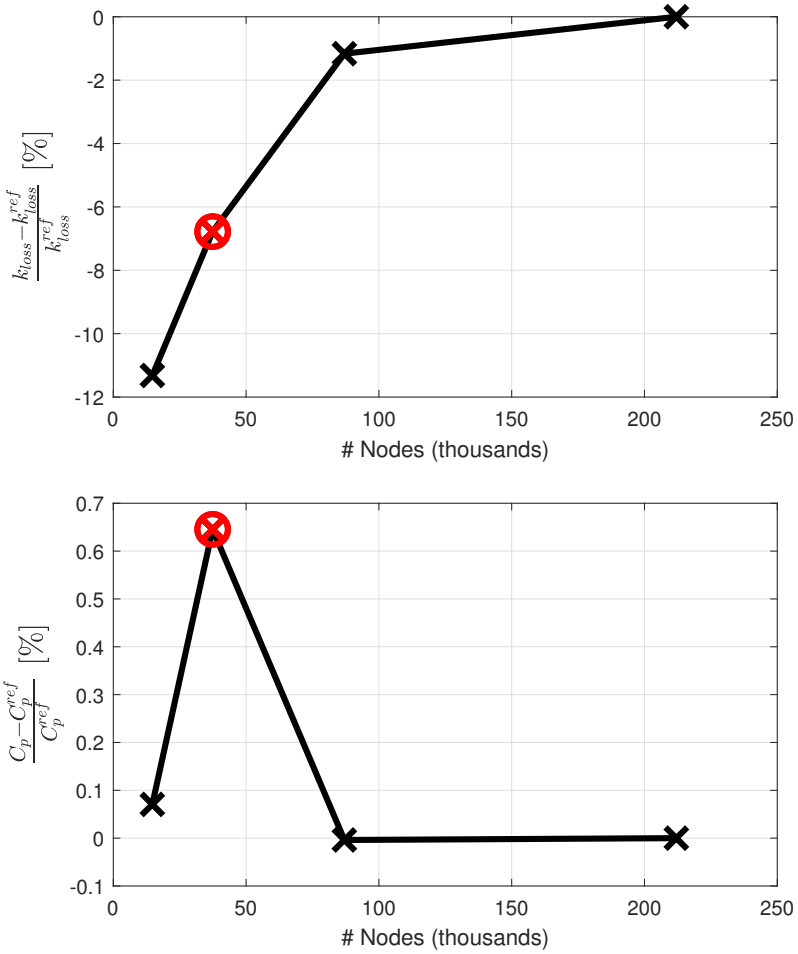

Figure 3.9: Grid independence study for the diffuser downstream of the turbine grid used along the study. Number of nodes reports the nodes *only* in the diverging section. The red cross shows the grid settings used along the project. More information can be found in Appendix A.

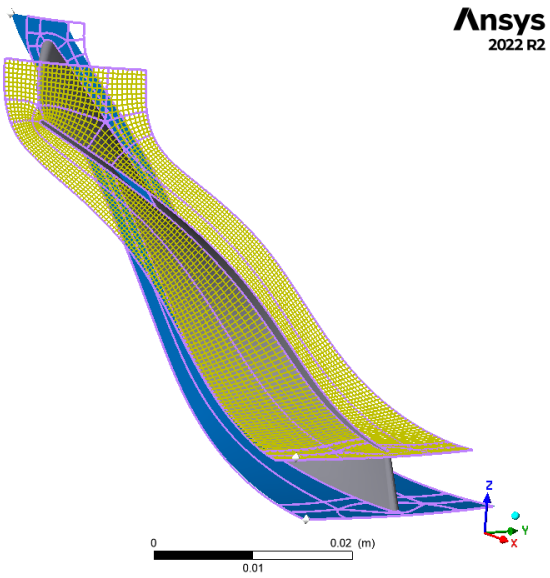

a) Rotor topology. View radially in from the inlet.

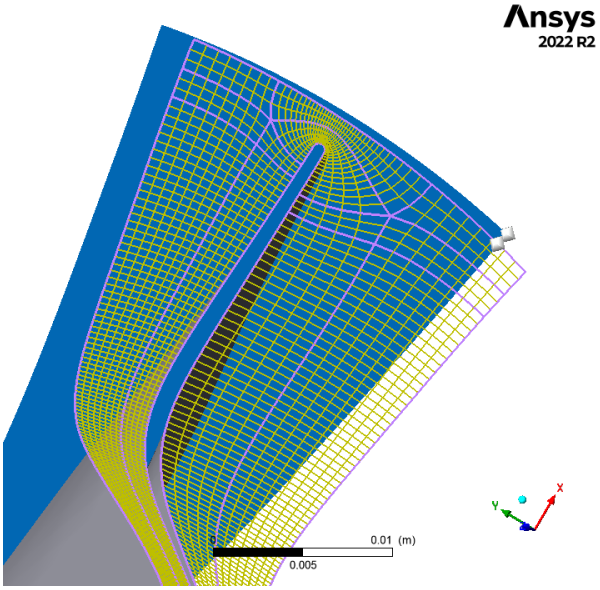

b) Rotor topology. Axial view from the outlet, detail of the leading edge.

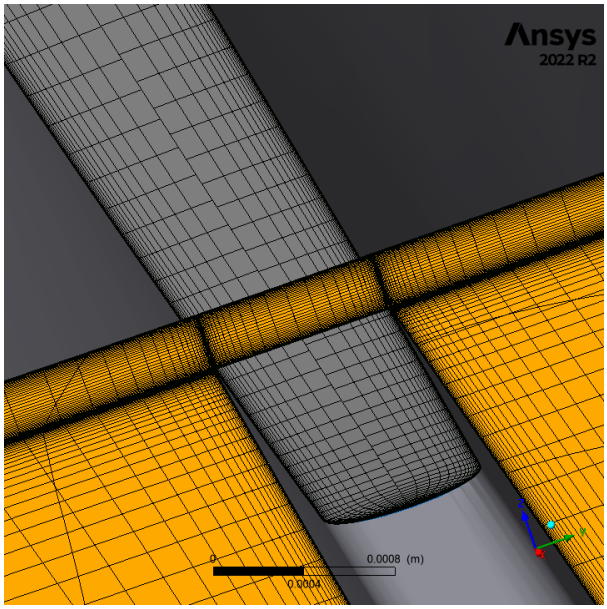

c) Rotor grid. Detail of the tip gap cavity discretization. View from the LE.

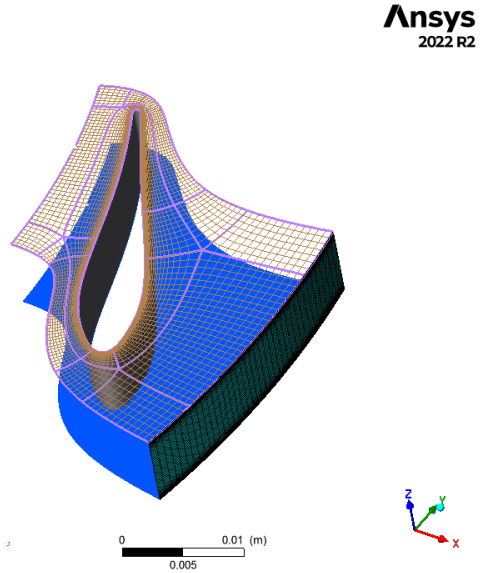

d) Stator topology.

Figure 3.10: Details of the structured computational grid for the turbine. **Stator:** 562 thousand nodes; **Rotor:** 1.82 million nodes.

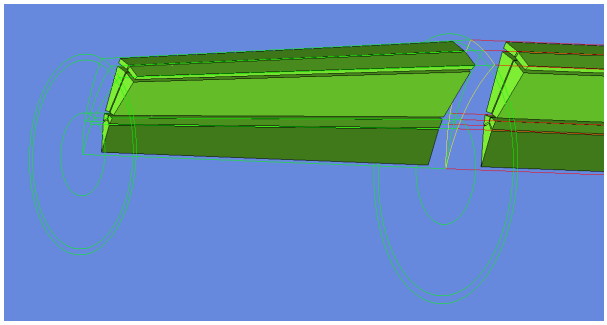

a) Blocking of the diffuser domain.

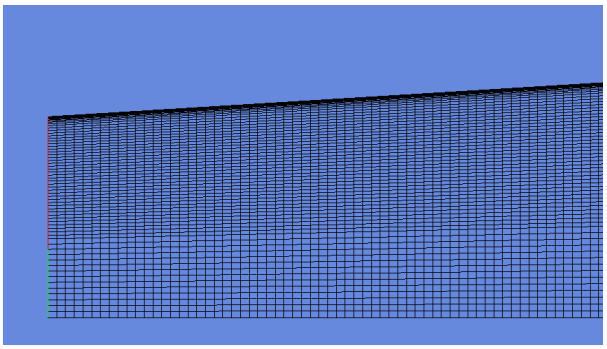

b) Side view of the diffuser grid.

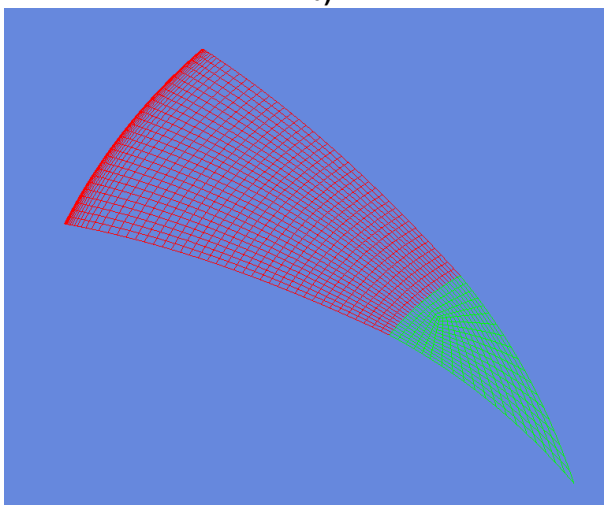

c) Detail of the grid at the inlet of the diffuser. The interface with the rotor is colored in red.

Figure 3.11: Details of the grid for the original diffuser. 362 thousand hexahedral elements, 10% of them in the diverging section.

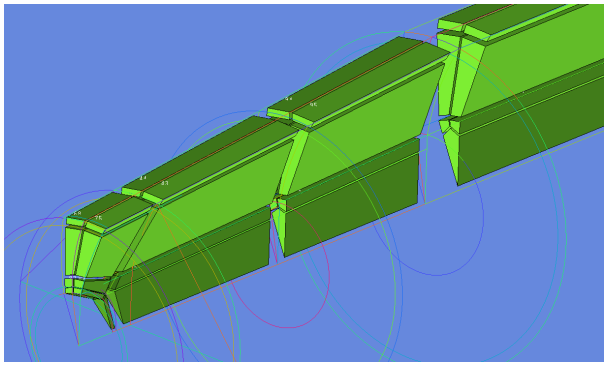

a) Blocking of the diffuser domain.

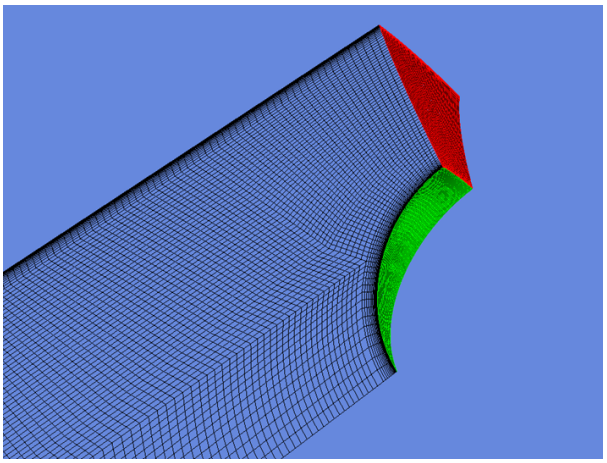

b) Side view of the diffuser grid.

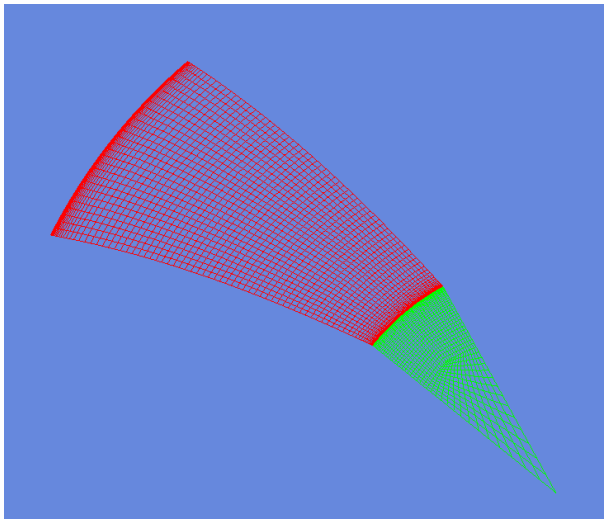

c) Detail of the grid at the inlet of the diffuser. Orthogonal view.

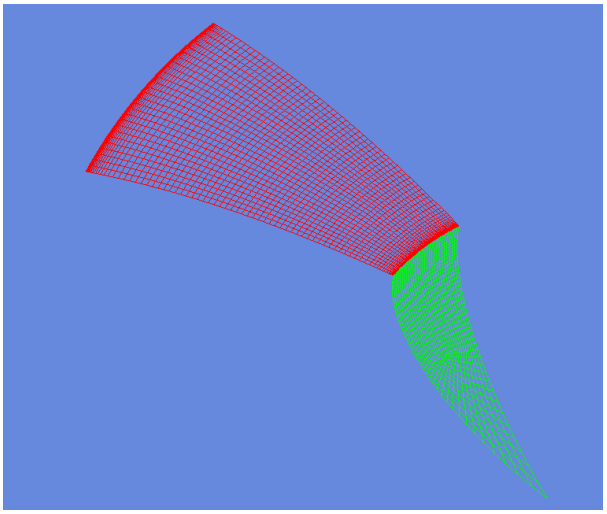

d) Detail of the grid at the inlet of the diffuser. Perspective view.

Figure 3.12: Details of the grid for the diffuser including the spinner. 583 thousand hexahedral elements, 10% of them in the diverging section.

3.7. Test Matrix

Turbogrid models tip gap clearance as a linear variation between the value at the leading edge (LE) and the value at the trailing edge (TE). During S1 and S2.1 it was noticed that it was useful to study the interaction phenomena in terms of tip gap average size and tip gap variation. This defines the tip gap with two non-dimensional parameters:

$$\epsilon_{Avr} = \frac{\epsilon_{LE} + \epsilon_{TE}}{2h_{LE}} \tag{3.15}$$

$$\Delta_\epsilon = \frac{\epsilon_{TE} - \epsilon_{LE}}{\epsilon_{Avr} \cdot h_{LE}} \tag{3.16}$$

Where ϵ_j is the tip gap size (measured perpendicular to the casing in that location), and h_{LE} is the span at the leading edge. This was chosen as a normalizing value out of convenience. The second parameter, Δ_ϵ, is a compact way of knowing if the gap is *increasing* or *decreasing* and how much. During the initial testing it was noticed that the local non-dimensional tip gap size $\frac{\epsilon_j}{h_j}$ was only meaningful for local rotor entropy generation, but not to characterise the interaction with the diffuser.

It was found that the interesting range of study was:

$$0 \leq \epsilon_{avr} \leq 10\%$$

$$-50\% \leq \Delta_\epsilon \leq +50\%$$

Note that the original design (Table 3.4) is: $\epsilon_{Avr} = 5\%$, $\Delta_\epsilon = -54\%$.This design space was explored in a combinatorial[12] manner, resulting in 35 test points, plus 1 with $\epsilon_{Avr} = 0$, and another one simulating a shrouded rotor (the casing moves with the rotor). This is shown in Table 3.6

Table 3.6: Test matrix involved in S2.2. $h_{LE} = 6.35$, tuples such that $(\epsilon_{LE}, \epsilon_{TE})$ in mm. Additionally to this there are two more data points with $\epsilon_{LE} = \epsilon_{TE} = 0$ (see text).

		Δ_ϵ %						
		-50	-20	-5	0	+5	+20	+50
ϵ_{Avr} %	1	(0.0794, 0.0476)	(0.0699, 0.0572)	(0.0651, 0.0619)	(0.0635, 0.0635)	(0.0619, 0.0651)	(0.0572, 0.0699)	(0.0476, 0.0794)
	2	(0.1588, 0.0953)	(0.1397, 0.1143)	(0.1302, 0.1238)	(0.1270, 0.1270)	(0.1238, 0.1302)	(0.1143, 0.1397)	(0.0953, 0.1588)
	4	(0.3175, 0.1905)	(0.2794, 0.2286)	(0.2604, 0.2477)	(0.2540, 0.2540)	(0.2477, 0.2604)	(0.2286, 0.2794)	(0.1905, 0.3175)
	6	(0.4763, 0.2858)	(0.4191, 0.3429)	(0.3905, 0.3715)	(0.3810, 0.3810)	(0.3715, 0.3905)	(0.3429, 0.4191)	(0.2858, 0.4763)
	10	(0.7938, 0.4763)	(0.6985, 0.5715)	(0.6509, 0.6191)	(0.6350, 0.6350)	(0.6191, 0.6509)	(0.5715, 0.6985)	(0.4763, 0.7938)

[12] It is possible to explore the design space in a more efficient manner, as for instance using polynomical surrogates and sparse grid techniques. This would be useful to obtain $C_p(\epsilon_{Avr}, \Delta_\epsilon)$, but it was preferred to have more data points allowing for a more detailed study of the flow phenomena.

4

Results

4.1. Comparison of different modelling approaches for turbine-diffuser flows

There are not detailed measurements about the *real* flow-field, neither experimental [47] or computational [48]. For this reason this discussion will be mainly qualitative. It is known (Section 3.2) that no CFD simulation can exactly reproduce the real flow-field in a diffuser. However, unsteady simulations (uRANS) and frozen rotor (RANS) models can adequately capture the main flow characteristics. Given the big computational cost of uRANS simulations, and the large test campain conducted in this research, RANS simulations are employed. Furthermore, a *frozen rotor* simulation is taken as the reference flow throughout this section.

Three different configurations for the rotor tip region were tested:

- Nominal tip gap distribution, based on Table 3.4.
- Zero-tip-gap, with counter-rotating shroud wall.
- Shrouded rotor, with co-rotating shroud wall[1].

Each of these models were combined with the following rotor-diffuser interface:

- Mixing plane.
- Frozen rotor.

In addition, an isolated diffuser with uniform inlet and boundary conditions taken from the frozen rotor simulation was also tested. This makes a total of 7 cases. Note that the diffuser used throughout this section is the one without spinner (Figure 3.11). Furthermore, the computational domain did not include the stator, and the rotor inlet swirl was set according to data from Jones 1996 [47]. Losses at the stator were not taken into account, and thus all simulations in this section are slightly off-design.

4.1.1. Meridional flowfield

Figure 4.1, 4.2 and 4.3 show the meridional plane of the diffuser. Each column shows a different flow magnitude and each row a different rotor configuration. Different figures are different interfaces. All plots contain a black bold line representing the contour $u_x = 0$. This was taken as a qualitative measure of the recirculating region. Note that the recirculating region is *bigger* than this contour because there is a shear layer in between. The high loss region (red) in k_{loss} plots highlights the region of separating flow.

[1] From now on, "*Zero Tip Gap*" will make reference to the case with counter-rotating shroud, and "*Shrouded Rotor*" will be always explicitly called.

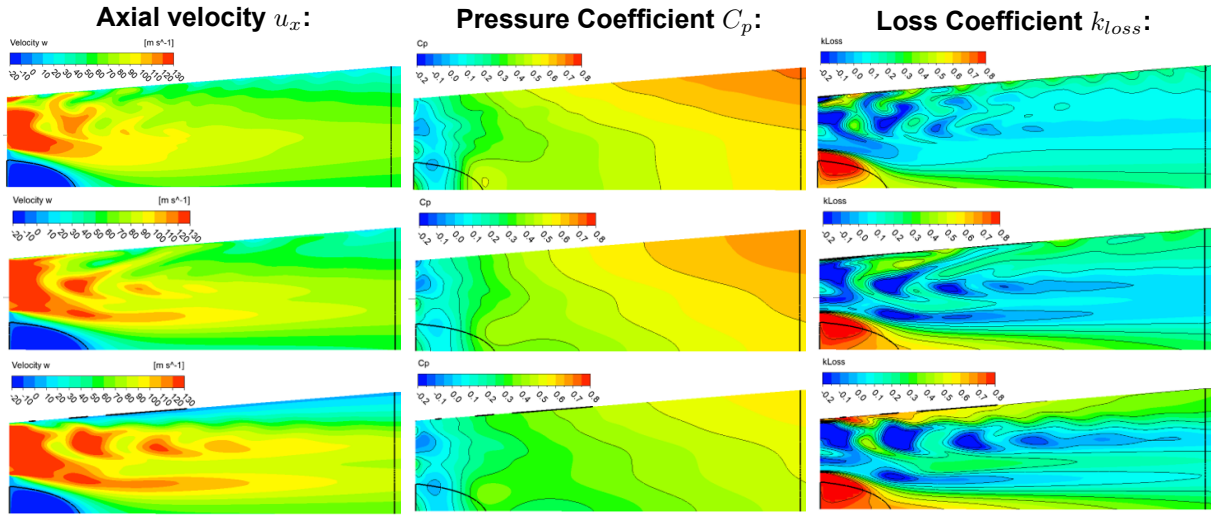

Figure 4.1: Meridional view of the diffuser for different rotors and ***frozen rotor*** interface.
Each row is: **1.** Nominal rotor, **2.** Zero tip gap, **3.** Shrouded rotor.

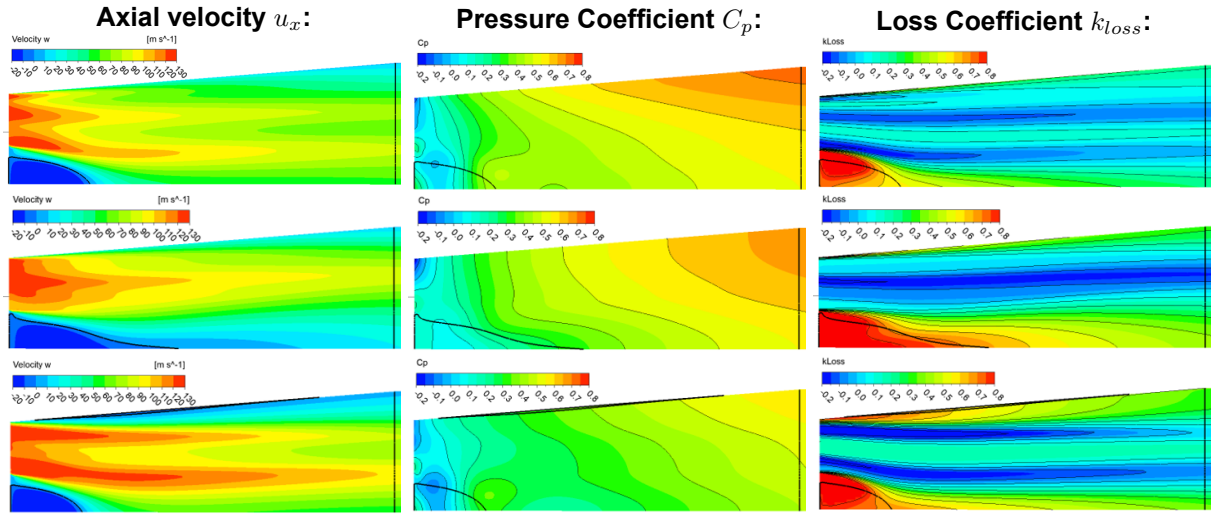

Figure 4.2: Meridional view of the diffuser for different rotors and ***mixing plane*** interface.
Each row is: **1.** Nominal rotor, **2.** Zero tip gap, **3.** Shrouded rotor.

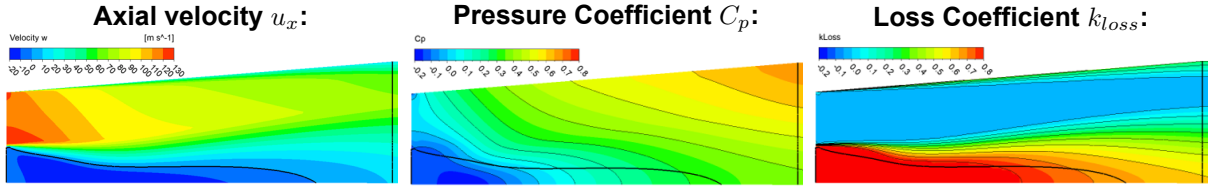

Figure 4.3: Meridional view of the diffuser for ***unifrom inlet*** boundary condition.

Frozen rotor
The flowfield in Figure 4.1 is taken as the *reference* one because it is the one containing the most flow structures. All of them show similar recirculating regions, except the *zero tip gap* rotor, which is slightly bigger. u_x and k_{loss} plots show high energy regions corresponding to the intersection of turbine passage cores with the meridional plane. This shows that the flow in the diffuser is swirling.

The configurations without tip gap are characterized by low loss regions in the core of the diffuser, which are convected to longer distances downstream of the rotor exit section. Lastly, the static pressure distribution (C_p) is similar in all cases. The radial gradient in C_p is due to the swirl of the flow.

Mixing Plane
Figure 4.2 contains the results for mixing plane simulations. As expected, the flowfield is tangentially uniform and part of the previous non-uniformities are lost. However, radial variations and swirl are retained in the flow. The major difference in the hub region is found for the *zero tip gap* case, where the recirculation zone extends further downstream. This was not investigated further.

The static pressure field is qualitatively and quantitatively (Figure 4.4) comparable to the reference case. However, the energy fields (u_x and k_{loss}) deviate more from it. High energy regions extend longer than what they should because the pitch-wise average smooths the gradients and thus reduces dissipation.

Uniform inlet
Figure 4.3 shows the results for uniform inlet simulations. The boundary conditions are such that the mass flow and stagnation inlet conditions are matched. The flowfiels are largely dissimilar to the reference case. The recirculation region is larger, leading to greater losses than expected at the diffuser outlet section. Despite the uniform inlet model is able to capture correct values of the pressure recovery coefficient, the poor capability in reproducing accurate predictions of the overall losses in the diffuser made it unsatisfactory for the current investigation, and it was therefore discarded.

4.1.2. Diffuser performance
Figure 4.4 shows the evolution of C_p through the diffuser length. Both *frozen rotor* and *mixing plane* interfaces predict a very similar C_p trend for the rotors with scraping. The pressure recovery for the shrouded rotor is worse due to the blockage induced by stall at the inlet. The simulation with uniform inlet shows the same trend as shrouded rotor at the beginning, but it becomes unrepresentative of any realistic case after one rotor outlet radius. This plot shows that: a) static pressure trends are captured by *mixing plane* interfaces, and b) shroud flow structures are important in the prediction of C_p trends, and scraping is enough to generate this behaviour in static pressure.

This plot also shows ideal references as gray lines. The dotted line is the C_p obtained as $C_p = 1 - \frac{1}{AR^2}$ (Equation 2.1), while the other lines corresponds to the combination (Equation 2.3) of a sudden expansion mixing process ($C_p = 2\left(\frac{1}{AR} - \frac{1}{AR^2}\right)$, Equation 2.2) followed by a regular ideal expansion. Different lines represent different lengths where the mixing is assumed to have finalised. Note how $x_{mix}/R_1 \approx 1$ matches the averaged data and the length of the recirculation bubble (Figure 4.1 and Figure 4.2) for the unshrouded cases. The great difference between these lines and the shrouded rotor was not investigated, but it is thought to be related to the boundary layer separation. In the case of uniform inlet, the sudden expansion region and the regular diffuser flow region is not clearly delimited. It is possible that in this case the long recirculation bubble acts as an inner wall and both processes happen in parallel.

Figure 4.5 contains K_{loss} distribution along the diffuser. The spread in value and shape of the curves is important. *Mixing plane* interface always under-estimate losses, and the trend is more linear than with *frozen rotor*. *Frozen rotor* predicts most of the losses at the inlet. It is in this region where the flow is the least uniform and the recirculation zone is located.

These results highlight the importance of the mixing processes in the diffuser to accurately predict losses. The static pressure distribution can be obtained without including tangential variations, but the prediction of losses requires to solve the complete 3D flow.

[2]Note that this rotor is simulated without stator and thus it is slightly off-design

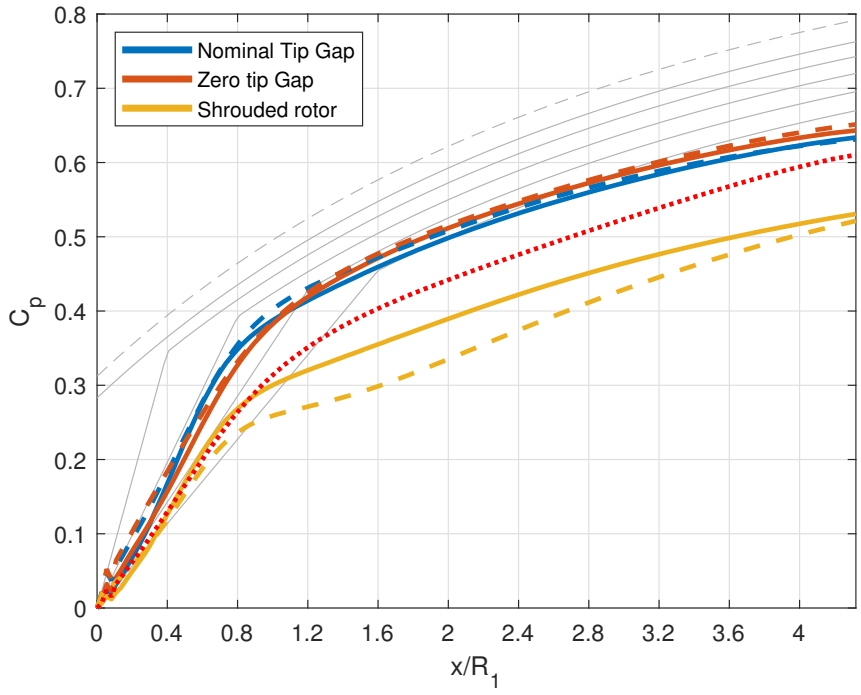

Figure 4.4: Static pressure recovery (C_p) for different tip gap configurations and rotor-diffuser interfaces (Solid line: Frozen Rotor; dashed line: Mixing Plane; red dotted line: uniform inlet). The thin gray lines represent ideal references, see text.

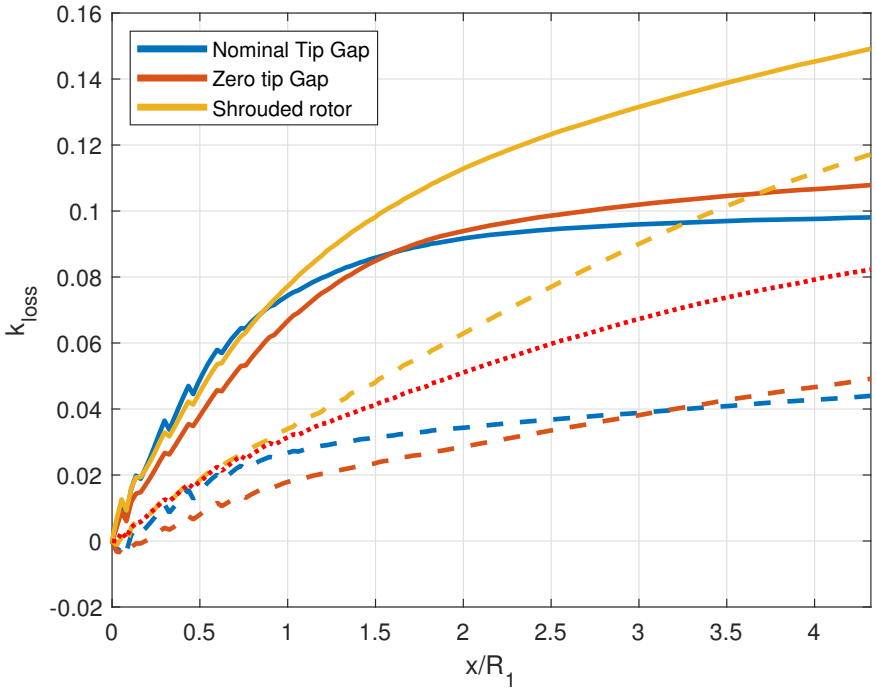

Figure 4.5: Total pressure loss coefficient (k_{loss}) for different tip gap configurations and rotor-diffuser interfaces (Solid line: Frozen Rotor; dashed line: Mixing Plane; red dotted line: uniform inlet).

4.1.3. Effects on mass flow

The computed massflow for the *nominal rotor* and *frozen rotor interface* is $0.342\ kg/s$, 4% more than the design objective[2] [47]. Table 4.1 shows the percentage deviation in mass-flow for the rest of simulations. The tip gap reduces mass-flow due to blockage effects, but the interface with the diffuser is not influential.

Table 4.1: Percentage difference in mass-flow for different T-100 rotor configurations and rotor-diffuser interface. $\dot{m}$ for frozen rotor and nominal configuration: $0.3416\ kg/s$.

	Nominal Rotor	**Zero Tip Gap**	**Shrouded Rotor**
Frozen Rotor	0	+1.6%	+1.49%
Mixing plane	+0.06%	+1.7%	+1.49%

4.1.4. Research Question 2

Research Question 2

Which is the simplest set-up able to capture realistic diffuser flow-fields and integral performance?

Along this section it has been discovered that in unstalled diffusers the static pressure trend (C_p) can be predicted with quasi-2D flows (only solving the flow in $r-x$). However, the prediction of diffuser losses, K_{loss}, requires the computation of 3D flows. This is because most of the losses are due to mixing, and these tridimensional structures dominate the mixing processes.

This implies that in the rest of the project frozen rotor interfaces will be used. This has important implications when developing low-order models for diffusers. If the losses are to be predicted in a 2D method, 3D effects must be included through some correction coefficient. Note that a 1D model will need to include the hub recirculating region as an input parameter. These results also show that simulations of isolated diffusers (both numerically and experimentally) are not fully representative of the installed operating conditions.

4.2. Tip Gap parametric study

The different tip gap configurations tested are shown in Table 3.6. Every result in this section corresponds to mass averaged values from CFD computations (Section 3.4). To avoid inconsistencies, the averaged properties are P, P_t and T_t. With these, $\dot{m}$, and geometrical parameters the rest can be computed[3]. Along this section parameters related to the turbine will be labeled ^{T}, whereass parameters refered to the whole assembly turbine+diffuser will be labeled ^{Sys}. In this section the computational domain always includes the stator, the rotor, and the diffuser.

4.2.1. Effects of tip gap on power generation and stage efficiency

Given that the boundary conditions are always the same, the best performance metric is flange to flange total to static efficiency, η_{ts}^{Sys}:

$$\eta_{ts}^{Sys} = \frac{w_{real}}{\hat{C}_p T_{4t}\left(1-(\beta_{ts}^{Sys})^{-\frac{\gamma-1}{\gamma}}\right)} = k w_{real} \rightarrow \frac{\eta_{ts}-\eta_{ts}^{ref}}{\eta_{ts}^{ref}} = \frac{w_{real}-w_{real}^{ref}}{w_{real}} \tag{4.1}$$

where the reference configuration is taken as the shrouded rotor. Note that the percentage increment in η_{ts}^{Sys} is exactly the same as the one in w_{real}. Figure 4.6 shows the difference in total to static efficiency for different tip gaps. Every model has the same diffuser and rotor geometry, the only change being in the shroud region. The red dot is the nominal T-100 tip gap configuration, and the red curve is the isoline with equal efficiency to the nominal rotor.

The plots show that configurations with bigger gaps always extract less work from the flow. However, for a given average tip gap size, configurations with *streamwise increasing tip gaps* will yield better performance. The figure on the right shows the same data plotted in terms of $\epsilon/\overline{h}$. This shows that a dimensional change in the leading edge gap (ϵ_{LE}) is more influential to performance than the same change in the trailing edge. Turbine performance, when coupled with a diffuser, is more sensitive to leading edge (axial) gaps.

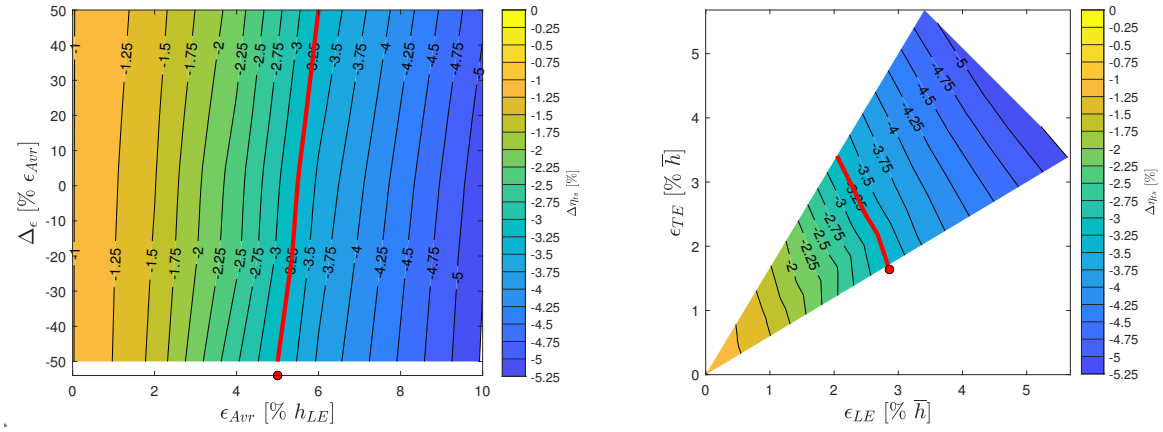

Figure 4.6: Change in system total to static efficiency, η_{ts}^{Sys}, with respect to the shrouded rotor for different tip gap configurations. The red curve is the isoline of efficiency equal to the nominal rotor, and the red dot represents this nominal configuration.

In order to isolate the effect of the diffuser on performance, the efficiency of the turbine must be shown explicitly. The work extracted is:

$$\tilde{w} = \frac{w_{real}}{\hat{C}_p T_{4t}} = \eta_{tt}^{T}\left(1+(\beta_{tt}^{T})^{-\frac{\gamma-1}{\gamma}}\right) \tag{4.2}$$

[3]The Mach number can be obtained from $\left(\frac{P_t}{P}\right)^{\frac{\gamma-1}{\gamma}} = 1+\frac{\gamma-1}{\gamma}M^2$, static temperature with $\frac{T_t}{T} = \left(\frac{P_t}{P}\right)^{\frac{\gamma-1}{\gamma}}$, density from the equation of state $\rho = \frac{P}{R_g T}$, and bulk velocity from $u = \frac{\dot{m}}{\rho A}$. Note that this formulation does not allow the recovery of swirl. Swirl and vorticity are contained as *non-uniform kinetic energy*, Section 2.1.

Comparing this to the expression for system total to static efficiency it is obtained:

$$\eta_{ts}^{Sys} = \eta_{tt}^{T} \frac{1-(\beta_{tt}^{T})^{-\frac{\gamma-1}{\gamma}}}{1-(\beta_{ts}^{Sys})^{-\frac{\gamma-1}{\gamma}}} \tag{4.3}$$

The fraction multiplying η_{tt}^{T} represents the effect of the diffuser and will be called $D(\beta_{tt}^{T})$. Then, the percentage gain of η_{ts} is:

$$\frac{\Delta\eta_{ts}^{Sys}}{\eta_{ts,0}^{Sys}} = \frac{(\eta_{tt,0}^{T}+\Delta\eta_{tt}^{T})(D_0+\Delta D)-\eta_{tt,0}^{T}D_0}{\eta_{tt,0}^{T}D_0}$$

$$\frac{\Delta\eta_{ts}^{Sys}}{\eta_{ts,0}^{Sys}} = \frac{\Delta\eta_{tt}^{T}}{\eta_{tt,0}^{T}} + \frac{\Delta D}{D_0} + \frac{\Delta\eta_{tt}^{T}\Delta D}{\eta_{tt,0}^{T}D_0} \tag{4.4}$$

Recognising that the changes in η_{tt}^{T} and D are very small with respect to their original values, the third term can be disregarded and the changes in system total to static efficiency can be seen as due to two additive effects: changes in turbine efficiency η_{tt}^{T} and changes in β_{tt}^{T}. Section 2.4 shows how C_p can affect β_{tt}^{T}.

Figure 4.7 shows this study. The plots on the left represent the changes on $D = \frac{1-(\beta_{tt}^{T})^{-\frac{\gamma-1}{\gamma}}}{1-(\beta_{ts}^{Sys})^{-\frac{\gamma-1}{\gamma}}}$ and the ones on the right the change in turbine losses. As expected, rotor losses grow with average tip gap.

The plots on the right of Figure 4.7 show work extraction enhancement due to tip gap-diffuser interaction. Note that the numerical value is the result of a comparison with the shrouded rotor results. However, the *gradient* of the plot is the most interesting result. This informs about the effect of increasing or decreasing the tip gap size. The maximum enhancement is for a non-zero gap configuration around $\epsilon_{LE} = 0.095\ mm,\ \epsilon_{TE} = 0.16\ mm$ (in local span percentages, $\epsilon_{LE} = 1.5$%, $\epsilon_{TE} = 0.7$%). The causes of this will be studied in Section 4.3. Note, in the lower left plot, that for the smallest gaps, turbine isentropic work extraction can be improved by increasing trailing edge gap (radial) at constant axial gap. This same plot shows that the work enhancement due to turbine tip gap -diffuser interaction depends almost exclusively on leading edge gap size, ϵ_{LE}.

Finally, changes in losses are five times larger than those in work enhancement. This is aligned with Farokhi's results [2], as the turbine can not extract more work by increasing tip gaps, even with a diffuser.

The most relevant conclusion of this section is the fact that *streamwise increasing gaps* (in absolute size) perform better both in terms of rotor losses and C_p enhancement. This is not what was traditionally thought[33], see Jones' design in the plots. In addition, the existence of an optimal tip gap size implies that there is a region where increasing tip gaps is also detrimental to diffuser performance.

4.2.2. Effects of tip gap on diffuser integral performance

C_p and M_5 changes

The C_p obtained with mass averaged pressures in each tip gap configuration is shown in Figure 4.8. When comparing these plots with *work enhancement* (left column in Figure 4.7), it is possible to see how the maximum in both plots is roughly located in the same position: it is this high C_p what improves β_{tt}^{T}. However, for bigger average tip gaps, C_p is less sensitive to the gap size itself and mostly depends on the *streamwise gap distribution*. This behaviour is not present in the work enhancement term.

In order to explain these differences it is necessary to include the Mach number at the outlet of the turbine, Figure 4.9. These plots show that M_5 increases up to 17% with varying average tip gaps, ϵ_{Avr}. Interestingly, the distribution of tip gap does not play a role in the change of Mach number, as showcased by the vertical isolines. Section 2.4 showed that for a given C_p and boundary conditions, higher M_5 reduces β_{tt}^{T}: This matches the behaviour of the work enhancement term for big gaps.

In this context M_5 represents a mass averaged kinetic energy. Higher M_5 implies more kinetic energy, and, as Section 2.1 showed, non-uniform velocity profiles contain more energy. M_5 grows with ϵ_{Avr} because the flow becomes less uniform.

This discussion shows that the effective result is a combination of C_p and M_5 changes, and these can not be studied in isolation. Furthermore, this changes can only be captured by including the turbine

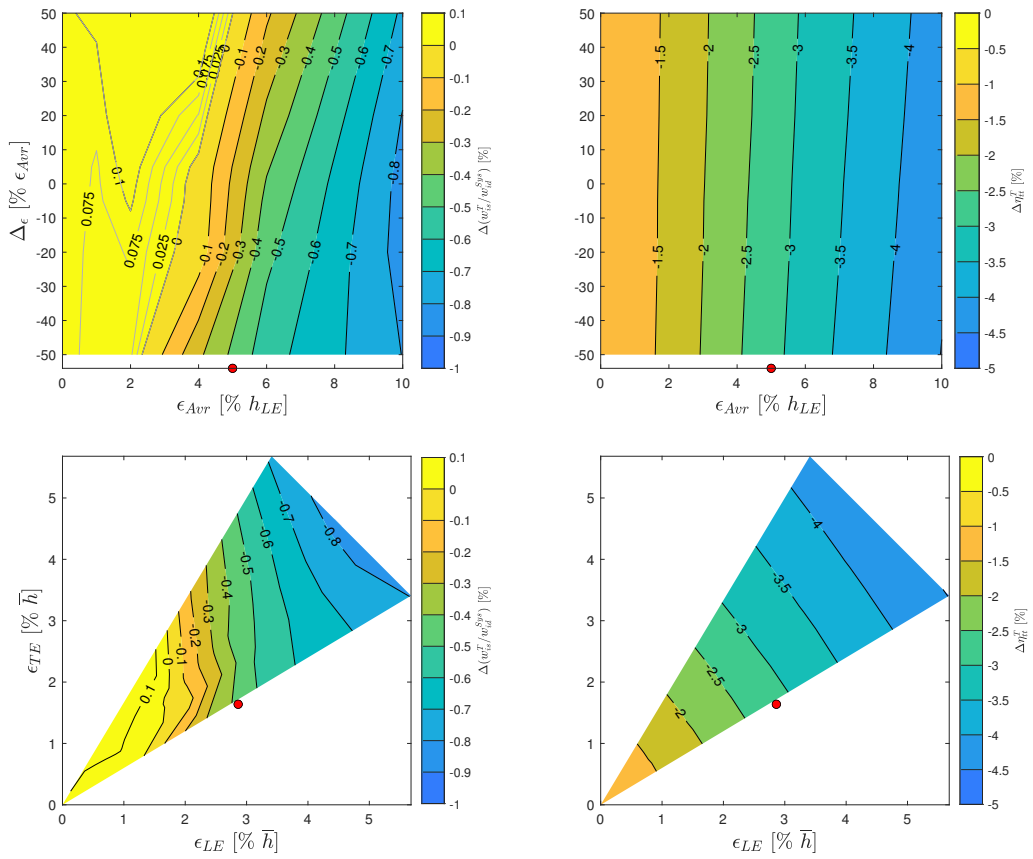

Figure 4.7: Change in turbine isentropic work (left) and turbine total to total efficiency, η_{tt}^T (right) due to different tip gap configurations. Shrouded rotor is taken as a reference. The the red dot represents the nominal configuration.

and the diffuser in the same simulation. C_p has a maximum and a minimum for finite values of ϵ_{Avr}, and *streamwise increasing gaps* always yield higher C_p. For gap configurations such that $\epsilon_{LE} < 2.5\%$ of the mean blade span, C_p mainly depends on ϵ_{LE}, and greater ϵ_{TE} can even increase C_p (Figure 4.8 right). For ϵ_{Avr} bigger than this the changes in C_p are much smaller.

Origin of C_p variations

In order to explain the variations of C_p with different tip gap configurations it is useful to recall the following relation:

$$C_p + k_{loss} + \xi_{bulk} + \xi_{NU} = 1$$

where the quantities ξ_{bulk} and ξ_{NU} are introduced in Section 2.1. Evaluating this expression at the inlet and at the outlet of the diffuser it is obtained:

$$C_p = -\Delta\xi_{bulk} - (k_{loss} + \Delta\xi_{NU}) \tag{4.5}$$

Where the terms in the right hand side represent diffusion, losses, and the effect of non-uniformities. Note that $\Delta\xi_{bulk}$ is negative if the flow diffuses and $\Delta\xi_{NU}$ is negative if the flow becomes more uniform, so these two phenomena *increase* C_p. The right hand side has been grouped in such a way that it is clear that C_p mainly comes from diffusion, but there is a second addend related to mixing processes. It is not trivial to know *a priori* if the term in brackets will increase or decrease C_p.

The results from the test case are shown in Figure 4.10. The plot on the left shows the *diffusion* effect, $-\Delta\xi_{bulk}$ and the plot on the right shows the *mixing* effects, $-(k_{loss} + \Delta\xi_{NU})$. The addition of these two values exactly matches C_p, Figure 4.8. Note that the difference between maximum and minimum values on both plots are similar. The diffusion effect shows a strong dependency with ϵ_{Avr} and almost none with

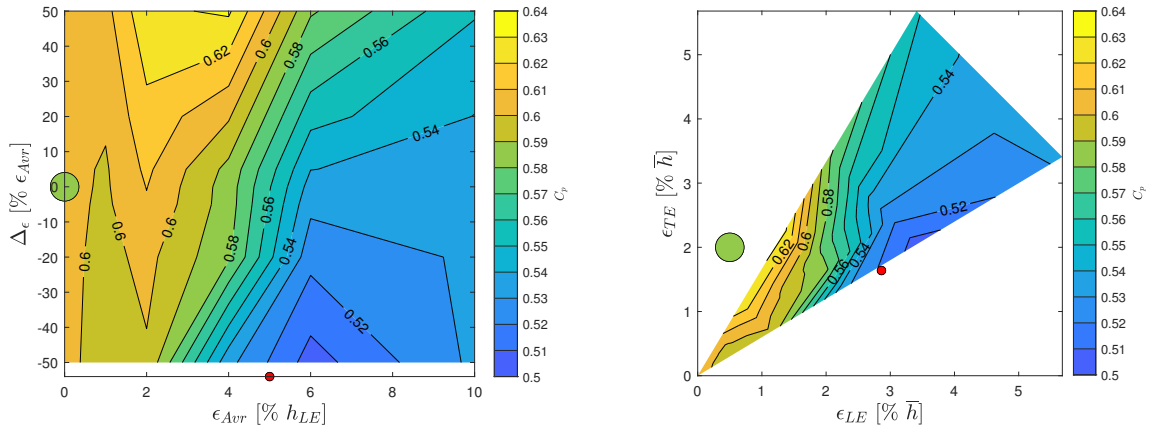

Figure 4.8: C_p computed from mass averaged values. The red dot represents this nominal configuration, and the colored dot is the value of the shrouded rotor.

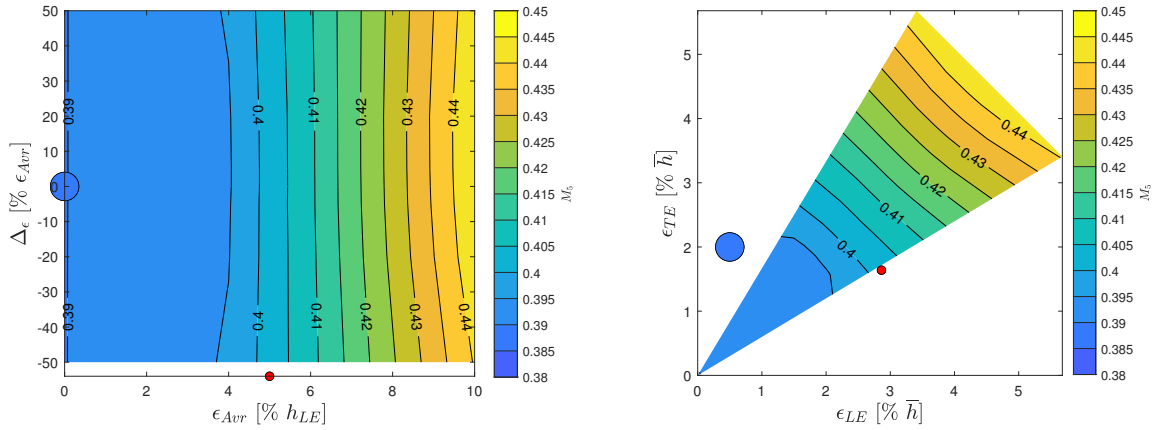

Figure 4.9: M_5 computed from mass averaged P_{5t} and P_5 at turbine outlet. The red dot represents this nominal configuration, and the colored dot is the value of the shrouded rotor.

the *streamsise tip gap distribution*. This behaviour is very similar to that of M_5, and it is actually due to the same physical phenomena. M_5 is a measure of total kinetic energy, and $-\Delta\xi_{bulk}$ is the diffusion of the *bulk* kinetic energy. The bigger the energy content of the non-uniform flow is, the smaller the effect of ξ_{bulk} becomes. This is because ξ is non-dimensional with the inlet dynamic pressure, and this increases with non-unifrom flow.

The dependencies of the mixing process are more complex. For small ϵ_{Avr} this term mainly depends on *streamwise gap distribution*, and not on ϵ_{Avr}. For $\epsilon_{Avr} > 3\%\ \overline{h}$, the driving parameter becomes gap size and the distribution is less important. Note that it is this dependency for small ϵ_{Avr} what makes C_p for *streamwise increasing tip gaps* greater. Lastly, for very big gaps $-(k_{loss} + \Delta\xi_{NU})$ changes sign, and the pressure recovery due to ξ_{NU} overcomes the losses k_{loss}: the dissipation of flow structures can produce a net increase in static pressure.

To further clarify the previous statement, $\Delta\xi_{NU}$ and k_{loss} are compared in Figure 4.11. The losses in the diffuser mainly depend on ϵ_{Avr}, and they increase with tip gap size. This suggest that the losses in the diffuser are driven by mixing processes. On the other hand, all the complexity described previously comes from the term $\Delta\xi_{NU}$. Note that this is negative in most of the domain,meaning that non-uniformities contribute to diffuser pressure recovery. It is clear that for $\epsilon_{Avr} \approx 3\%\ \overline{h}$ there is an important change in flowfield configuration affecting the dissipation of turbine vortical structures (Section 4.3). For small tip gaps the flow structures are sensitive to tip gap distribution, whereas this is not true after some critical size.

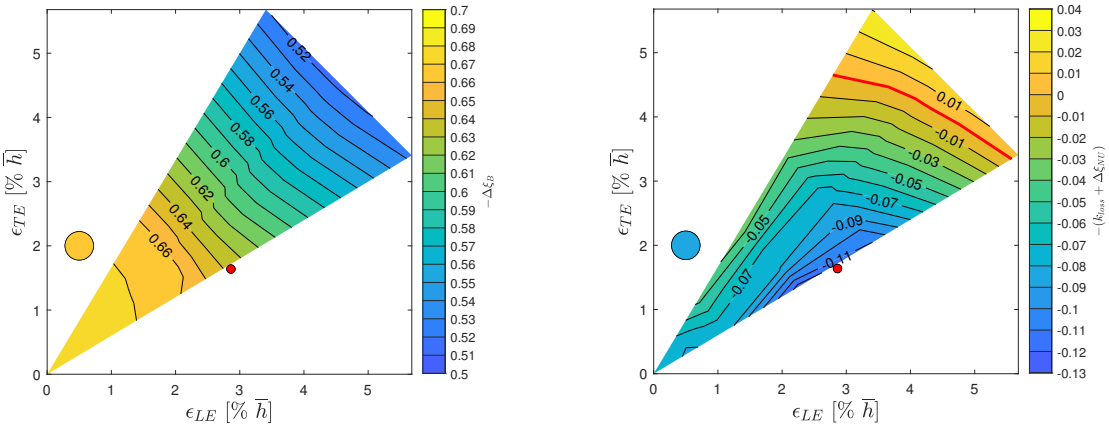

a) Contour of $-\Delta\xi_{bulk}$ **b)** Contour of $-(k_{loss}+\Delta\xi_{NU})$

Figure 4.10: Value of the terms in $C_p = -\Delta\xi_{bulk} - (k_{loss} + \Delta\xi_{NU})$ for different tip gap configurations.

Figure 4.12 shows $\overline{k_{loss}} - \overline{k_{loss}}^{Mixed\ Out}$ in order to confirm mixing as the main source of k_{loss}. This difference is representative of the progress of the mixing through the diffuser, Section 3.4. It is possible to see how mixing losses are the biggest part of k_{loss} and they are roughly proportional to ϵ_{Avr}. The other kind of losses in the diffuser are smaller and depend on tip gap distribution. The change in behaviour for $\epsilon_{Avr} \approx 3$ is only visible in $\Delta\xi_{NU}$, what implies that it has something to do with the *effectiveness* of the flow structures and not with any *efficiency* or dissipation process.

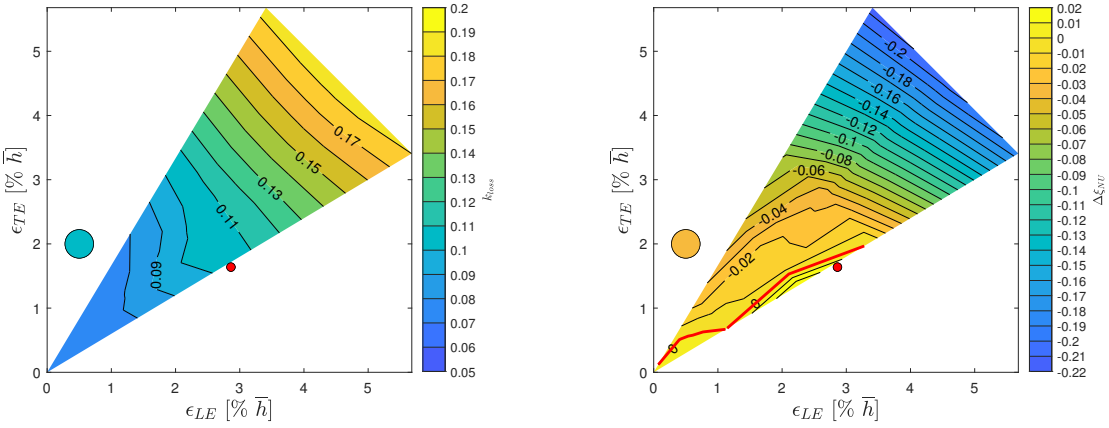

a) Contour of k_{loss} **b)** Contour of $\Delta\xi_{NU}$

Figure 4.11: Comparison of losses and pressure recovery due to non-uniformities for different tip gap configurations.

Summary

The previous discussion can be summarised in the following points:

1. Turbine work extraction always decreases with increasing tip gaps. For a given ϵ_{Avr} this penalty is bigger for *streamwise decreasing* tip gaps.
2. This loss in performance is mainly due to losses in the rotor, which are 5 times more important that any change induced by the diffuser.
3. The work enhancement due to the diffuser depends both on M_5 and C_p. M_5 always increases with ϵ_{Avr}, what is *detrimental* to β_{tt}^T enhancement. C_p variations with tip gap configuration are more complex, and there is a maximum and a minimum C_p for finite values of ϵ_{Avr}.Pressure recovery is always bigger for *streamwise increasing* tip gaps.

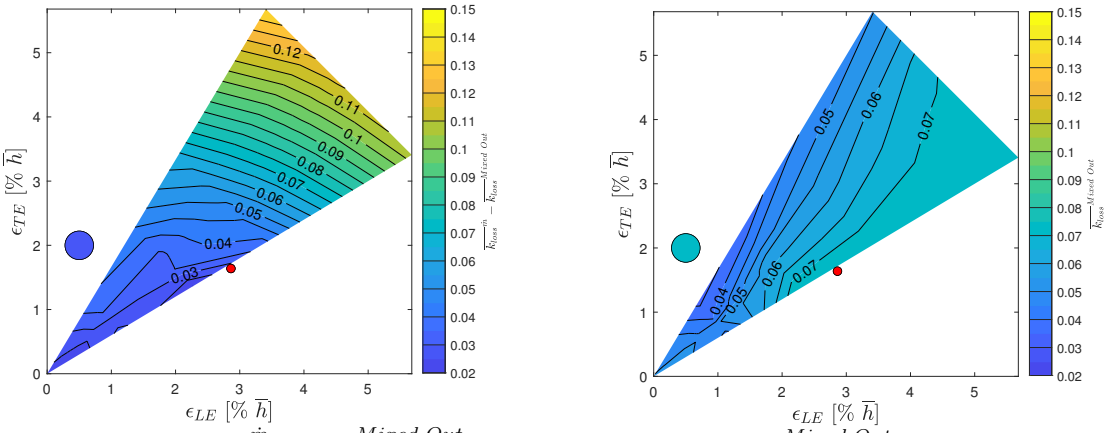

a) Contour of $\overline{k_{loss}}^{\dot{m}} - \overline{k_{loss}}^{Mixed\ Out}$, representative of mixing losses.

b) Contour of $\overline{k_{loss}}^{Mixed\ Out}$, representative of the rest of losses

Figure 4.12: Decomposition of k_{loss} in mixing losses and another losses

4. Depending on tip gap configuration, diffuser work enhancement can *alleviate* or *increase* the cost on performance of the tip gaps.
5. C_p origin can be found in *diffusion* ($\Delta\xi_{bulk}$) or *non-uniform flows* ($\Delta\xi_{NU} + k_{loss}$). *Diffusion* mainly depends on ϵ_{Avr} and decreases with it. Non-uniform flow effects present different behaviours:
   - for $\epsilon_{Avr} < \epsilon^*$ the main parameter is Δ_ϵ.
   - for $\epsilon_{Avr} > \epsilon^*$ the tip gap distribution is less important, and the gap size is the main parameter.
6. Diffuser losses (k_{loss}) are mainly due to mixing of non-uniform flow, and this increases with ϵ_{Avr}.
7. Dissipation of non-uniform structures ($\Delta\xi_{NU}$) recovers static pressure in most of the configurations, and for big gaps can overcome losses. It is this term what introduces the existence of ϵ^* and the different behaviours for small or big gaps.
8. All dependencies of work enhancement with tip gap can be traced back to the way non-uniform flows dissipate in the diffuser. It is a mixing process parallel to diffusion. The reduction in the *diffusion* term ($\Delta\xi_{bulk}$) is partially due to the non-dimensionalization, and it implies that the kinetic energy of non-uniform flows can not be recovered by expanding the flow.

4.2.3. Distribution of performance coefficients along the diffuser

In the quest of obtaining short and high performance diffuser, a configuration gaining C_p very rapidly might be more interesting that a full-length efficient diffuser. Figure 4.13 shows the required length to achieve different C_p with different tip gap configurations. It can be seen that those diffuser that have been identified as the best performing ones are better at any given axial station. The highest pressure recovery can be obtained only with the tip gap configuration that yields best diffuser performance. On the other hand, if the objective is a smaller C_p, as for instance 0.5, the plot shows that between the nominal design and the best tip gap configuration, the diffuser length varies by a factor of 2. This improvement would be achieved by reducing ϵ_{LE} to $^1/_3$ of its original value. Such an improvement might justify expensive measures to tune the tip gap distribution in order to offset the installation cost of a bigger machine.

The evolution of C_p for different tip gap configurations is shown in Figure 4.14. The plot on the left shows the mass averaged evolution and a reference ideal $C_{p,i}$ in light gray, and the plot on the right shows the difference between computed and ideal values. This ideal reference assumes that an incompressible flow expands without losses and fully attached to the spinner[4]. The difference between *small* and *big* gaps is visible as two curve clusters. Gaps bigger than $\epsilon_{Avr} > 2.5\%\ \overline{h}$ do not recover as much pressure in the first R_1 length and they evolve almost parallel to the smaller gaps after this. Lastly, note the evolution of

[4]Note how it is possible to see the separation point and the axial station where the separation bubble closes as inflexion points in the second plot.

the purple lines ($\epsilon_{Avr} = 1.82\%\ \overline{h}$): for *streamwise increasing* tip gaps it is the best performing one, but for *streamwise decreasing* gaps it behaves as the *big* tip gap evolution. The critical value of gap size and differences in flow structures must be in this region.

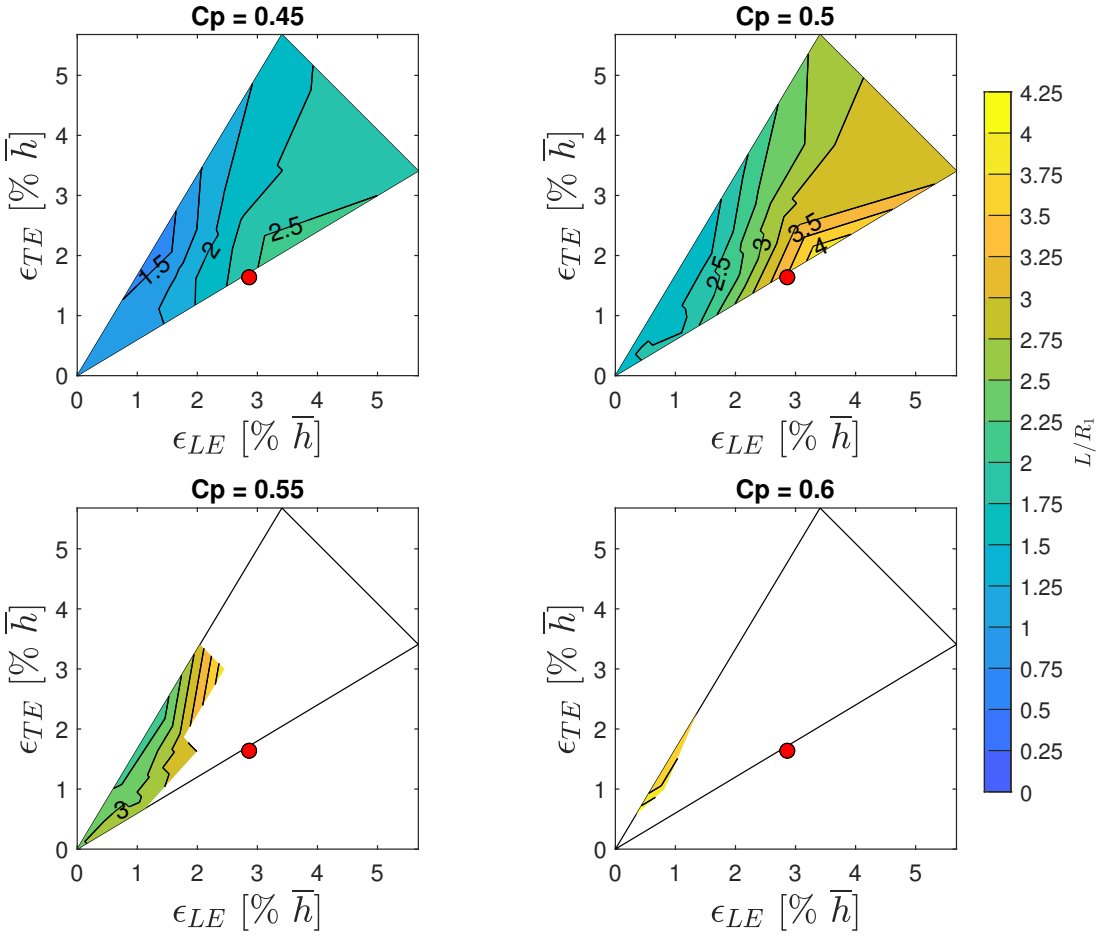

Figure 4.13: Non-dimensional diffuser length, L/R_1, required to achieve a given C_p for different tip gap configurations.

4.2.4. Influence of λ and R on diffuser performance

The previous results have shown that there are two different behaviours on turbine-diffuser interaction depending on the size of the tip gaps. Furthermore, the origin of these differences has been traced back to the way flow structures dissipate in the diffuser. However, the terms *big* and *small* have been used loosely. In order to find a rigorous description, it is necessary to apply the theory described by Dambach et al. (2001 [33], Section 2.3 in this text) and recover tip gap characteristic parameters:

$$R(s) = \frac{\Delta P}{\frac{1}{2}\rho U(s)^2 \cos^2(\gamma(s))} \tag{4.6}$$

$$\lambda(s) = \frac{\varepsilon(s)}{t(s)} = \frac{\epsilon_{Avr}}{t_{max}} \frac{1 + \Delta_\epsilon(s^{-1}/_2)}{t'} \tag{4.7}$$

where s is a streamwise coordinate along the rotor, $U(s) = \Omega \cdot r(s)$ is the peripheral speed of the blade tip at a given streamwise position, γ is the metal blade angle with the meridional direction, t_{max} is the maximum thickness of the blade at the tip, and $t' = t/t_{max}$ is the non-dimensional blade tip thickness distribution. Note that λ has been separated into *size* and *design*.

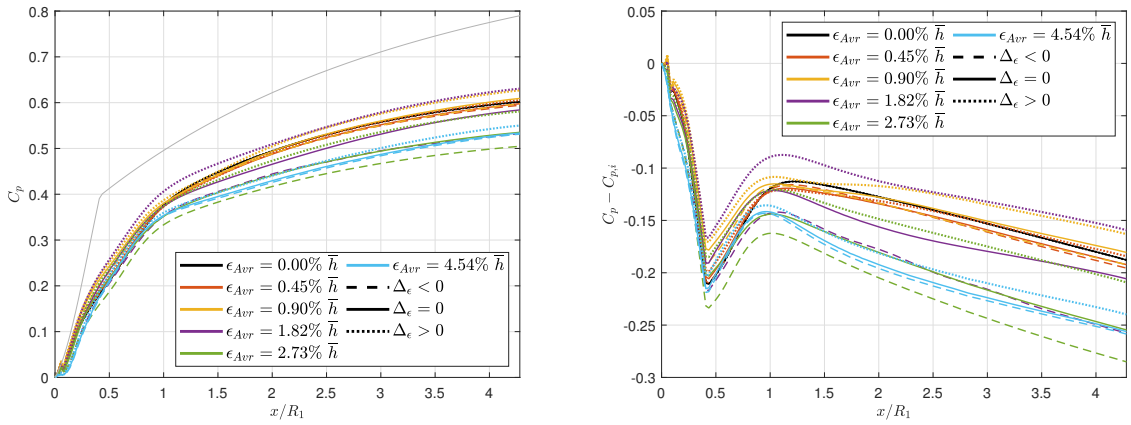

a) $C_p\left({}^{x}/_{R_1}\right)$ **b)** $C_p - C_{p,i}$

Figure 4.14: Evolution of pressure coefficient C_p along the diffuser for different tip gap configurations.

The pressure to scraping ratio R is shown in Figure 4.15. As a reference, this figure also includes this parameter evaluated without tip gaps: the black solid line is the shrouded rotor evaluated at 99% span and the black dotted line is the zero tip gap case, also evaluated at 99% span. The cases with non-zero tip gaps have been evaluated over a circumferential line located at the middle of the gap. As noted by Dambach et Al. [33], the inducer region is dominated by scraping effects ($R < 1$). The rest of the rotor is dominated by pressure blade loading. The general trend is that bigger gaps unload the tip of the blade *more* and *further upstream* than smaller ones.

Figure 4.16 shows the distribution of the λ coefficient along different rotors. These curves are very dependent on the blade tip thickness distribution, as shown by Equation 4.7. Furthermore, both plots include different diamond markings showing the different flow regimen of the tip gap cavity (Figure 2.5). Blue diamonds show the location of the first *isentropic jet* (Section 4.3; Figure 4.27, 4.28 and 4.29); the green diamond show the last location where this jet was found, and blue diamonds show the location where the *isentropic jet* is strong enough as to push the scraping flow and leave the gap tangentially (Section 4.3; Figure 4.24, 4.25 and 4.26). This data shows that it might be impossible to define a single universal λ^* to predict the existence of the isentropic jet. The interaction between scraping, blade loading, and tip gap cavity shape is intense, and it was not possible to find any correlation between them. Furthermore, the vortex dynamics described in the next paragraphs make the author recommend the inclusion of more geometrical information about the meridional gas path if this task is going to be attempted. The general trend suggest that lower R parameters (more scraping to loading ratio) require higher λ values to yield the same phenomenology, but also upstream influence seems relevant (Section 4.3). For the case $\epsilon_{Avr} = 1.82\%\ \overline{h}$ it is possible to find regions where $\lambda > \lambda^* \approx 0.2$ [33] without isentropic tip gap jets. These regions are located where scraping is maximum. Note that the scraping flow partially blocks the tip gap, so the *effective* tip gap height is reduced. The effect might be studied in terms of $\lambda_{eff} = \frac{\epsilon - \epsilon_{scraping}}{t}$. However, this detailed characterization of tip gap cavity flow structures is out of the scope of the project.

4.2.5. Research Question 3

Research Question 3

What is the effect of tip gap size and distribution on the integral performance of the diffuser?

It has been found that different tip gap sizes and distributions affect the performance of the diffuser, changing C_p up to 20% for a given geometry, or diffuser length up to 100% for a given C_p. There is an optimal tip gap configuration. Bigger tip gaps are detrimental both to diffuser and rotor performance. Furthermore, the origin of this interaction has been traced back to the pressure recovery due to the dissipation of non-uniform flow structures. Diffuser losses depend on ϵ_{Avr}, and they are mainly driven by mixing. On the other hand, pressure recovery due to non-uniform flow depends both on gap size

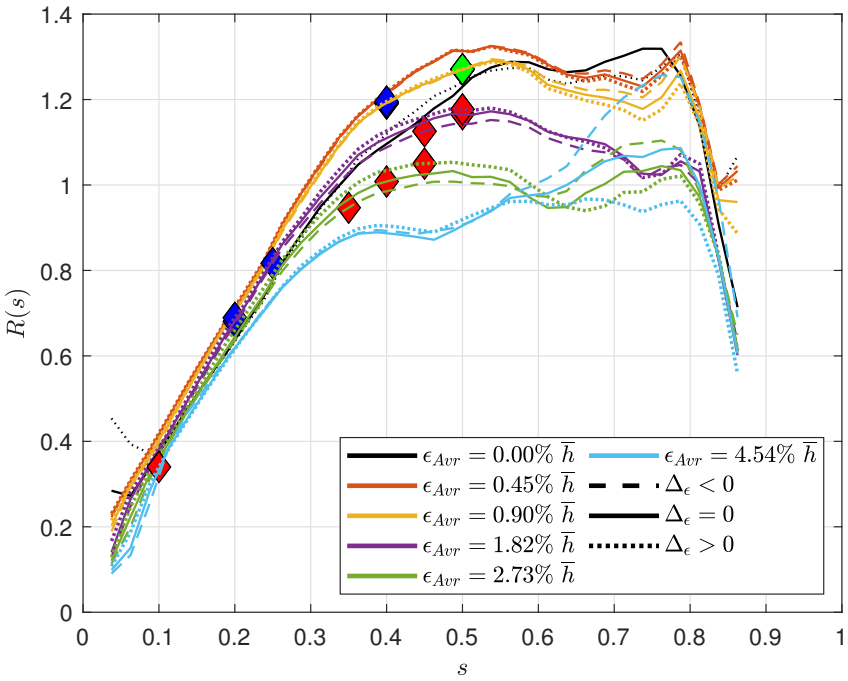

Figure 4.15: Parameter $R = \frac{\Delta P}{\frac{1}{2}\rho U(s)^2 \cos^2(\gamma(s))}$ described in [33] and Section 2.2.3. Blue diamonds are the first streamwise position with an isentropic jet, green is the last position with this jet, and red is the first location where the tip gap flow pushes the scraping vortex away from the blade. Black solid line is 99% span of the shrouded rotor and black dotted line is 99% span of the zero tip gap case.

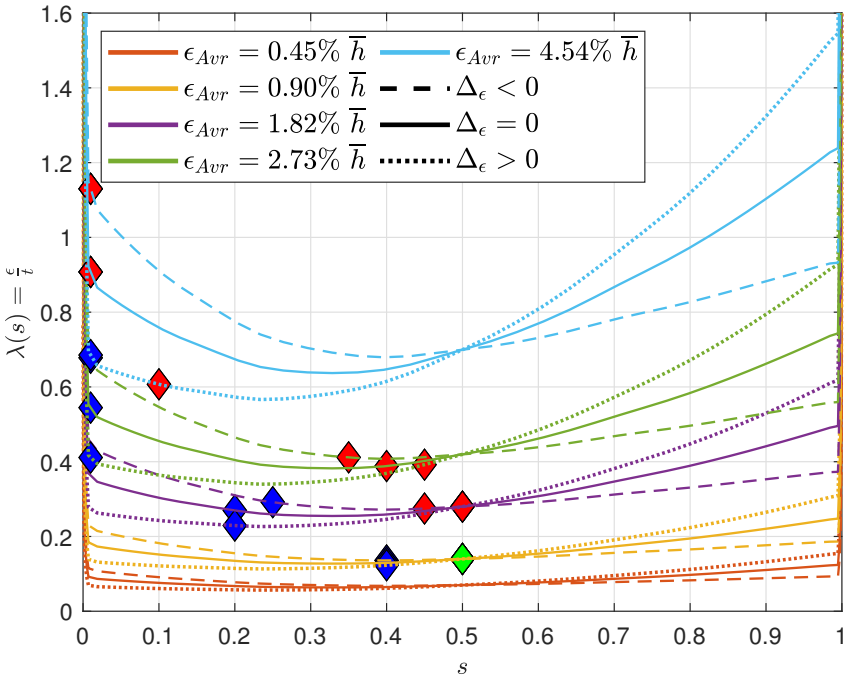

Figure 4.16: Parameter $\lambda = \frac{\epsilon}{t}$ described in [33] and Section 2.2.3. Blue diamonds are the first streamwise position with an isentropic jet, green is the last position with this jet, and red is the first location where the tip gap flow pushes the scraping vortex away from the blade.

and distribution. Small gaps perform better, and *streamwise increasing* tip gaps yield the best pressure recovery. If a critical gap size is surpassed, the dependency on distribution is mostly lost and performance drops with ϵ_{Avr}.

It has been attempted to identify the conditions where this change in behaviour occurs by means of tip gap characteristic parameters, as λ and R. No general quantitative trend was found, but lower R parameter requires higher λ to yield the same diffuser integral behaviour. Furthermore, the data obtained shows that it is unlikely to find an universal λ^* value to characterise the tip gap cavity flow, as this also depends on scraping [33].

Finally, it has been also shown than an increment in tip gap size will always reduce power extraction. However, if the design team is given a choice between reducing axial or radial gap, diffuser interaction criteria says that they should reduce the axial (leading edge) one, even at the cost of small increases in the another one.

4.3. Detailed Study of RIT Rotor flow structure

In order to properly asses the flow structures in the rotor shroud region it is important to set down the basis and physical origin of them. Section 2.2.2 offers an introduction about what secondary flows are. A list of the different vorticity sources in a RIT is:

- **Convected Vorticity** from upstream domains, as for instance stator horse-shoe vortexes, Figure 4.17 left (*In this work these structures are dissipated by the mixing plane model*).
- **Secondary flows** generated by:
  - *Incoming boundary layers*, as for instance the HSV in the rotor leading edge, Figure 4.17 right (*The pressure side leg dissipates quickly, the suction side leg migrates to the middle of the hub and in most configurations emanates from the turbine. The effects of these are out of the scope of the project*).
  - *Boundary layers in the domain*, that when interacting with pressure and inertia forces generate classical boundary layer crossflows as the ones studied by Zangeneh (1988, [31]).
- **Shroud scraping**, which generates a shear layer that rolls into a coherent vortex against the suction side blade tip.
- **Tip gap flow**, which strongly interacts with scraping flow. The existence of a tip gap does not immediately imply a traditional tip gap vortex.
- **Wakes** originated by the merging of blade boundary layers (*Effect of the stator wake unknown due to mixing plane model, effect of rotor wakes very important for diffuser performance in shrouded rotors.*).
- **Boundary layer separation**. For off-design operating conditions the flow separates at the inlet of the rotor as a strong coherent vortex at blade mid-span. This vortex is not present in on-design conditions.
- **Potential flow effects**, as for instance spanwise blade loading. This can cast continuous vortex sheets to the diffuser (*This effect is out of the scope of the project*).

The most important sources of vorticity in the project are *boundary layer cross-flow*, *Shroud scraping* and *tip gap flows*. A convenient way of identifying coherent vortexes is through the Q-criterion (Dubief et Al. 2000 [49]). However, the complexity and tridimensionality of the flow makes it difficult to show structures in static pictures. For this reason, *nomaliced Helicity* contours in constant streamwise surfaces will be used. This quantity is:

$$H = \frac{\vec{v} \cdot \vec{\omega}}{|\vec{v}|} \tag{4.8}$$

It is the streamwise component of vorticity. Given that vortex cores behave as streamlines, this magnitude locate coherent vortexes as maximum and minimums, while ignoring the vorticity in 2D boundary layers. Furthermore, the sign of this quantity allows the identification of the direction of rotation of the flow, see Figure 4.17 left. Note that the outer region of cross-flow boundary layers also generate a streamwise vorticity component.

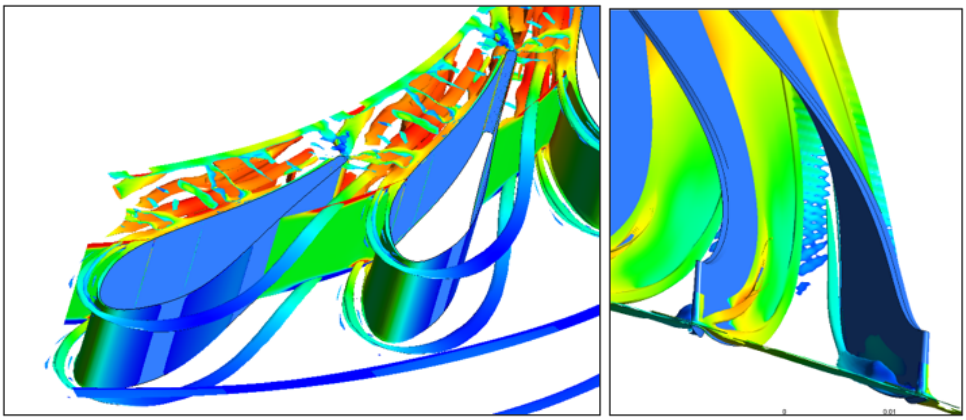

Figure 4.17: Vortical flow structures at the stator and at the hub region of the rotor inlet. Visualized as Q-criterion isolevels ($Q = 0.0005$) and colored by velocity. The left picture shows a $R = const$ plane colored by streamwise vorticity to show the direction of the HSV.

4.3.1. Cross-flow boundary layers

The first source of secondary flows to be studied is boundary layer cross-flow. As introduced in Section 2.2.2, the bulk flow establishes a mean pressure field and higher or lower momentum particles are affected differently. Low momentum particles are *more* affected by pressure gradients, and thus they migrate towards low pressure regions, whereas high momentum particles have more inertia and are deflected to high pressure regions.

In a RIT rotor channel the fluid particles are subjected to streamline curvature and inertia forces, and the balancing of them yields the *average* pressure field. The blade to blade channel curvature and coriolis forces both generate a tangential pressure gradient that contributes to blade loading, Figure 4.18. Note that Coriolis forces are always perpendicular to the flow velocity and they decrease as the flow progresses through the machine. Regarding the meridional plane, gas path curvature generates a pressure field which is maximum at the hub, while centrifugal forces always generate a pressure gradient component increasing radially out. In this case the pressure at the shroud is always lower than at the hub, Figure 4.19.

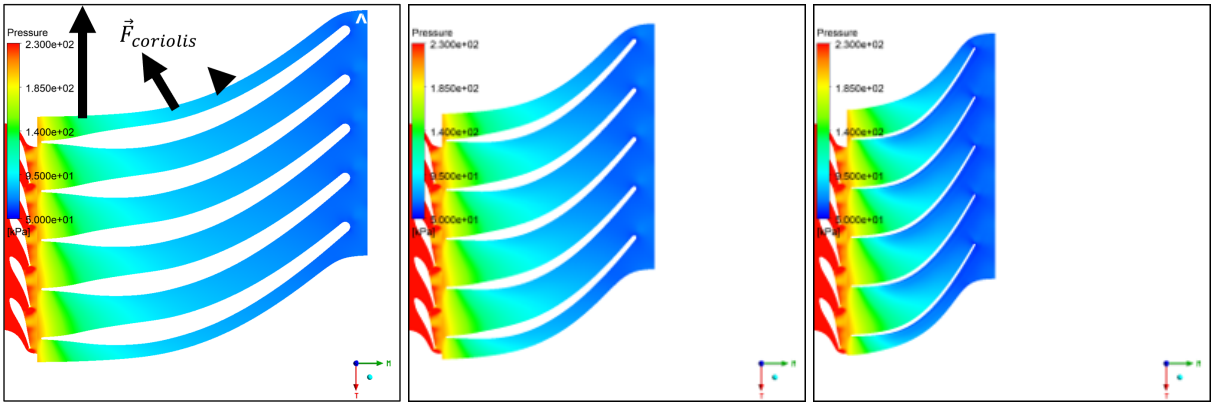

Figure 4.18: Pressure distribution is the blade to blade plane for the T-100 turbine. From left to right: hub, mid-span, and shroud.

This pressure distribution convects low momentum fluid (boundary layers) towards the shroud and suction side of the blade. This is shown as wall shear stress traces in Figure 4.20 for a shrouded rotor. Note that the only source of secondary flows in this case is the pressure field. The flow in hub and casing is migrating towards the suction side of the blades (convex surface). Regarding spanwise flows, it is very obvious at the inducer region of the blade, but the effect is greatly reduced by the exducer section.

This flow migrating from the hub, pressure side corner, towards the shroud, suction side corner generates

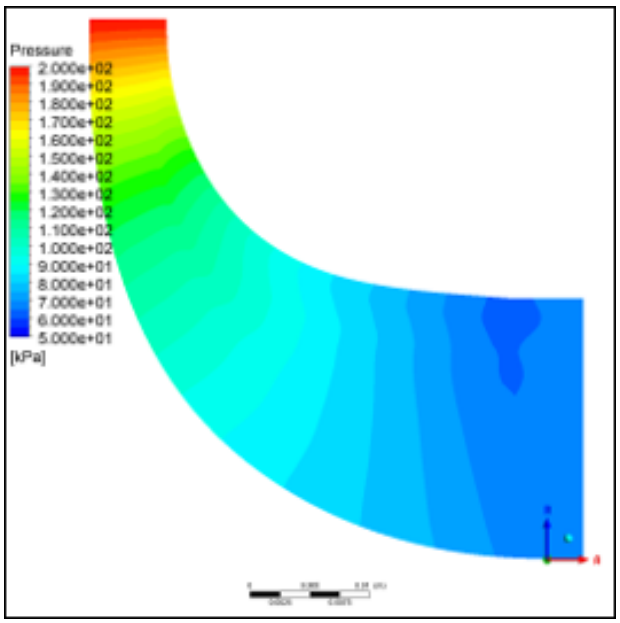

Figure 4.19: Pitch-wise averaged static pressure distribution for the T-100 rotor.

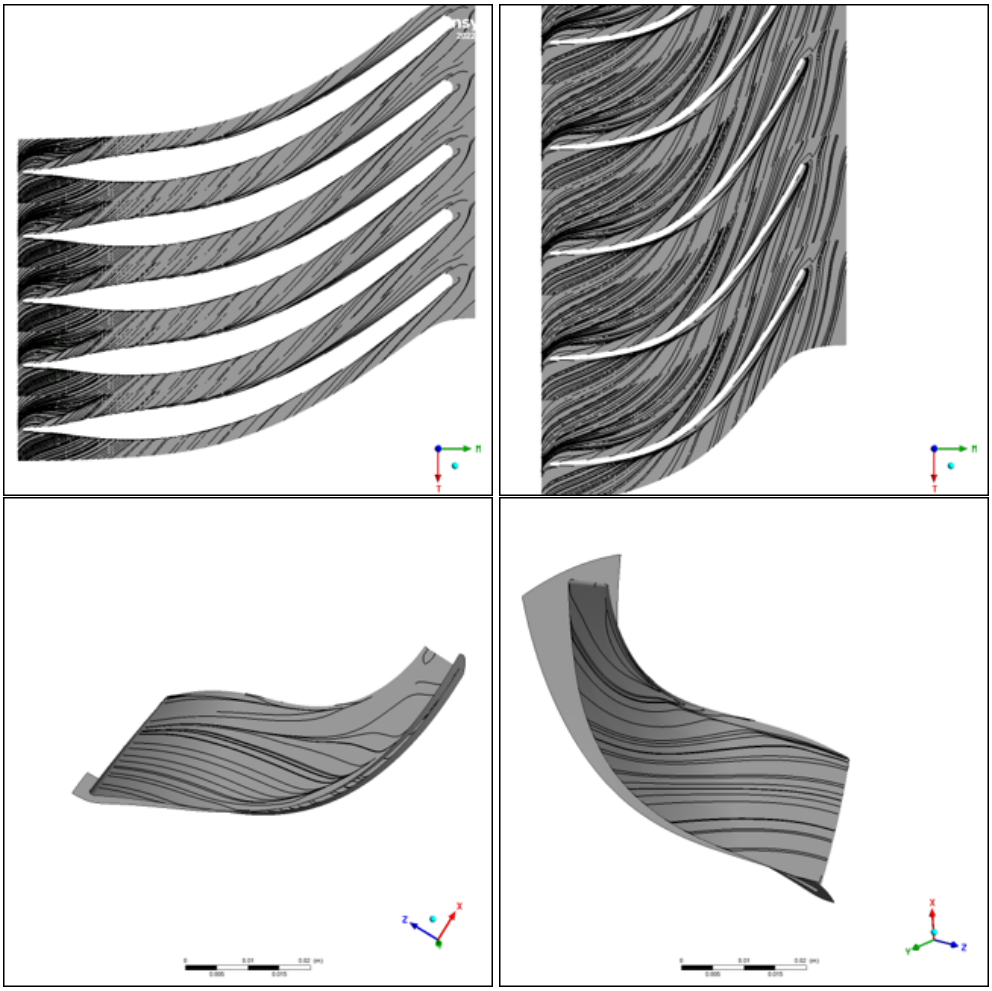

Figure 4.20: Wall shear stress traces for a T-100 shrouded rotor. Top, from left to right: Hub and Shroud; bottom, from left to right: pressure side and suction side.

the following structures in the secondary plane:

- A weak sink-like flow structure at the hub-pressure side corner.
- Corner vortexes in the shroud suction side and hub pressure side corners. This is visible in Figure 4.17 right as a Q-criterion isosurface *wedge*.
- A weak jet-like structure of very high entropy flow at the shroud suction side corner (Figure 4.27).

When more flow features are added, as scraping or tip gap leakage, these secondary flows continue there. The helicity field for the shrouded case can be seen in Figure 4.21 top left, and the entropy field in Figure 4.27 top left. This is the high entropy *wake* described in [31].

When scraping is added, a scraping vortex appears. This flow traverses down the suction side of the blade and pushes the secondary flow structures towards the hub. See Figure 4.21 top right: a weak scraping vortex is emanating from the turbine, and the secondary flows have rolled up into a streamwise vortex sitting bellow this scraping vortex. Regarding the entropy field (Figure 4.27 top right), there is a spot of higher losses. However, when compared with the shrouded case, this is displaced towards the middle of the channel, avoiding diffuser boundary layer separation. It is this scraping vortex located lower in the suction side what drags high energy flow into the suction side shroud corner and re-energises this region, Figure 4.27.

The next paragraphs describe the changes with respect to this baseline flowfield due to the addition of tip gaps. Some pictures has been already used, but a general introduction will ease comprehension. Figure 4.21, 4.22 and 4.23 show the helicity field in the rotor. Red is high positive helicity (vorticity *pointing* downstream) and blue is high negative helicity (vorticity *pointing* upstream). Figure 4.24, 4.25 and 4.26 show the streamlines emanating from the tip gap. The helicity field is maintained in a black and white color pallet, the darker regions being upstream vorticity and the lighter ones downstream vorticity. The color of the streamlines indicate the streamwise position where they emanate from, blue being the inducer and red the exducer. Figure 4.27, 4.28 and 4.29 show the the entropy field. Blue regions are low entropy and the red ones are high entropy regions. Figure 4.30, 4.31 and 4.32 show the relative kinetic energy field in the rotor with the same color criteria as the previous one. Finally, Figure 4.33, 4.34 and 4.35 show the Rothalpy field, again using the same coloring criteria. Every plot in a group has the same scale and the maximum and minimum values are indicated in the caption. Each group of figures starts with the shrouded and zero tip gap cases, and then each row shows $\epsilon_{Avr} = 2\%\ h_{LE}$, $\epsilon_{Avr} = 4\%\ h_{LE}$, $\epsilon_{Avr} = 6\%\ h_{LE}$ and $\epsilon_{Avr} = 10\%\ h_{LE}$ gaps, except in Figure 4.24 where $\epsilon_{Avr} = 1\%\ h_{LE}$ is shown instead of the zero tip gap cases. The smallest tip gap is omitted because it is indistinguishable from $\epsilon_{Avr} = 2\%\ h_{LE}$. The left column is always *streamwise decreasing gaps* ($\Delta_\epsilon = -50\%\epsilon_{Avr}$) and the right one *streamwise increasing gaps* ($\Delta_\epsilon = +50\%\epsilon_{Avr}$). The tip gap distributions omitted show smooth changes between these two. Finally, the second page in every plot family always contains the best performing diffuser ($\epsilon_{Avr} = 4\%\ h_{LE}$, $\Delta_\epsilon = +50\%\epsilon_{Avr}$) and the configuration where the change in integral behaviour happens ($\epsilon_{Avr} = 6\%\ h_{LE}$). All plots show three channels and 11 streamwise sections. the first one is upstream of the leading edge and the last one downstream of the trailing edge. Note that the last section only shows two channels. The wake located in the middle of this last section (use the contour of the periodic boundary as a reference) is the one created by the visible blade, and the flow structures over this line are the ones emanating from the channel that is shown. All pictures are a view from the exducer hub towards the inlet, the suction side of the blade is shown, and the rotor spins counterclockwise.

4.3.2. Streamwise vorticity field

Figure 4.21, 4.22 and 4.23 show the helicity distribution for different cases. Three different outflow configurations can be seen depending on ϵ_{Avr}:

1. For very small gaps, Figure 4.21, there are two counter-rotating weak vortical structures very close to the blade wake and separated one vortex diameter from the casing, label A. The *upstream* vortex (blue) is the scraping vortex, and the *downstream* one (red) is a combination of secondary flow and tip gap flow vortex. As mentioned before, the scraping vortex is over the *downstream* one and pushes it towards the hub.
2. For very big gaps, Figure 4.23, there is a very strong *dowstream* vortex that drags around the scraping vortex, label B. This scraping vortex is stronger than before, and both are located roughly at the same radial position almost blocking the totality of the shroud flow-path region. This flow structure is not sensitive to tip gap distribution.

3. For configurations in the mid region, Figure 4.22, it is possible to identify at least three vortical structures. The two corresponding to small tip gaps (A), and sitting in the space between these and the casing, and closer to the blade wake, a *downstream* vortex reminiscent of the one for big tip gaps (B). Note that for $\epsilon_{Avr} = 4\%\ h_{LE}$ and $\Delta_\epsilon = +50\%\epsilon_{Avr}$ (top right) the structure is more representative of very small gaps, and for $\Delta_\epsilon = -50\%\epsilon_{Avr}$ (top left) the pair of vortexes is weaker and the isolated tip gap vortex has grown: By changing tip gap distribution the flow structure transitions smoothly between modes. The same phenomena is present for the bigger $\epsilon_{Avr} = 6\%\ h_{LE}$, but the pair of vortexes is always weaker. Note that the top right plot is the configuration achieving maximum C_p, and the bottom left is the one with the lowest C_p (Figure 4.8). Best performance is obtained when the isolated *streamwise* vortex appears for the frst time. On the other hand, the worst one is the last configuration with the pair of counter-rotating vortexes. This suggest that the pair of vortexes is beneficial for C_p and it *should* be maximised, but the interaction with the strong tip gap vortex is detrimental to the overall performance.

In order to understand the cause of these flowfields it is useful to follow the flow from the tip gap (Figure 4.24, 4.25 and 4.26). For very small gaps, Figure 4.24, the scraping vortex at the inducer is very strong and pushes the tip gap flow towards the hub. Note that for the smallest tip gap there is no leakage at the leading edge, and scraping flow moves from suction to pressure side. As scraping reduces, the tip gap flow is not pushed that much and both vortexes balance each other: scraping vortex is a *high energy structure* and tends to move towards the hub, while tip gap flow is a *low energy structure* and tends to float towards the shroud[5].

For medium size gaps, Figure 4.25, the same happens at the inducer region. However, there is a point along the blade, once the scraping has been reduced, where the tip gap flow is strong enough to overcome the scraping vortex and it is not pushed down anymore. At this point the original scraping vortex is separated from the casing and a new, stronger tip gap vortex sits in the suction side-shroud corner. This vortex is formed by low momentum flow, and thus it stays at the shroud. New scraping flow is dragged around this second tip gap vortex. Note that in geometries with *streamwise increasing* tip gap this process happens further downstream, and thus the isolated tip gap vortex is weaker. This is because the smaller leading edge tip gap allows the casting of a stronger scraping vortex that it is going to be able to *counteract* the tip gap flow, compare left and right top plots in Figure 4.25. For the worst performing case (bottom left), this process happens almost at the inducer and thus the counter-rotating pair of vortexes is almost dissipated in the channel. It is the existence of this structures casted at the passage inlet is what makes the leading edge gap such an important parameter for turbine diffuser interaction.

In the biggest tip gap configurations the leakage flow always overcomes scraping and an isolated strong tip leakage vortex occupies the shroud of the passage.

4.3.3. Entropy field

It is also interesting to analyse the entropy field (Figure 4.27, 4.28 and 4.29). As mentioned, shrouded rotor shows a high entropy region close to the casing that results in diffuser boundary layer separation. When scraping is added, this high entropy region is displaced down (Figure 4.27). Very small tip gaps generate a more diffuse high entropy region, with lower peak value and more circumferential space taken. In medium size gaps, Figure 4.28, it is possible to see how the high entropy region due to the vortex pair still exist, but a high entropy spot due to the new tip gap leakage vortex appears at the shroud. For $\epsilon_{Avr} = 4\%\ h_{LE}$ there is still a low entropy region close to the diffuser wall, but this is reduced as the isolated vortex gains presence. Finally, for the biggest gaps (Figure 4.29) all the upper mid span passage region is a high entropy region. For *streamwise increasing gaps* the entropy is less dispersed, but the flux of it is very similar (Figure 4.7 right). Regarding the isentropic jets reported by Dambach et Al. (2001, [33]), they exists from $\epsilon_{Avr} = 2\%\ h_{LE}$ onwards (Figure 4.27), what corresponds to $\lambda \approx 0.15 - 0.2$ (Figure 4.16). This is in good agreement with the value they report. However, this isentropic jet is deflected towards the hub by the scraping flow, and it is not up to bigger λ parameters when the jet overcomes scraping and emanates from the gap tangentially. It is this change what affects the flowfield, and not the existence or not of an isentropic jet.

[5] See plots about kinetic energy, Figure 4.30.

4.3.4. Energy fields

These last two fields are reported for consistency shake and supporting some previous claims. It has been said that the scraping vortex is formed by *high energy* flow and tip gap vortex by *low energy* flow. It is possible to see this in Figure 4.30, 4.31 and 4.32, where kinetic energy in the relative frame is shown. By comparing these plots with the previous, it is possible to always identify tip leakage as lower energy (blue and green) and scraping flow as high energy (green and red). This explains the tendency of scraping flow to go towards the hub and that one of leakage flow to stay at the shroud. The origin of this high energy regions is found in scraping, and to prove this Figure 4.33, 4.34 and 4.35 show the rothalpy fields. It is possible to find a higher-than-average region of rothalpy at the inducer shroud, and then this is diffused across the passage by the vortical structures. Rothalpy is only conserved in the shrouded rotor, where the low energy (rothalpy) flow has been convected to the suction side - shroud corner by secondary flows, but the flux remains constant. Figure 4.36 shows the change in rothalpy over $C_p T_{0t}$. This can be identified as the work done *by the rotor* to overcome casing scraping (windage) losses. It mainly depends on leading edge tip gap size, what is aligned with the previous discussion about the leading edge being the most important region in scraping phenomena. The increase in scraping losses with leading edge gap is related to the tip gap leakage. This leakage flow is opposed to the casing rotation direction and thus it increases the velocity gradients and viscous losses.

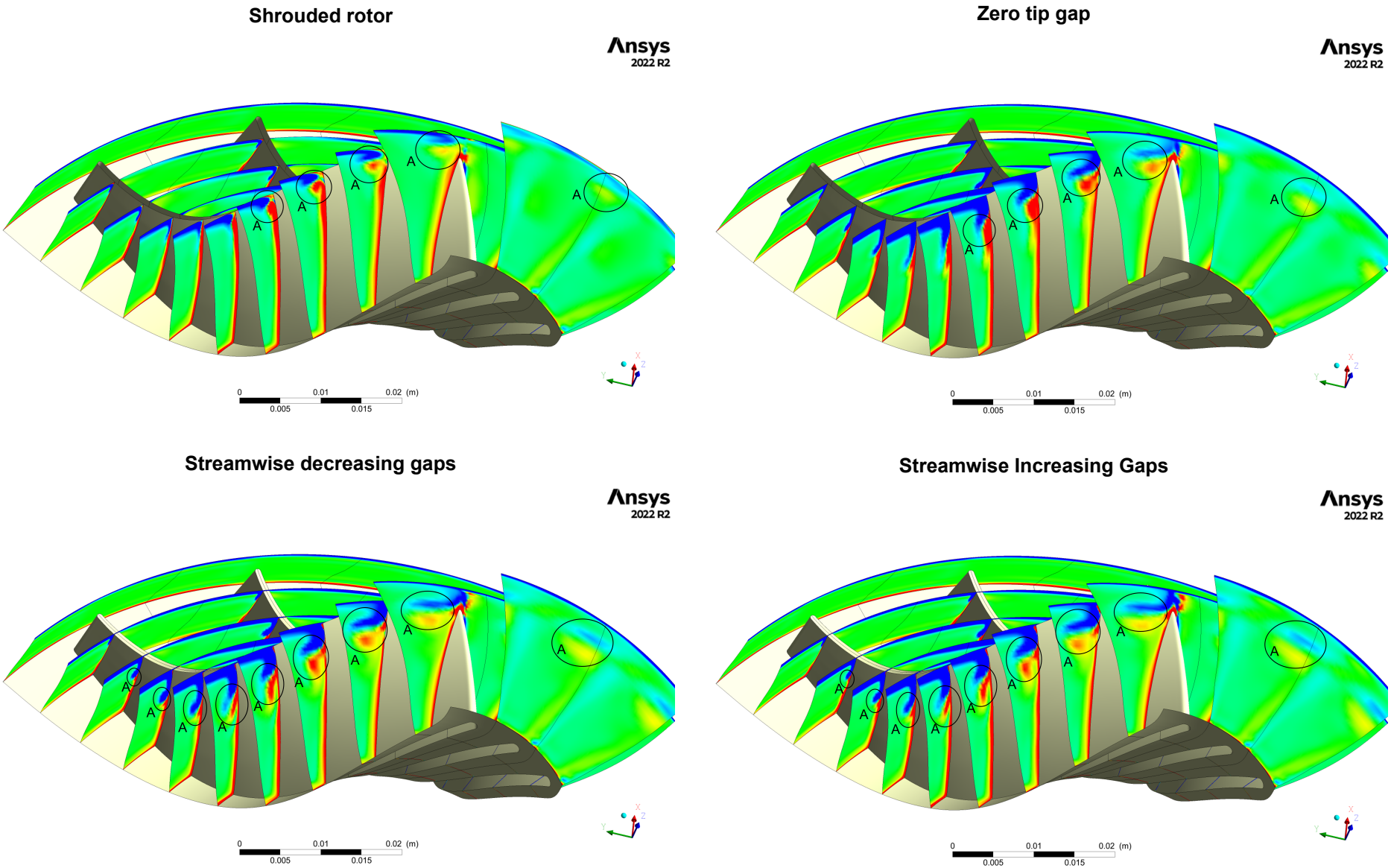

Figure 4.21: Streamwise vorticity field ($\frac{\vec{\omega}\cdot\vec{v}}{|\vec{v}|}$) (min: $-10000\ s^{-1}$, max: $10000\ s^{-1}$). Second Row: $\epsilon_{Avr} = 2\%\ h_{LE}$.

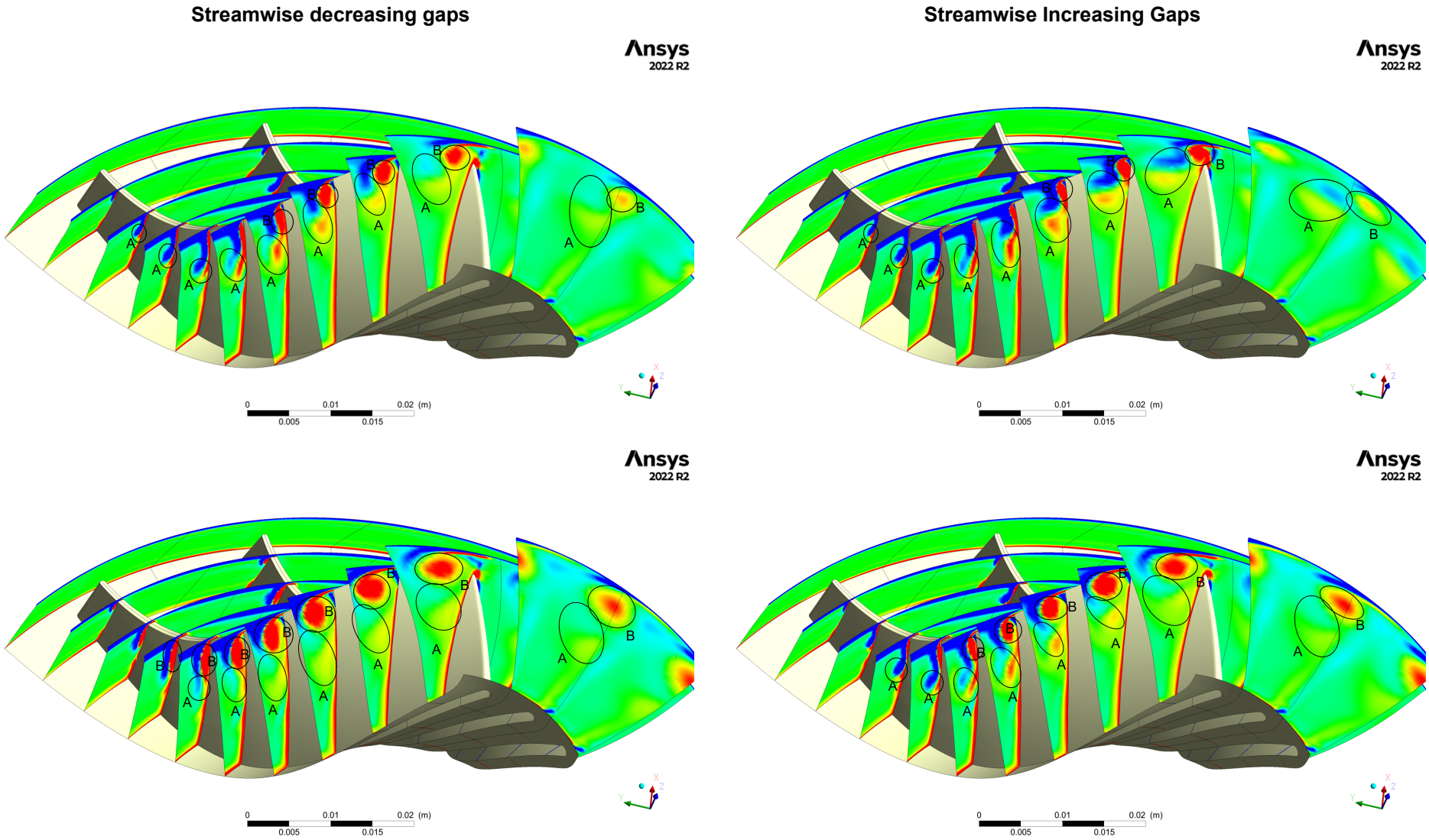

Figure 4.22: Streamwise vorticity field ($\frac{\vec{\omega}\cdot\vec{v}}{|\vec{v}|}$) (min: $-10000\ s^{-1}$, max: $10000\ s^{-1}$). First row: $\epsilon_{Avr} = 4\%\ h_{LE}$; Second Row: $\epsilon_{Avr} = 6\%\ h_{LE}$.

Figure 4.23: Streamwise vorticity field ($\frac{\vec{\omega}\cdot\vec{v}}{|\vec{v}|}$) (min: $-10000\ s^{-1}$, max: $10000\ s^{-1}$). $\epsilon_{Avr} = 10\%\ h_{LE}$.

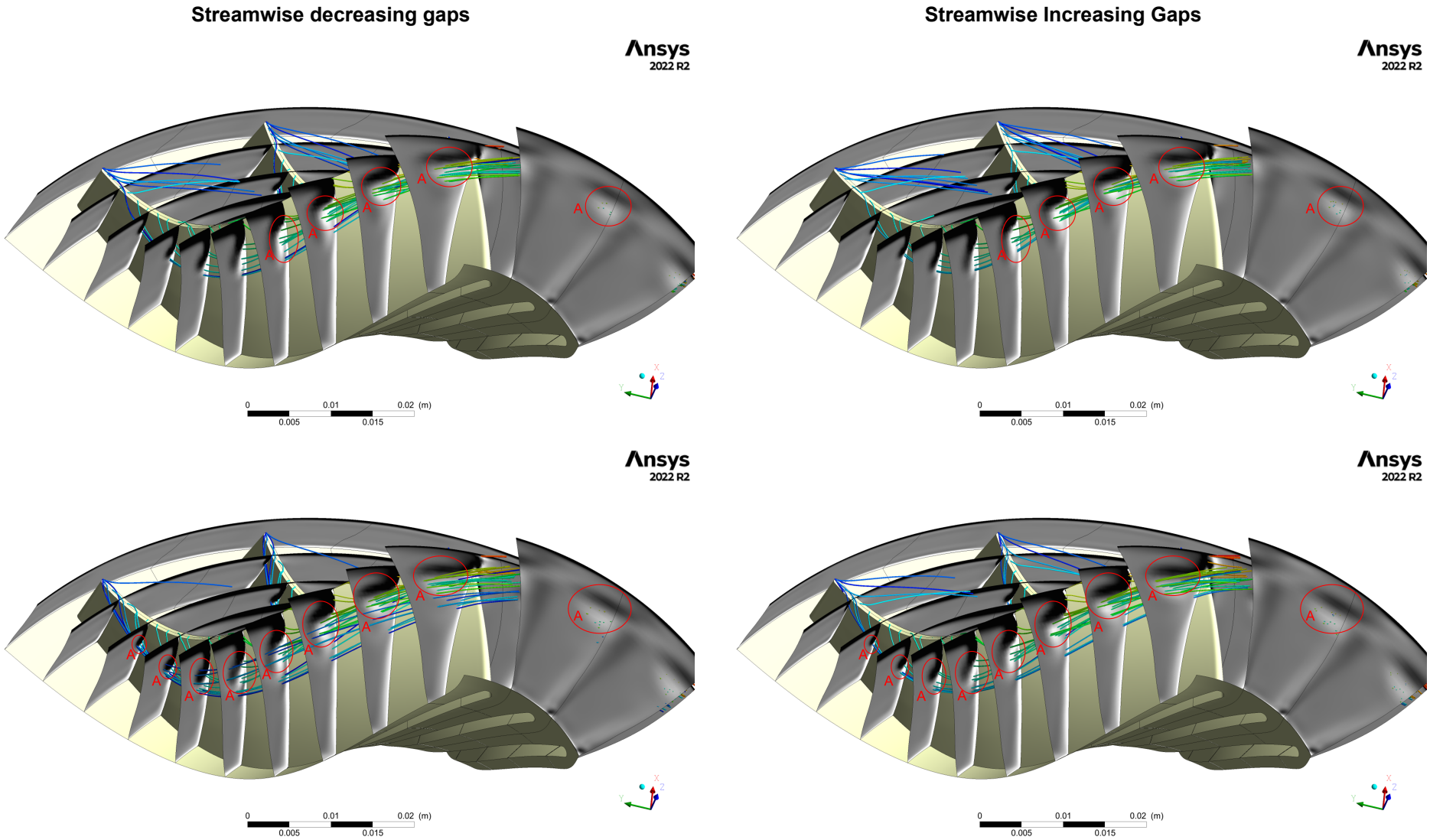

Figure 4.24: Streamlines emanating from the tip gap cavity. Black are *upstream vortexes* and white are *Streamwise vortexes*.
First Row: $\epsilon_{Avr} = 1\%\ h_{LE}$; Second Row: $\epsilon_{Avr} = 2\%\ h_{LE}$.

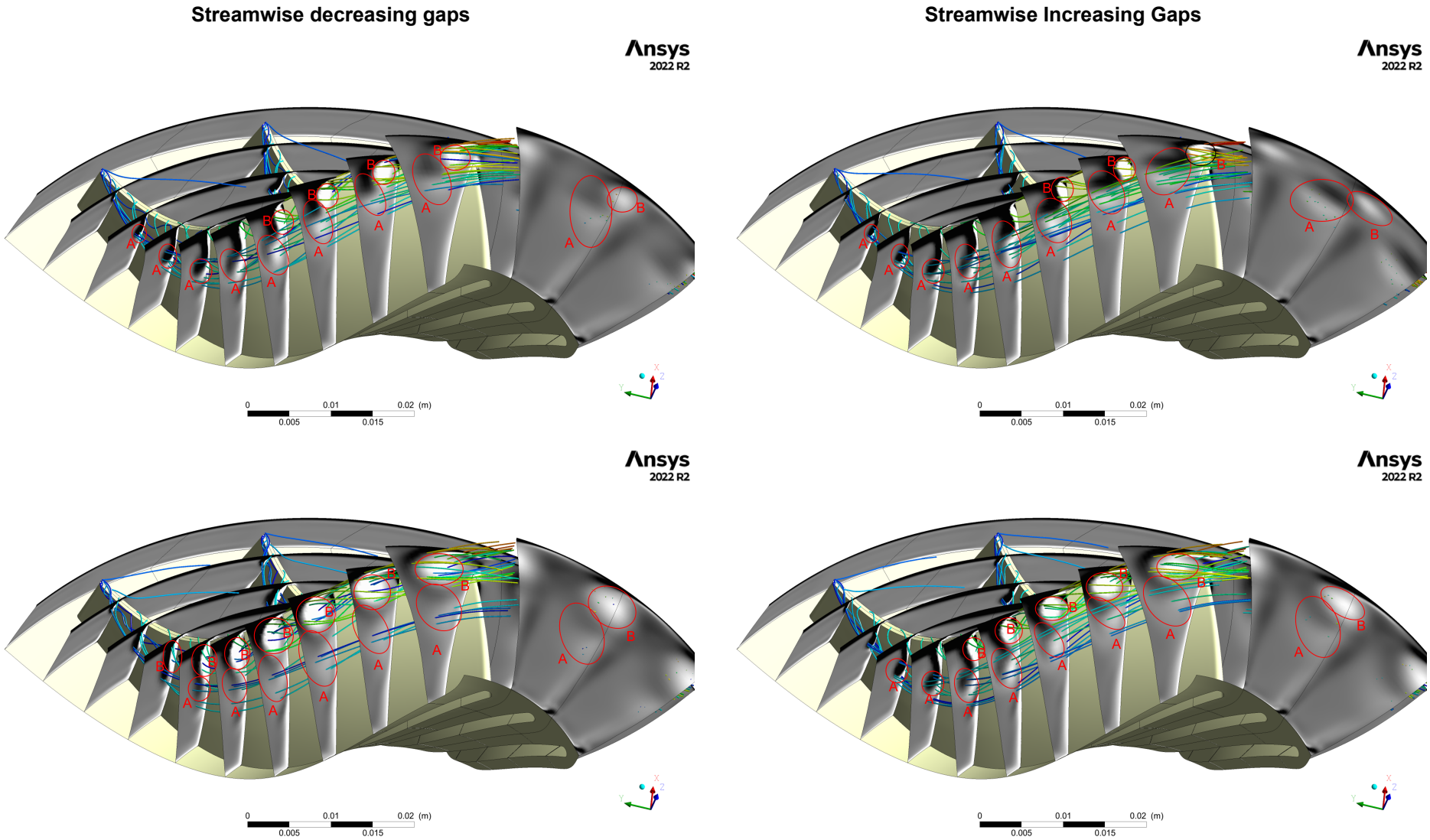

Figure 4.25: Streamlines emanating from the tip gap cavity. Black are *upstream vortexes* and white are *Streamwise vortexes*. First row: $\epsilon_{Avr} = 4\%\ h_{LE}$; Second Row: $\epsilon_{Avr} = 6\%\ h_{LE}$.

Figure 4.26: Streamlines emanating from the tip gap cavity. Black are *upstream vortexes* and white are *Streamwise vortexes*. $\epsilon_{Avr} = 10\%\ h_{LE}$.

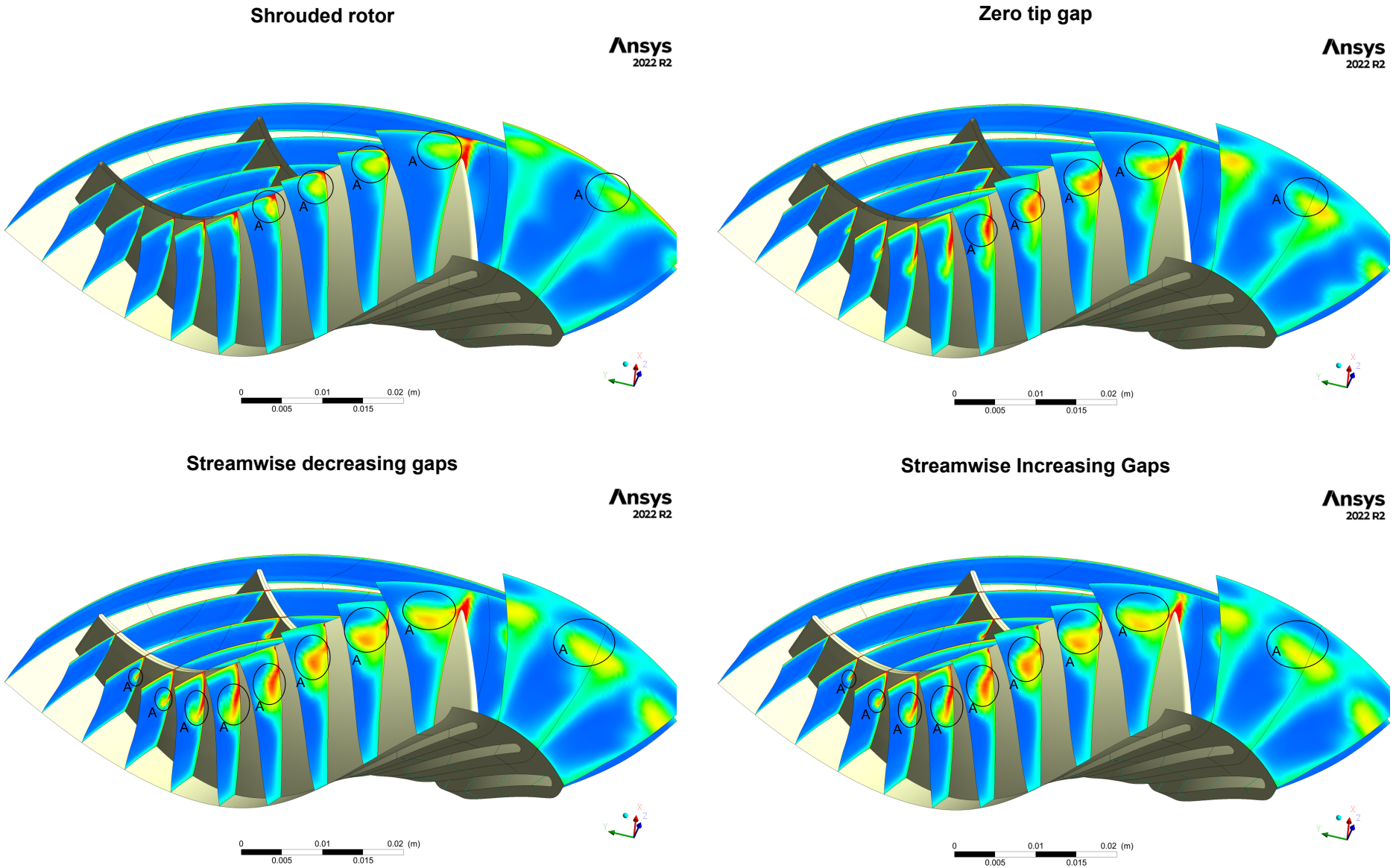

Figure 4.27: Rotor entropy field (min: $70\ J/kg{\cdot}K$, max: $250\ J/kg{\cdot}K$). Second Row: $\epsilon_{Avr} = 2\%\ h_{LE}$.

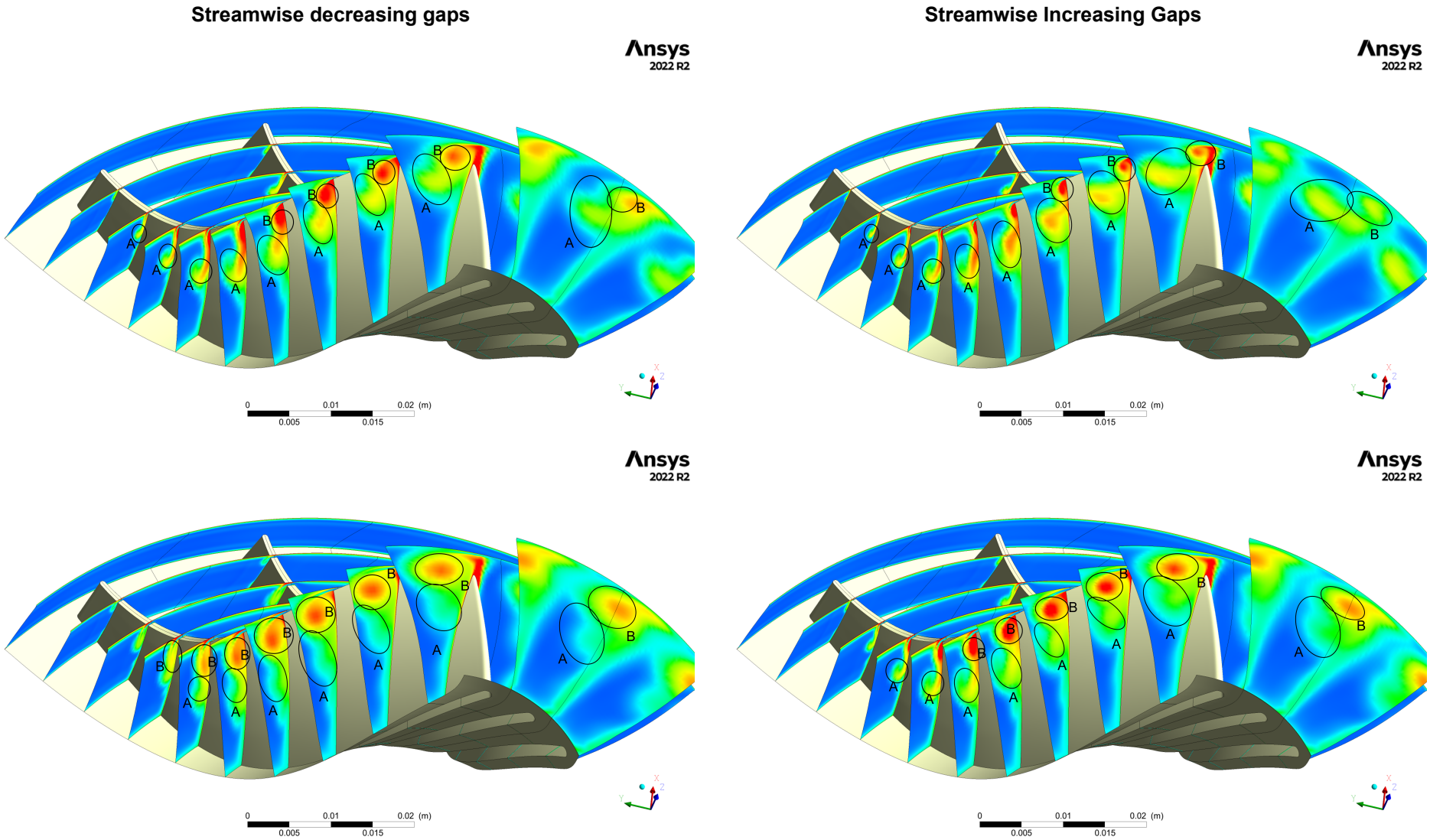

Figure 4.28: Rotor entropy field (min: $70\ J/kg{\cdot}K$, max: $250\ J/kg{\cdot}K$). First row: $\epsilon_{Avr} = 4\%\ h_{LE}$; Second Row: $\epsilon_{Avr} = 6\%\ h_{LE}$.

Figure 4.29: Rotor entropy field (min: $70\ J/kg{\cdot}K$, max: $250\ J/kg{\cdot}K$). $\epsilon_{Avr} = 10\%\ h_{LE}$.

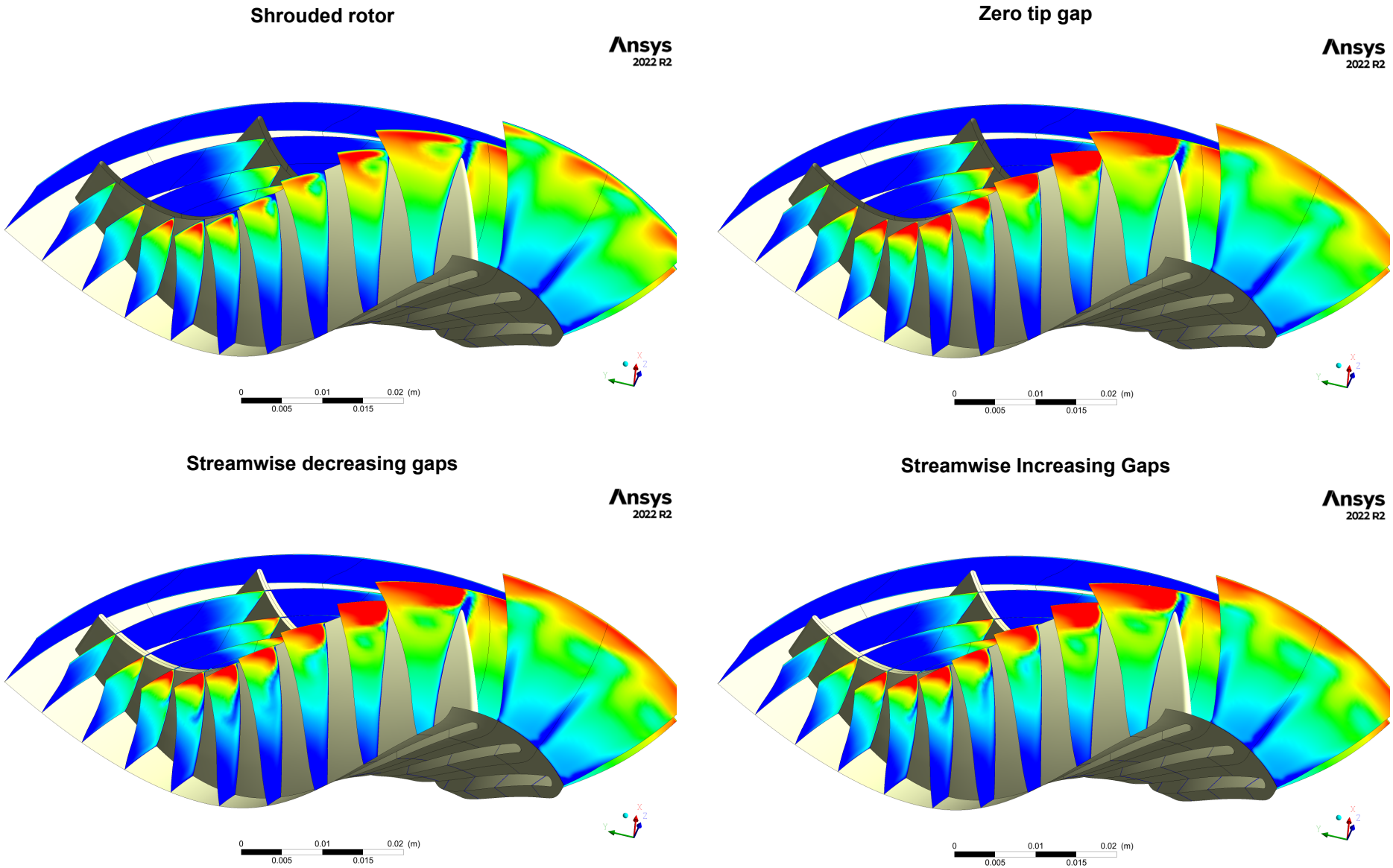

Figure 4.30: Rotor relative kinetic energy field (min: $10\ kJ/kg$, max: $50\ kJ/kg$). Second Row: $\epsilon_{Avr} = 2\%\ h_{LE}$.

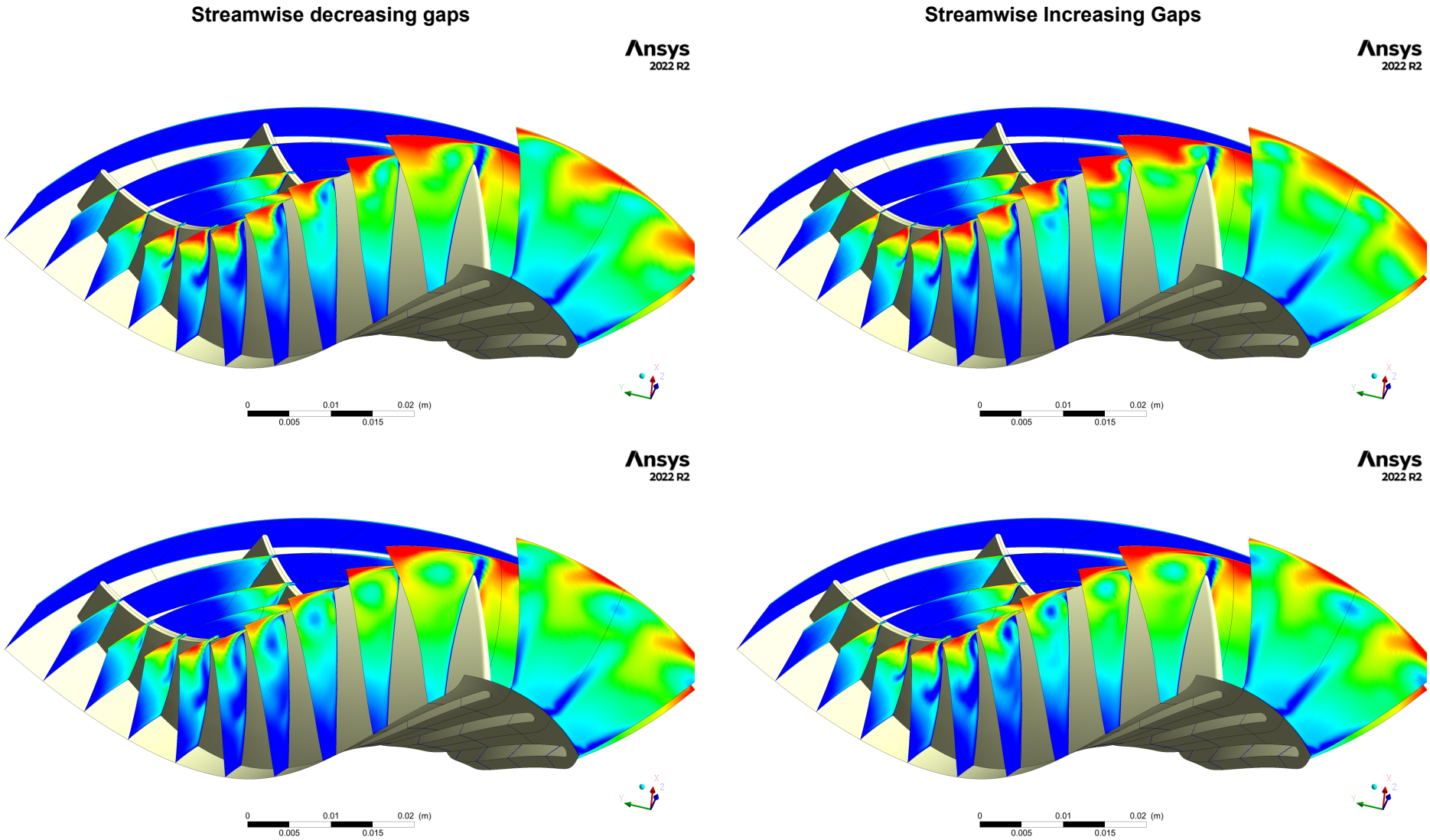

Figure 4.31: Rotor relative kinetic energy field (min: $10\ kJ/kg$, max: $50\ kJ/kg$). First row: $\epsilon_{Avr} = 4\%\ h_{LE}$; Second Row: $\epsilon_{Avr} = 6\%\ h_{LE}$.

Figure 4.32: Rotor relative kinetic energy field (min: $10\ kJ/kg$, max: $50\ kJ/kg$). $\epsilon_{Avr} = 10\%\ h_{LE}$.

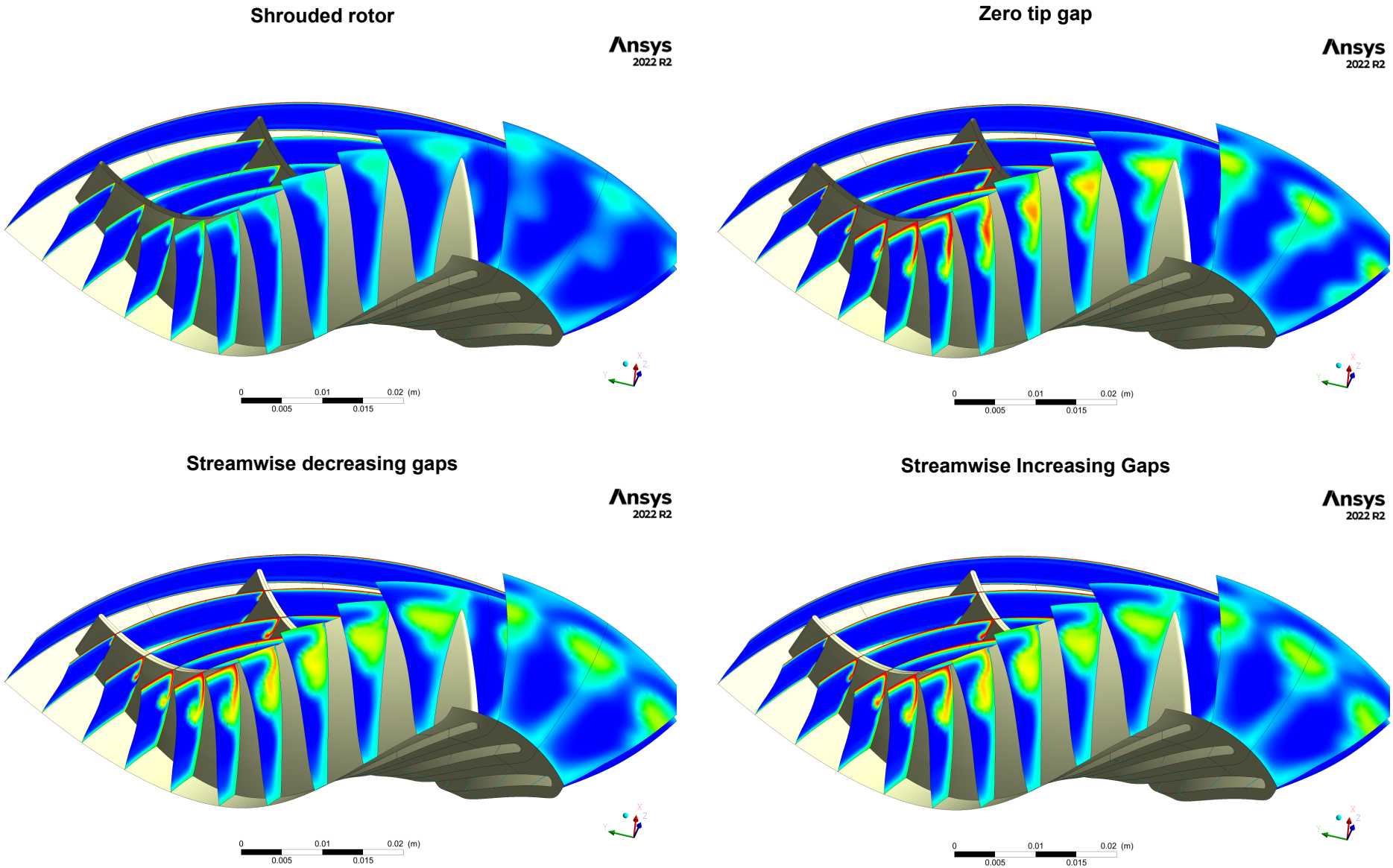

Figure 4.33: Rothalpy field (min: $0\ kJ/kg$, max: $40\ kJ/kg$). First row: Second Row: $\epsilon_{Avr} = 2\%\ h_{LE}$.

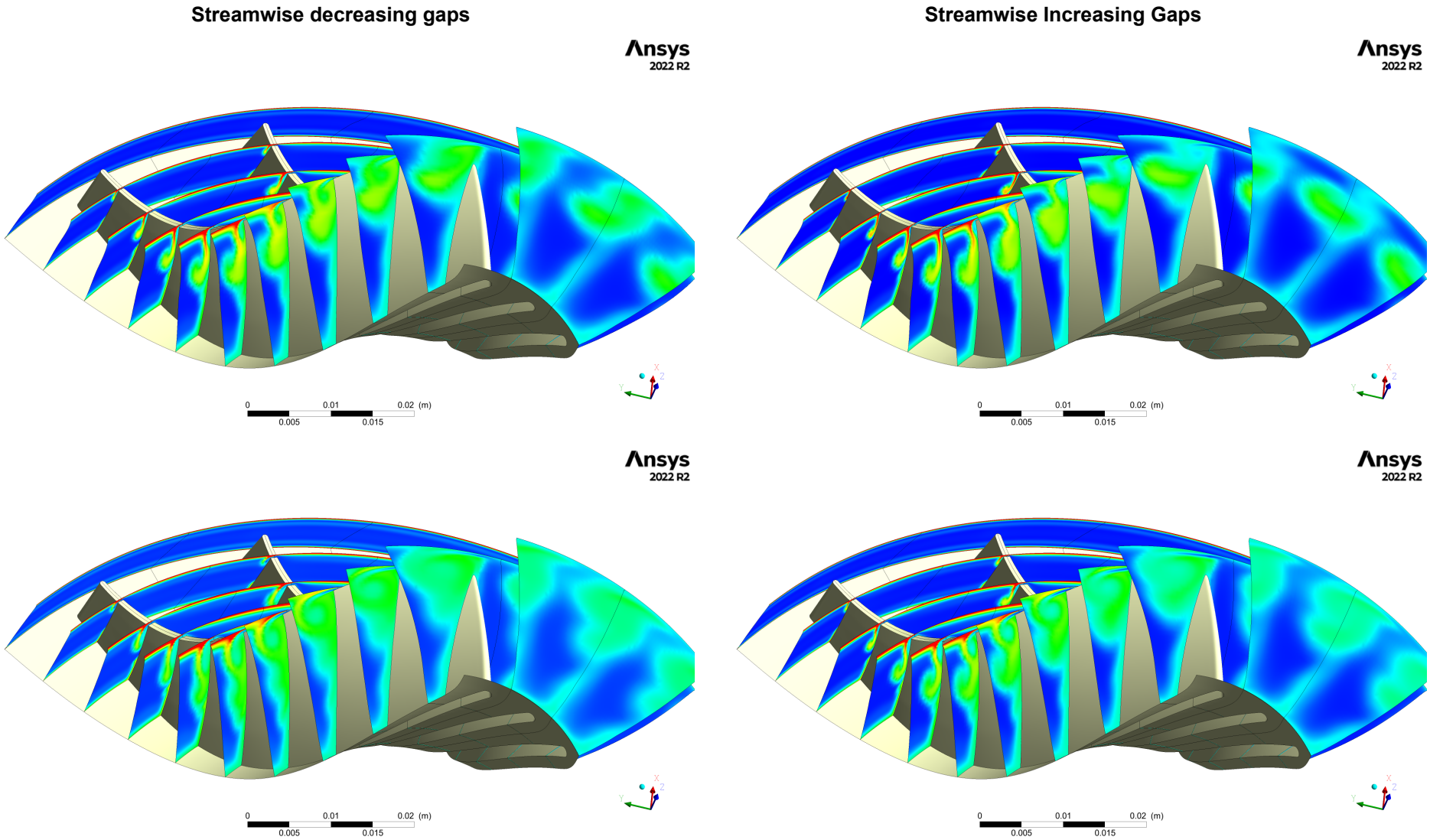

Figure 4.34: Rothalpy field (min: $0\ kJ/kg$, max: $40\ kJ/kg$). First row: $\epsilon_{Avr} = 4\%\ h_{LE}$; Second Row: $\epsilon_{Avr} = 6\%\ h_{LE}$.

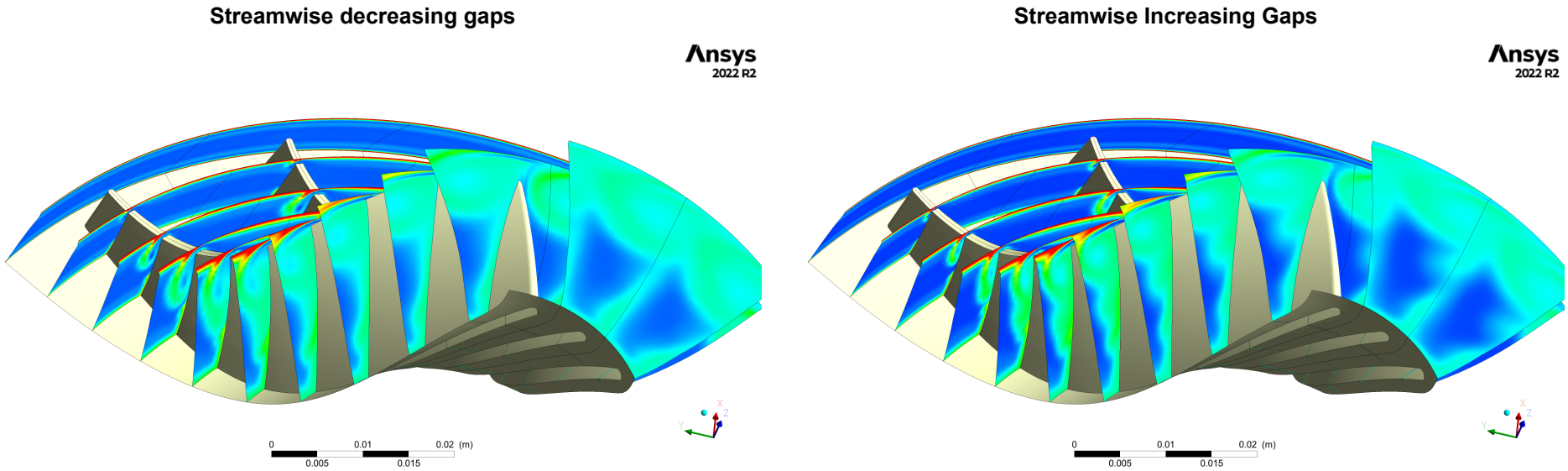

Figure 4.35: Rothalpy field (min: $0\ kJ/kg$, max: $40\ kJ/kg$). $\epsilon_{Avr} = 10\%\ h_{LE}$.

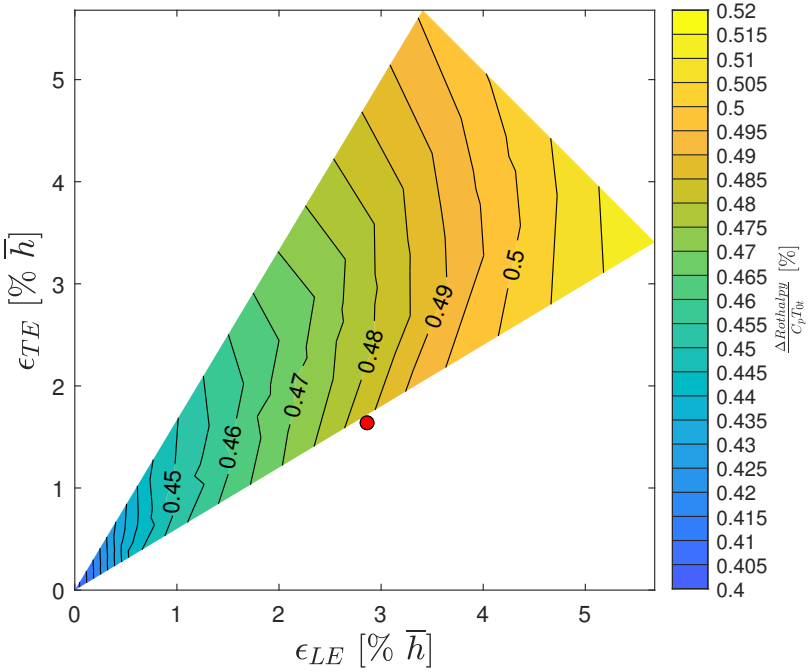

Figure 4.36: Increment in Rothalpy along the rotor for different tip gap configurations. Note that scraping is the only mechanism able to change this magnitude. $\frac{\Delta Rothalpy}{C_p T_{0t}}$ [%]

4.4. Evolution of flow structures through the diffuser

It is the evolution of these different flow structures what changes the performance of the diffuser. Figure 4.37 shows the development of vorticity for different tip gap configurations. Each column contains different ϵ_{Avr}, and moving down rows corresponds to axial progression along the diffuser. Every plot is a combination of *decreasing tip gaps* (top left), *increasing tip gaps* (top right) and *uniform tip gaps* (bottom). The turbine rotates counterclockwise as seen in the drawing, and the flow is slightly swirling in the same direction. The left most column contains the results for a *very small* tip gap. It is possible to observe the two counter rotating vortexes described earlier as two red and blue spots and the wakes of the turbine as red and blue radial structures. The two vortexes remain coherent and away from the walls throughout the entire device length. For configurations with $\Delta_\epsilon > 0$ the scraping vortex lasts longer, what supports the discussion about smaller leading edge gaps casting stronger vortical structures. The right most column shows a *very big* tip gap. For every tip gap distribution it is possible to find a large *red* spot: the tip gap leakage vortex. The rest of the passage is filled with the *upstream* vorticity related to scraping flow. The bigger leakage vortexes separate from the scraping vortex and they migrate towards the mid radius of the diffuser, where they coalesce into a high vorticity annular region. The scraping vortexes remain as individual structures and migrate towards the wall, where they visibly interact with the boundary layer. Lastly, the two middle columns show the *medium size gaps* that transition between these two flow configurations. It is possible to find the counter rotating pair and the isolated tip gap vortex at the inlet as discussed previously, and for *streamwise decreasing* gaps ($\Delta_\epsilon < 0$) the configuration is more reminiscence of that of *big gaps*. For the best performing configuration (2^{nd} column, top right; $\epsilon_{Avr} = 4\%\ h_{LE}$; $\Delta_\epsilon = +50\%$) The counter-rotating pair evolves very similarly to *small tip gaps*, and there is an additional *upstream* (scraping) vortex close to the diffuser wall. Note that these counter-rotating vortexes dissipate quicker than for the case of *small tip gaps*. For the worst performing cases (top left in both central columns) the counter-rotating pair dissipates very differently due to the interaction with the isolated tip leakage vortex. Note that only configurations reminiscent of *big gaps* generate vortexes close to the boundary layer.

Figure 4.38 shows the distribution of Mach number. In these plots magenta lines are iso-contours of $w_{axial} = 0$, so they identify recirculating regions. The wakes are shown in these plots as low Mach number radial regions. Note that in every case the tip leakage vortex is related to a low velocity region, whereas scraping vortexes appear as *jets*. In configurations with *small tip gaps* the scraping flow has migrated away from the wall, what generates low velocity regions close to the diffuser casing and local recirculation strikes along the wakes. This is avoided in *big tip gaps* because of the migration of high energy scrapping vortex flow towards the casing. This might be the reason explaining why the best performing diffuser is in the transition region: it has the counter-rotating pair that dissipates efficiently, but also a high velocity region close to the wall reinforcing the boundary layer.

Lastly, Figure 4.39 shows contours of the loss coefficient. In these plots the tip leakage vortex appears as a very high loss region (red) and the scraping flow as low loss regions (blue). As discussed above, for *small* tip gaps all vortical structures remain far away from the wall, and thus the diffuser boundary layer develops as a high loss region. With *big* tip gaps, the low energy flow from the tip gap leakage migrates towards the middle of the channel and thus the wall region is reinforced by the high energy flow resulting from scraping. It is this characteristic what avoids diffuser stall. Note that for mid-size tip gaps, the counterotating pair avoids the migration of the isolated leakage vortex towards the middle, and this is very detrimental to the boundary layer state. Finally, the outlet of the diffuser is more uniform for *big* tip gaps.

Figure 4.40 contains the meridional view of all of these flowfields. Note how only the bigger tip gaps (lower rows) interact with the boundary layer, and how this results in less losses close to the wall. Also, the quicker mixing of the tip leakage vortexes for *big* tip gaps results in a more uniform flow. As a summary, the flow structures from *small* tip gaps dissipate producing a greater static pressure rise, whereas *big* tip gaps flow structures tend to migrate towards the diffuser wall, re-energizing the boundary layer. However, they do not provide such a big pressure recovery. Best performance is found in a mid-region where these effects are both exploited. However, if they are not balanced, their interaction produces the worst possible diffuser performance.

4.4.1. Research Question 4

Research Question 4

What is the physical interaction mechanism between turbine and diffuser?

Three kinds of flow modes have been identified depending on tip gap size and distribution. For small gaps two counter-rotating vortexes leave the turbine, located approximately one vortex diameter bellow the casing. This generates a low loss region close to the diffuser wall that avoids the stalling found in shrouded rotors. For the biggest tip gaps, there is only one isolated vortex associated to tip gap leakage, and the scraping flow is convected around it. For medium tip gaps, a gradual mixture between the two flow structures is found. Maximum diffuser performance is obtained when the pair of vortexes is the strongest possible before casting a big isolated vortex, whereas worst diffuser performance is obtained when a strong isolated vortex coexists with the counter-rotating pair. Furthermore, it has been discovered that the value of λ^* that changes performance is the one where the isentropic jet is strong enough as to overcome the scraping flow, and not the one when it appears for the first time.

The disipation of all vortical structures generates a static pressure rise. The isolated vortex generates high mixing losses when dissipating in the diffuser. However, the counter-rotating pair generates lower losses than the isolated vortex. It is the dissipation of these vortexes what drives turbine-diffuser interaction, and the counter-rotating vortex is more efficient in doing this. Furthermore, the scraping vortex in the case of big tip gaps is convected close to the diffuser wall, while for small tip gaps it stays at the centre. This implies that, even though the structures for small tip gaps are more *effective*, they might not be as good as the others in avoiding boundary layer separation. More research is needed in this topic.

Finally, the greater influence of the leading edge tip gap is explained by the higher scraping in this region. The structures casted at the inducer region can leave the rotor, and they affect the evolution of all the shroud processes further downstream along the rotor.

$\epsilon_{Avr} = 2\%\ h_{LE}$ $\epsilon_{Avr} = 4\%\ h_{LE}$ $\epsilon_{Avr} = 6\%\ h_{LE}$ $\epsilon_{Avr} = 10\%\ h_{LE}$

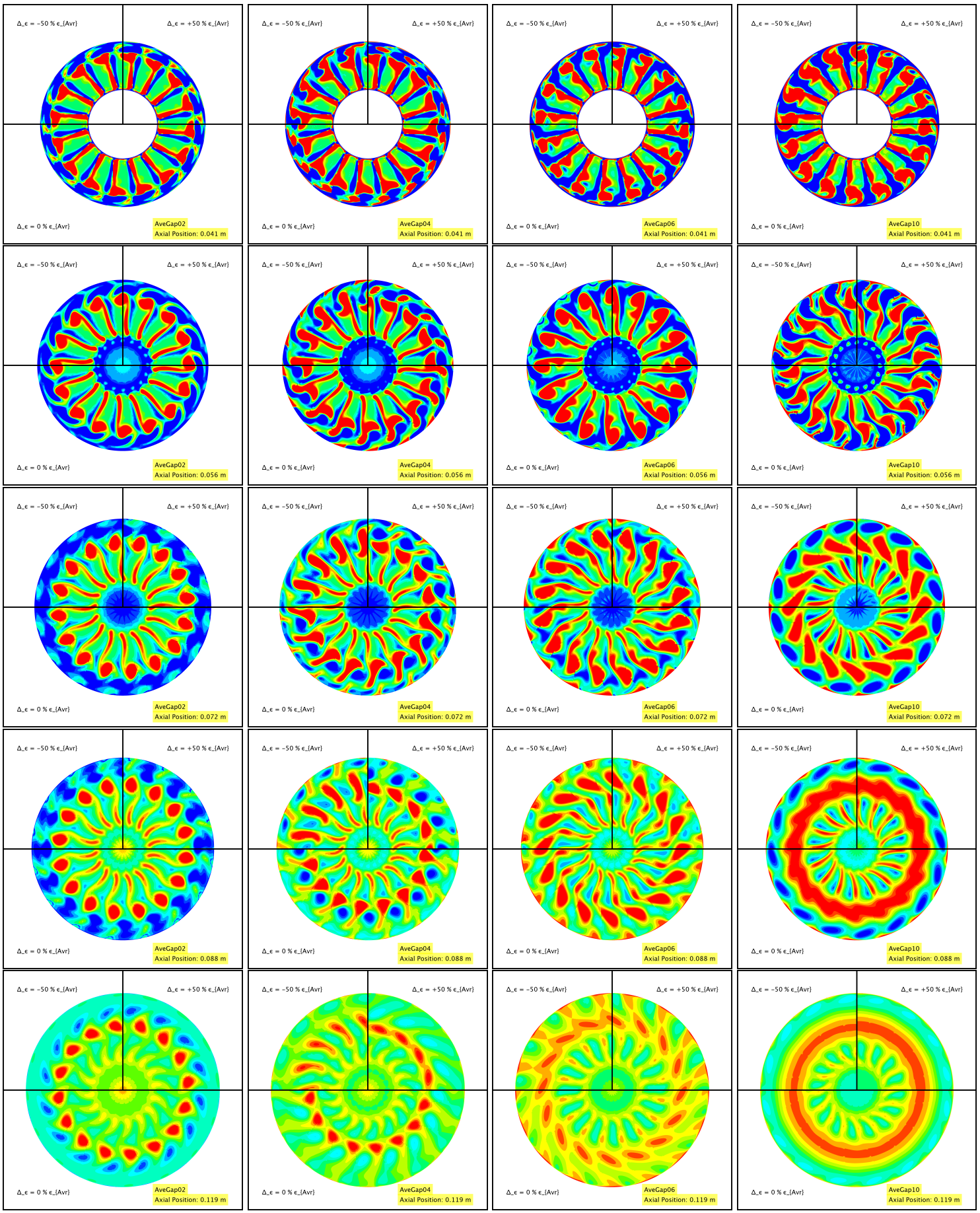

Figure 4.37: Helicity (min: $-7500\ s^{-1}$, max: $7500\ s^{-1}$)

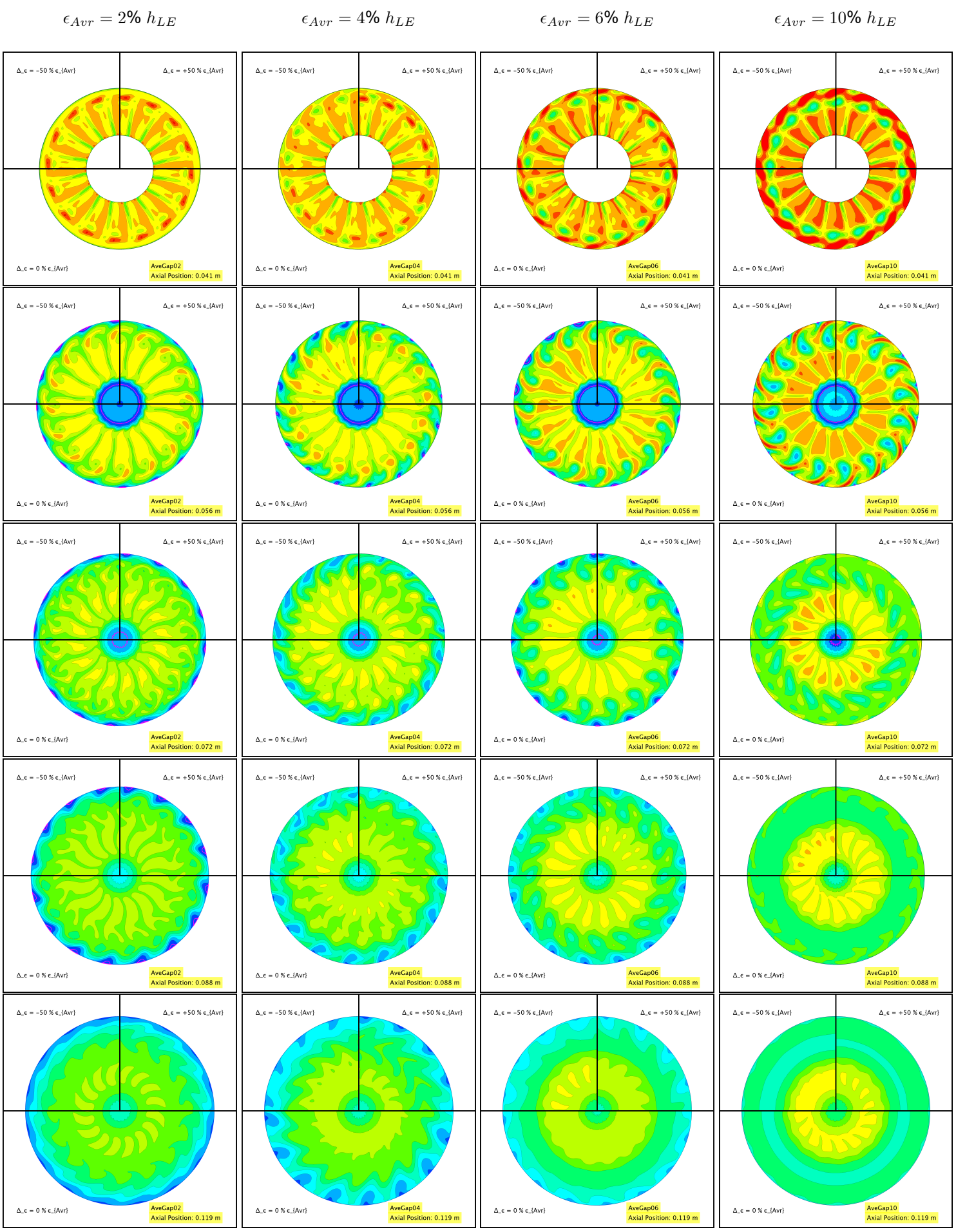

Figure 4.38: Mach number (min: 0, max: 0.5)

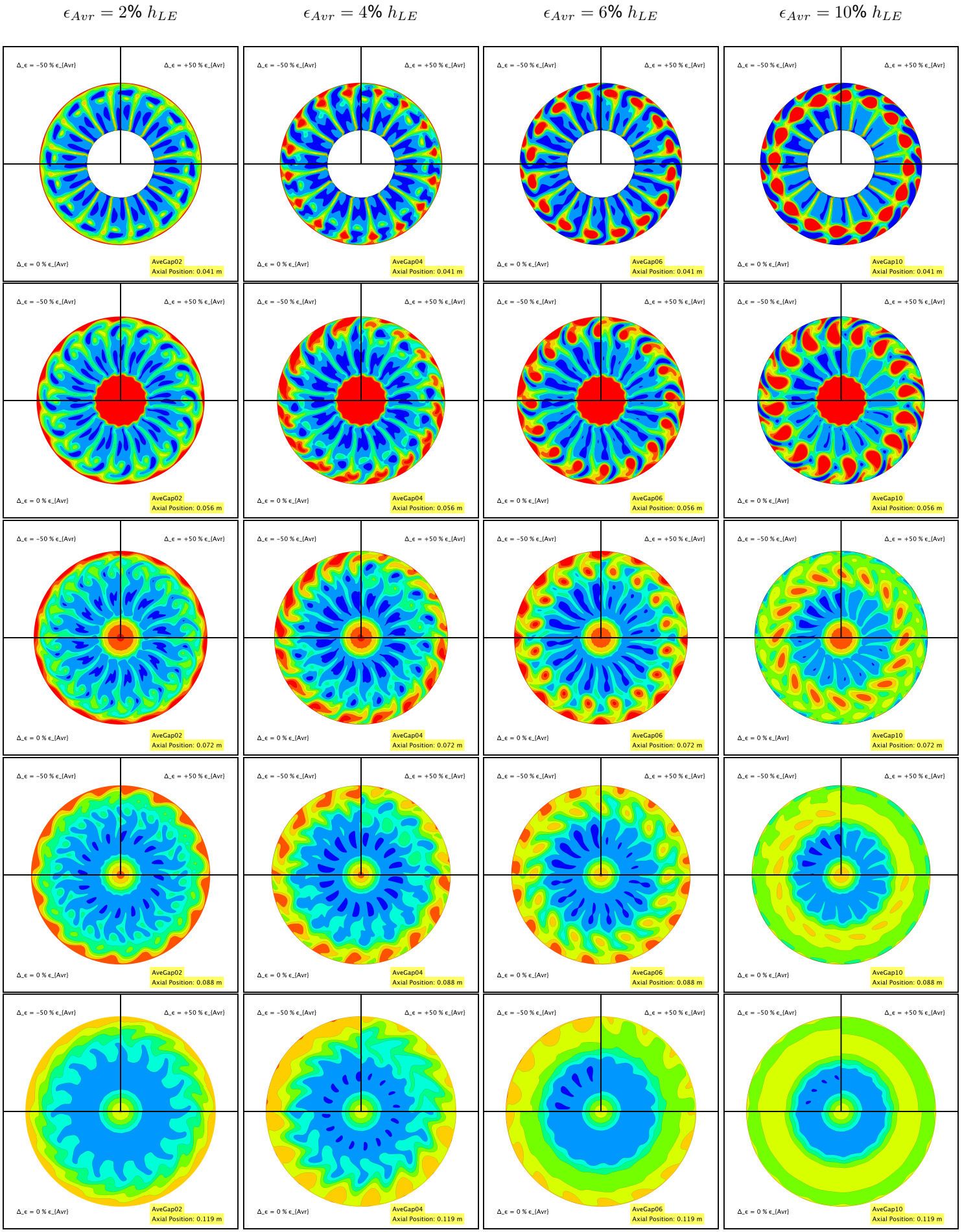

Figure 4.39: Loss Coefficient k_{loss} (min: -0.2, max: 0.6)

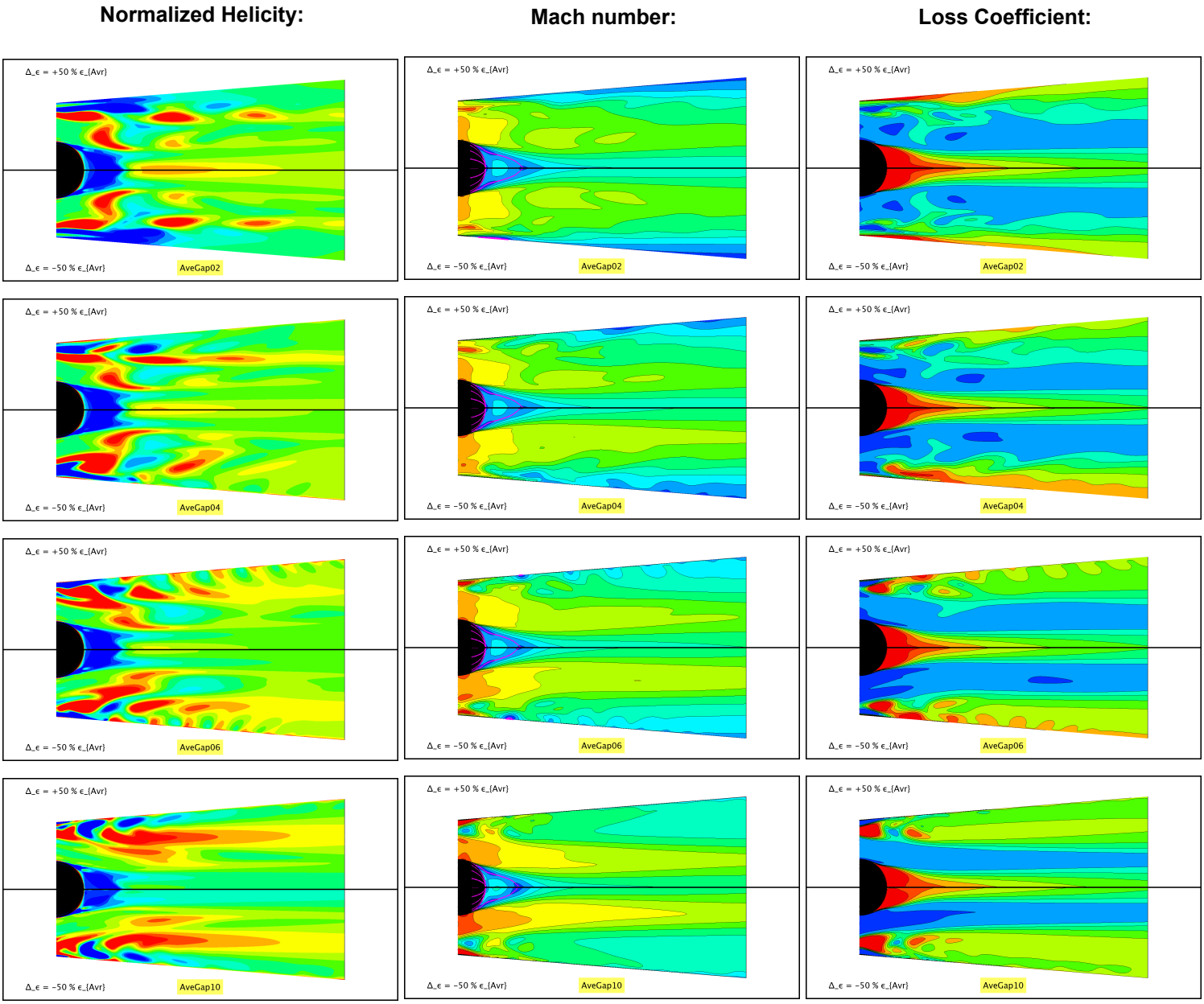

Figure 4.40: Meridional view of the diffuser for different tip gap configurations. Same limits as cross-section plots. Each row is ϵ_{Avr} = 2, 4, 6, and 10 %h_{LE}. In each diffuser, the upper half is $\Delta_\epsilon = +50\%\ \epsilon_{Avr}$ and the lower half is $\Delta_\epsilon = -50\%\ \epsilon_{Avr}$

4.5. Generalization of the results

4.5.1. ORCHID turbine

The turbine used in this section has been designed by Delft University of Technology Propulsion & Power department. It is intended to be build and tested in a new experimental set up called *Organic Rankine Cycle Hybrid Integrated Device* (ORCHID) (Bahamonde et al. 2017 [50]). This is a well-studied case withing the department.

Design Characteristics

The publication by Bahamonde et al. (2017, [50]) exposes a novel design method optimizing the parameters of an Organic Rankine cycle (ORC) coupled to the design of the turbine. This is done in the context of a heat recovery system for transport applications. In this paper they investigate different working fluids and turbine configurations. They conclude that the optimal solution is a high expansion ratio, single stage, radial inlet turbine operating with *siloxane MM* (hexamethyldisiloxane). This publication also identifies the operating conditions and target power generation. In a set of later publications, the same group performs the shape optimization of stator blades (Anand et al. 2019, [51]), rotor (De Servi et al. 2019, [52]) and stator-rotor radial spacing (Cappiello et al. 2022, [53]). These studies set the design and operating conditions of the ORCHID turbine, and the interested reader is redirected to them.

The design objectives are summarised in Table 4.2 and the main dimensions in Table 4.3. Figure 4.41 and Figure 4.42 show the geometry of the stator and rotor blades of the machine. Table 4.3 also contains the computational domain boundaries in the CFD simulation. They were chosen to be similar to those of the previous set up: stator inflow mantains the ratio $\frac{R_{BC}-R_{in}}{R_{in}-R_{out}}$ and rotor outflow maintains $\frac{L_{Domain}-L_{Rotor}}{R_{out}^{Srhoud}-R_{out}^{Hub}}$. Rotor stator interface is located at the mean radius of the radial gap in both simulations.

Table 4.2: Design objectives and duty coefficients for ORCHID turbine.

Design Parameters		**Duty coefficients**	
$\dot{W}$ $[kW]$	10.6	$\psi_2 = \frac{w}{U_2^2}$	1.1
Ω [RPM]	98000	$\phi_2 = \frac{v_{2m}}{U_2}$	0.29
T_{4t} $[K]$	573	α_3 $[deg]$	+15
P_{4t} $[kPa]$	1810	$R_3/R_{2,mid}$	0.557
$\dot{m}$ $[kg/s]$	0.132	v_{3m}/v_{2m}	≈ 1
β_{ts}	40.86	r	0.37
Working fluid	*siloxane MM*		
# Stator Blades	12		
# Rotor Blades	16		
U_2 $[m/s]$	264		

CFD Mesh

Both rotor and stator grids are structured O-grids generated with *Turbogrid*. The stator domain (Figure 4.43 c) has 1.44 thousand nodes (1.38 million hexahedral elements) and the rotor grid (Figure 4.43 a-b) has around 1.74 million nodes (1.67 million hexahedral elements). De Servi et al. (2019, [52]) provides a grid convergence study for the geometry and confirms that this mesh achieves grid-independent results.

4.5.2. ORCHID diffuser proposal

The ORCHID turbine is an ongoing project, and as such some parts are still missing. Namely, there is not a diffuser designed for this case. Different design criteria will push diffuser characteristics towards different directions. On the practical implementation in a transport system, minimizing weight and installation space will be of utmost importance[6]. However, in an experimental set up, other concerns, such as flow uniformity or accessibility, might be more important than size. In this study the ORCHID turbine is used as a test of

[6]This argument is stronger when considerations from Section 2.4 are taken into consideration. ORCHID turbine has a great pressure ratio of $\beta_{ts} \approx 41$, and this makes it less sensitive to C_p. The cost of a bigger diffuser is hard to argue through efficiency gains.

Table 4.3: Geometry parameters of the ORCHID turbine [52]. All lengths in mm, areas in mm^2 and angles in $[deg]$

Stator		**Rotor**		**Angles**	
R_{BC}	40	$R_{Mixing\ Plane}$	26.25	α_0	0
R_{in}	35.8	R_{in}	25.75	α_2	78
R_{out}	26.7	R_{out}^{Shroud}	20.5	α_3	15
h_{all}	2	R_{out}^{Mean}	14.4	β_2	35
Chord	22	R_{out}^{Hub}	8.3	β_3	-57.6
Total Throat area	19.2	L_{Rotor}	10		
TE thickness	0.2	$L_{Interface}$	11.3	**Clearances**	
M_{out}	1.92	h_{in}	2	ϵ_{LE}	0.2
		h_{out}	12.2	ϵ_{TE}	0.2

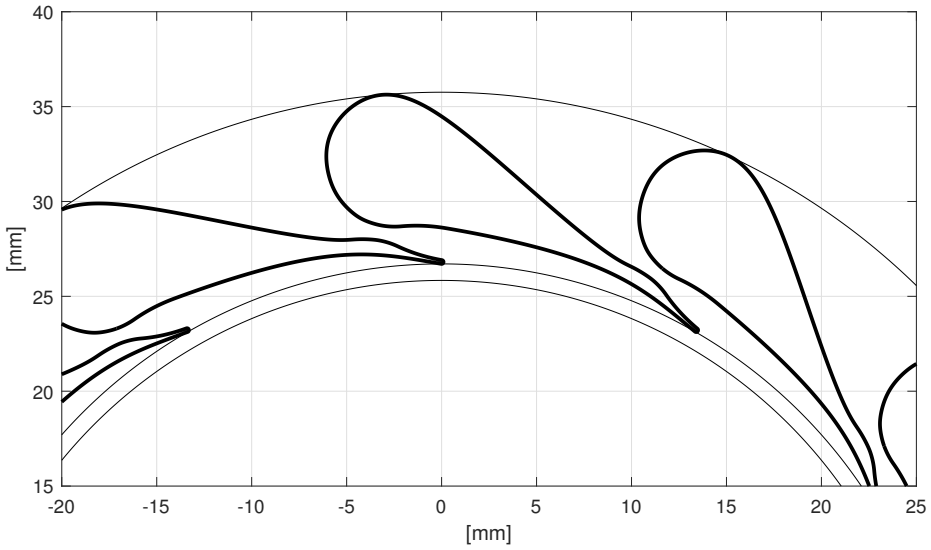

Figure 4.41: Orchid stator geometry. The stator is a straight prism. Thin black lines represent stator inlet radius ($35.8\ mm$), stator outlet radius ($26.7\ mm$) and rotor inlet $25.7\ mm$.

generality and applicability of previous results, and thus the diffuser will be the same as in the T-100 case ($L/R_1 = 1.3$, $AR = 2.2$, $\phi_{wall} = 4.61°$).This decision is going to provide exactly the same geometry and thus results will be easily comparable. Lastly, the diffuser domain includes a spherical spinner as the one used in the T-100 case.

The computational domain is discretized with a structured multi-block mesh. The topology is exactly the same as that in Figure 3.11. This time the extension is shorter (one diffuser length, or about 1.5 outlet diameters), and the grid is finer, containing 100 thousand elements in the diverging section (three times more than the original grid). No convergence study was performed in this grid due to the huge computational cost. The assumption is that this finer grid will provide results at least as good as the previous one. There are no visual differences with respect to Figure 3.11.

4.5.3. Comparison T-100 & ORCHID turbines

The main similitudes with the T-100 turbine are:

- Both machines are radial inflow turbines.
- Both rotors have 16 blades

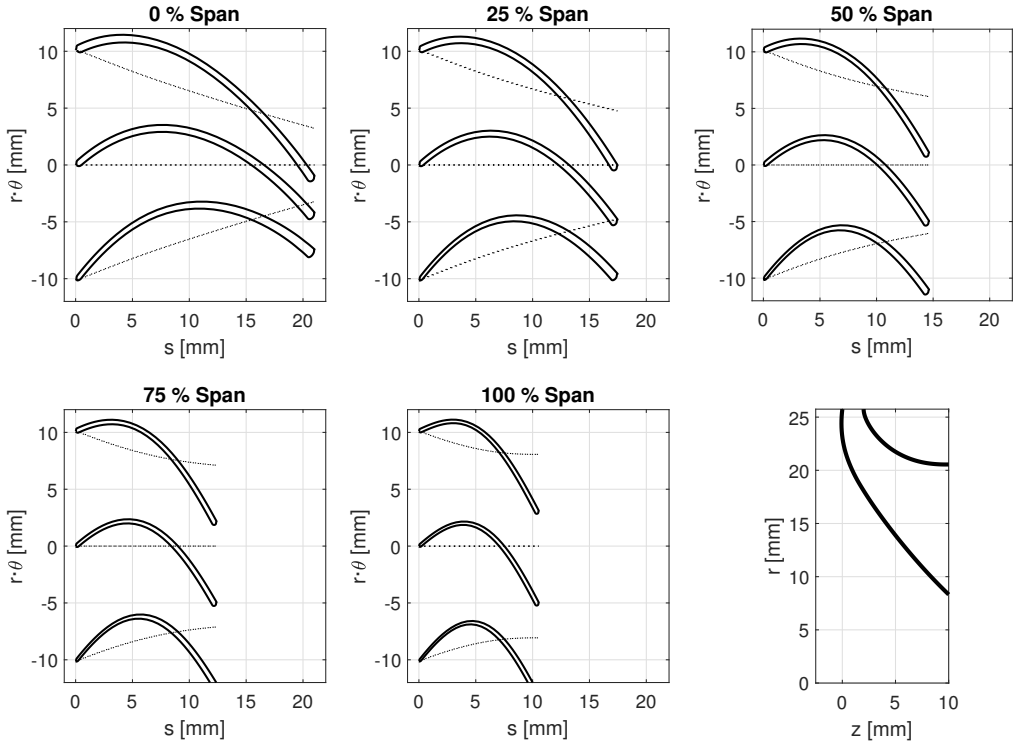

Figure 4.42: Rotor blades geometry for the ORCHID turbine. Tangential displacement $r{\cdot}\theta$ is plotted against meridional distance. Dotted lines are references such that $\theta = const.$.

- Both machines work with similar mass-flow (hundreds of grams per second).
- Both machines have the same design rotational speed ($100k$ RPM).
- Inlet to mean outlet radius is around 0.5 in both machines.
- hub to tip radius at the rotor outlet is $\frac{R_{hub}}{R_{tip}}\Big|_{Outlet} \approx 0.41$ in both machines (Figure 4.45).

And differences:

- ORCHID turbine works with non-ideal gases.
- ORCHID turbine pressure ratio is $\beta_{ts} \approx 41$, whereas T-100 is $\beta_{ts} \approx 5.7$.
- ORCHID stator is highly supersonic ($M_{outlet} = 1.92$), while T-100 is $M_{out} = 0.995$.
- ORCHID radial gap between rotor & stator is 5 times smaller in absolute size (2 times smaller in relative terms).
- ORCHID rotor blades present high inlet metal angle (≈ 40°, Figure 4.42 & Figure 4.44).
- ORCHID rotor blade thickness is around 30% of T-100 blade thickness at the tip.
- ORCHID on-design operation outflow has 15° swirl angle, whereas T-100 outflow is axial.
- ORCHID loading and flow coefficients are 20% and 50% higher than those in T-100.
- The meridional gas path has different curvature distributions (Figure 4.45).
- Orchid rotor relative length L/R_2 is half of that of T-100 rotor.

To summarise, the operating conditions at the stator are very different between cases. The overall meridional gas-path *relative dimensions* are similar, except for ORCHID being 0.5 times *shorter*, the meridional gas-path shape is very different (Figure 4.45), and the metal blade angle at the inlet of the rotor differs on 40° (Figure 4.44). Due to this, differences might be expected at the inducer region of the rotor and in the development of the flow structures through the passage. Also, the higher loading and flow coefficients makes ORCHID more aerodynamically compromised. However, the exducer region of both turbines is comparable in terms of hub to tip ratio, what allows the usage of an equivalent diffuser.

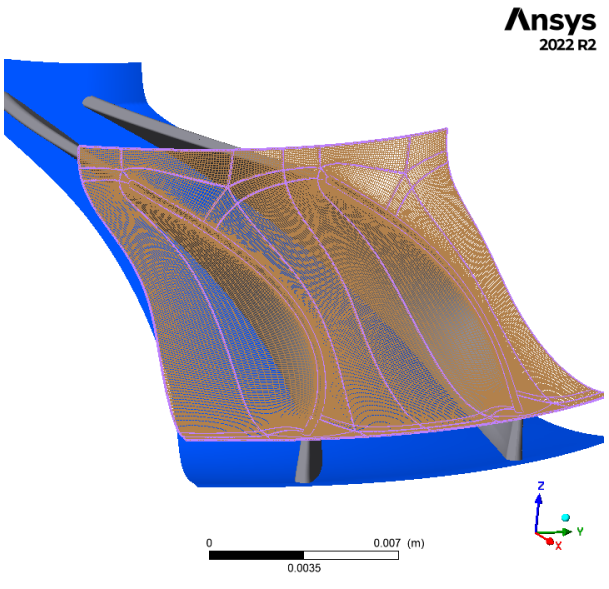

a) Rotor topology. View radially in from the inlet.

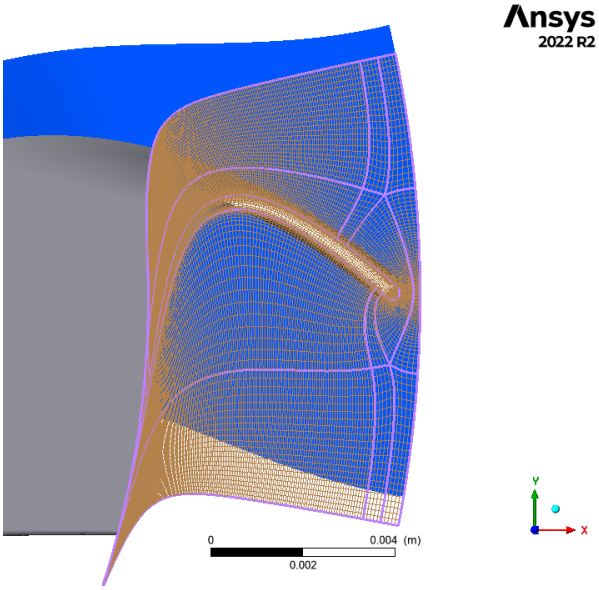

b) Rotor topology. Axial view from the outlet, detail of the leading edge.

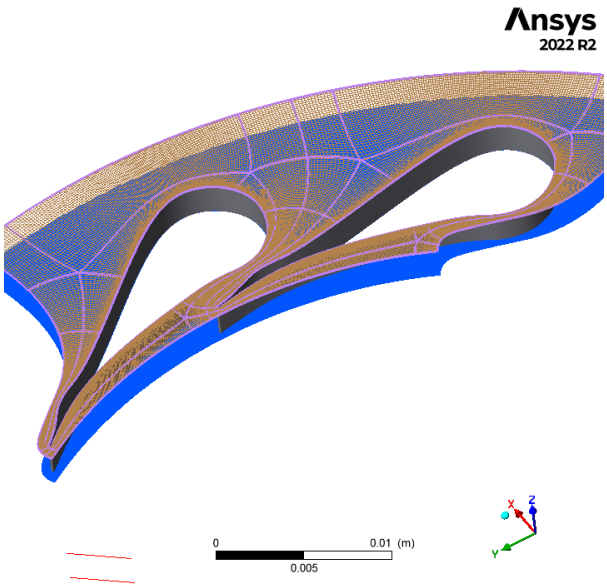

c) Stator topology.

Figure 4.43: Details of the structured computational grid for the turbine. **Stator:** 1.44 million nodes; **Rotor:** 1.74 million nodes.

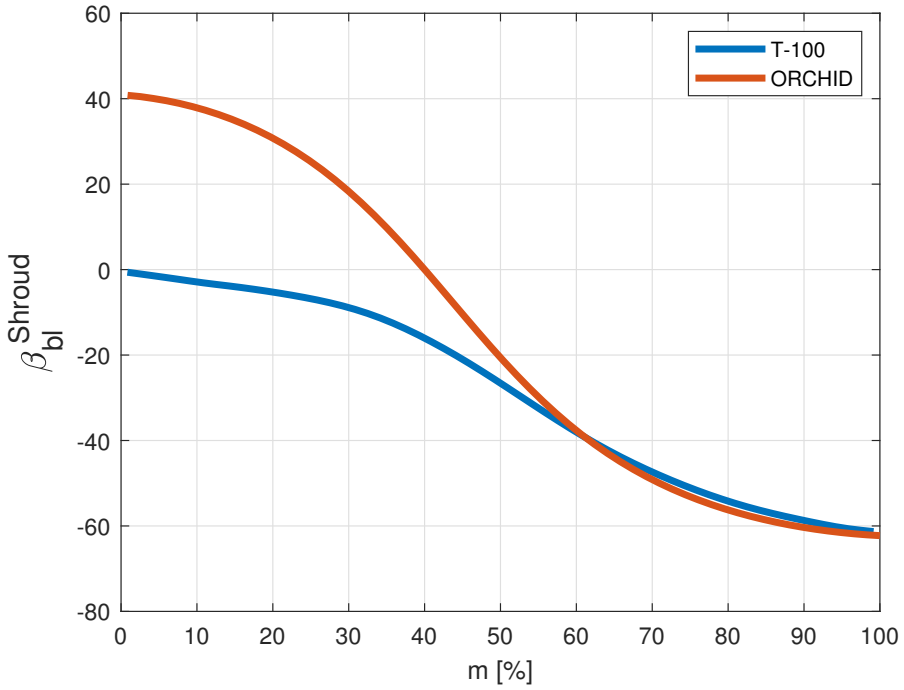

Figure 4.44: Difference in blade metal angle at the shroud between T-100 and ORCHID turbines

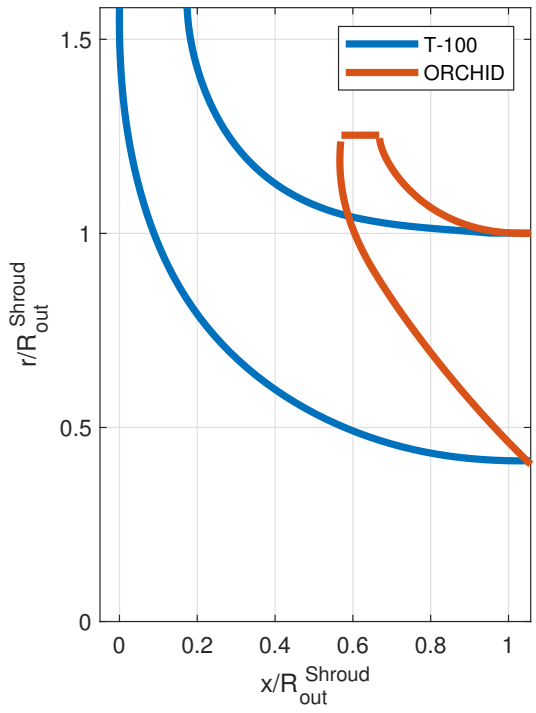

Figure 4.45: Difference in meridional gas path between T-100 and ORCHID. Rescaled in terms of $\frac{l}{R_{out}^{Shroud}}$, where l is any length.

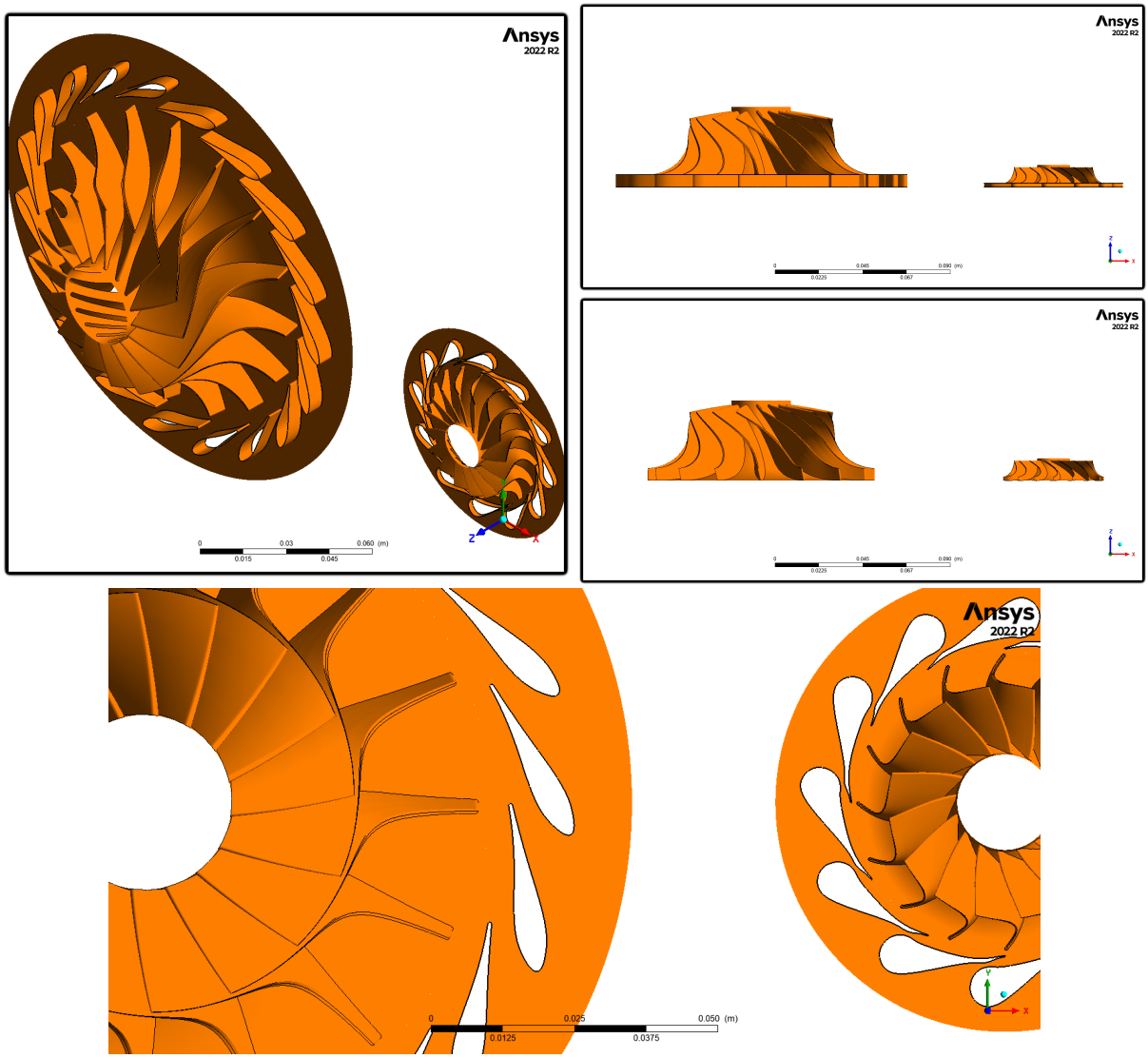

Figure 4.46: Qualitative comparison of T-100 (left) and ORCHID (right) turbines.

4.5.4. ORCHID results

Characterization of tip gaps

Different tip gap sizes and distributions where tested in order to provide an analogous study to the one presented in Chapter 4. The average tip gaps tested were: $0\ mm$, $0.045\ mm$, $0.090\ mm$, $0.12\ mm$, $0.2\ mm$, and $0.36\ mm$; and the distributions $\Delta_\epsilon = -50,\ 0,\ \&\ +50\ \%\epsilon_{Avr}$. These values were chosen to offer similar λ parameters as the ones tested previously, Figure 4.47. Note that the first 3 are not feasible configurations [52]. However, these configurations were tested to obtain a comparable data set to the T-100 case in non-dimensional (λ) terms. Comparing Figure 4.16 and Figure 4.47 it is possible to see the influence of thickness distribution in this parameter. Note that ORCHID turbine has uniform thickness blades ($0.3\ mm$). The λ with best performance in the T-100 case corresponds to a tip gap between $0.09\ mm$ and $0.12\ mm$ in ORCHID, depending on the streamwise location. This is $\epsilon_{Avr} \approx 1.41\%\overline{h}$.

Both turbines has the same number of blades, but the higher work coefficient ψ of ORCHID implies more loaded blades. This is visible in the distribution of R, Figure 4.48. In the new test case the pressure loading overcomes scraping along 80% of the passage, and the maximum value of R is three times that of T-100. It is interesting to note how this parameter is almost constant for the first half of the passage: as the blade loading increases, the blade angle decreases. This balances these two effects over a longer section than in the previous case, Figure 4.15. Lastly, note that every curve is overlapping, what suggests that the tip gap ratio has relatively low impact on blade loading close to the shroud. This was not the case for the T-100 rotor.

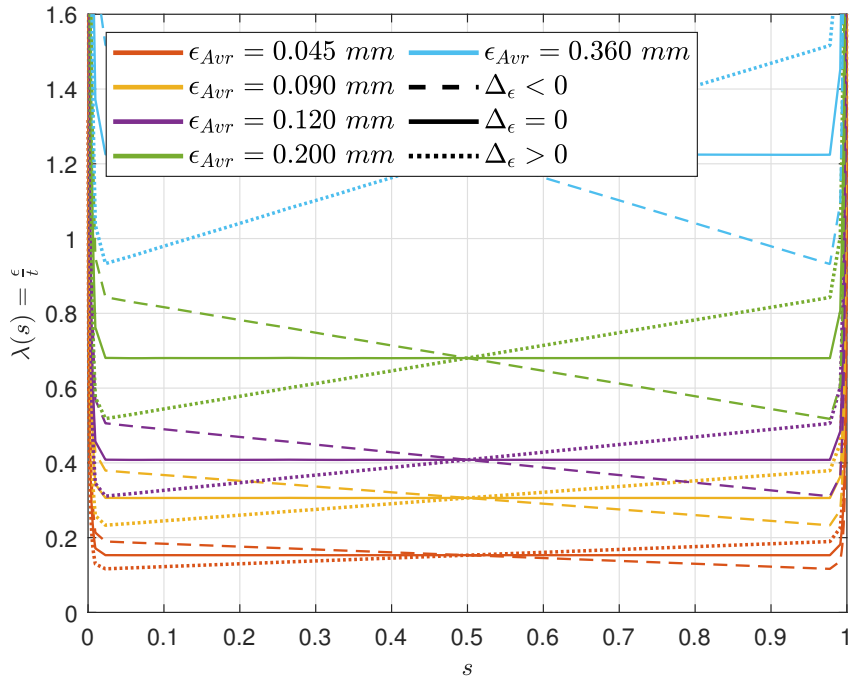

Figure 4.47: Parameter $\lambda = \frac{\epsilon}{t}$ described in [33] and Section 2.2.3 for ORCHID turbine.

Diffuser integral performance metrics

Figure 4.50 shows the total to static efficiency of the system (η_{ts}^{Sys}) and the total to total efficiency of the turbine (η_{tt}^{T}). The trends are quite different to the ones obtained for T-100 turbine (Figure 4.6 and 4.7). η_{ts}^{Sys} decreases with bigger ϵ_{Avr}, but now it is more sensitive to trailing edge gap size, ϵ_{TE}. There is a region for very small tip gaps where the work extraction of the system is practically independent of leading edge gap size, ϵ_{LE}. The evolution of η_{tt}^{T} is very different to the T-100 one, and again it is more sensitive to trailing edge gaps. This behaviour is more aligned with the common believe of ϵ_{LE} being less influential due to the partial tip gap sealing due to scraping flow. Note that the leakage flow conserves streamwise momentum and thus it is not perfectly perpendicular to the blade [32]. This implies that the positive β_{bl} at

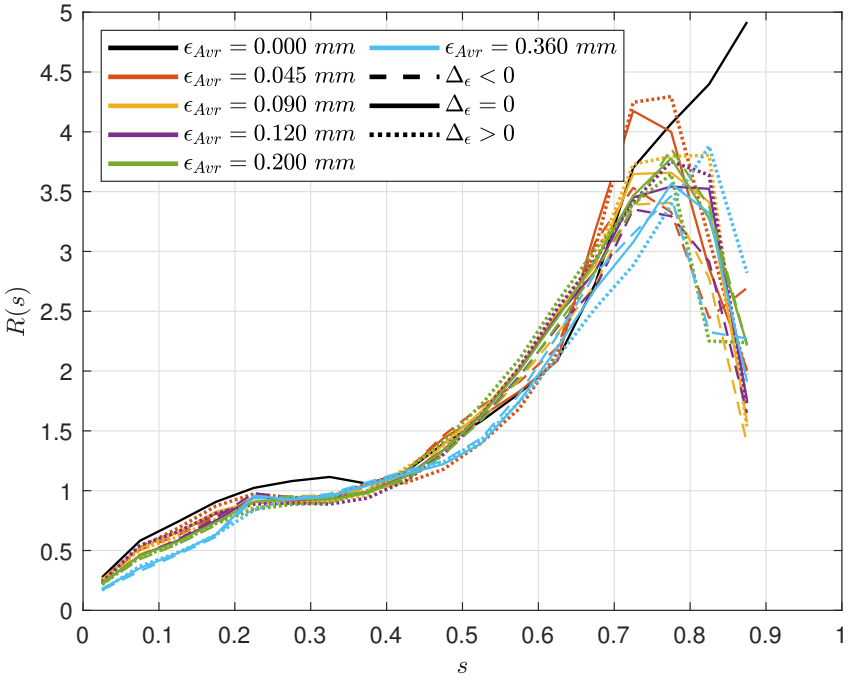

Figure 4.48: Parameter $R = \frac{\Delta P}{\frac{1}{2}\rho U^2 \cos^2(\gamma)}$ described in [33] and Section 2.2.3 for ORCHID turbine.

ORCHID inducer (Figure 4.44) actually makes scraping velocity *more orthogonal* to leakage blow, and it might increase its sealing capabilities. This behaviour is not included in the definition of the R parameter [33]. Lastly, note that the decrement in η_{ts}^{Sys} is always bigger than the one in η_{tt}^{T}: the interaction between turbine and diffuser always decreases diffuser enhancement for bigger tip gaps.

Diffuser performance metrics are shown in Figure 4.49. The highest C_p (0.66) is 0.02 points greater than the best result for T-100 turbine, and the lowest C_p is 0.2 points smaller. In the ORCHID test case, C_p mainly depends on ϵ_{Avr} and the distribution of tip gap is less important. Nonetheless, the best performance is found in the same location as before: $\lambda_{Avr} \approx 0.45$ ($\epsilon_{Avr} \approx 1.4\%\overline{h}$ for ORCHID) with *streamwise increasing* tip gaps. This points out the importance of λ. The value of K_{loss} is 3 times higher than in the $T-100$ case, but it shows the same morphology. The peculiarities of C_p are related to the kinetic energy term, ξ, as in the previous case.

Figure 4.51 shows the changes in ξ_{bulk} and ξ_{NU}. Recall $C_p = -(\Delta\xi_{bulk} + \Delta\xi_{NU}) - k_{loss}$. These values were computed with the same fluid tables as Ansys used to solve the Navies-Stokes equations. The bulk kinetic energy dissipates in the same way as in the T-100 case, Figure 4.10. Nonetheless, this effect in ORCHID is smaller and shows a stronger dependency on ϵ_{TE}. The effect of non-uniformities is greater than in T-100 and it always recovers static pressure. For very small tip gaps the strong dependency on gap size streamwise distribution is recovered, but this region is smaller and less influential.

Finally, Figure 4.52 shows the changes in M_5 with different tip gap configurations. As before, it increases with ϵ_{Avr}. However, now it is not symmetrical with respect to Δ_ϵ for big tip gaps. For a given average size ϵ_{TE} increases more M_5. M_5 is proportional to the kinetic energy at the outlet, and thus to non-uniformities (Section 2.1). This implies that in the ORCHID turbine the effect of the trailing edge gap is greater and it produces more flow-path blockage. This did not happen in the T-100 rotor.

Distribution of C_p along the diffuser

Figure 4.53 shows the distribution of C_p along the diffuser. The black solid line $C_p(x)$ for the zero tip gap case including scraping, and the dotted black line is for the shrouded rotor. Configurations with tip gaps recover pressure faster, and up to $\epsilon_{Avr} = 0.2\ mm$ the dependency on tip gap distribution is small. The biggest tip gaps tested show the behaviour of a stalled diffuser. This is clearly visible in the plot on the right.

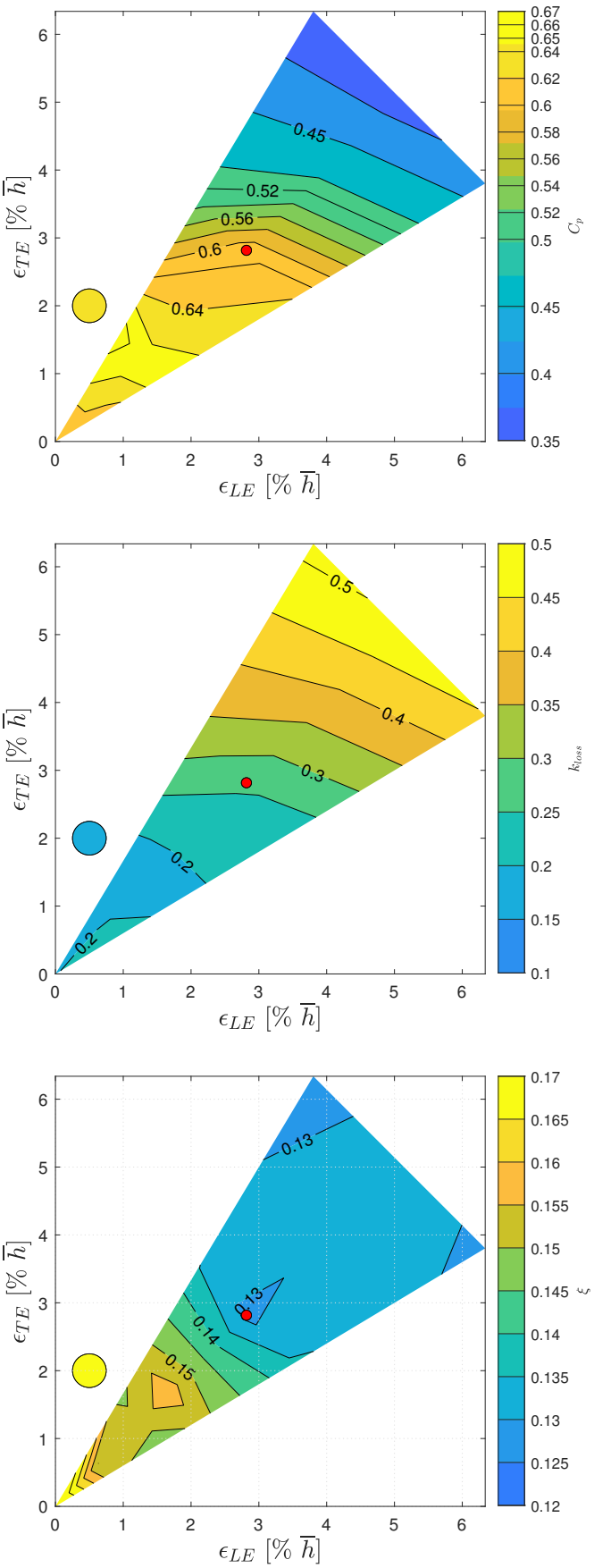

Figure 4.49: Diffuser performance metrics evaluated at the outlet for different tip gap configurations in the ORCCHID turbine. From top to bottom: C_p, k_{loss} and ξ. The red dot is the nominal configuration ($\epsilon = 0.2\ mm$), and the colored dot represents the shrouded rotor performance.

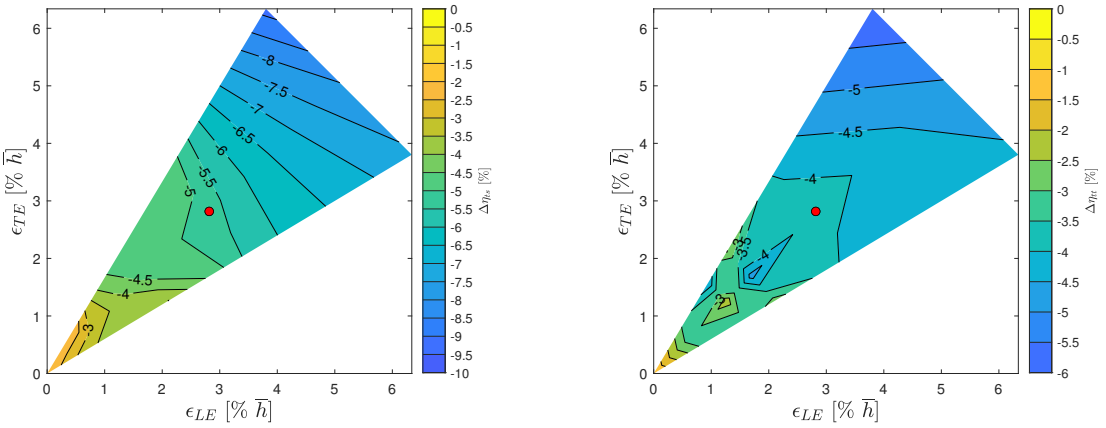

Figure 4.50: η_{ts}^{Sys} (left) and η_{tt}^{T} (right) for different tip gap configurations in the ORCHID turbine. Percentage computed with respect to a shrouded rotor. The red dot is the nominal configuration ($\epsilon = 0.2\ mm$)

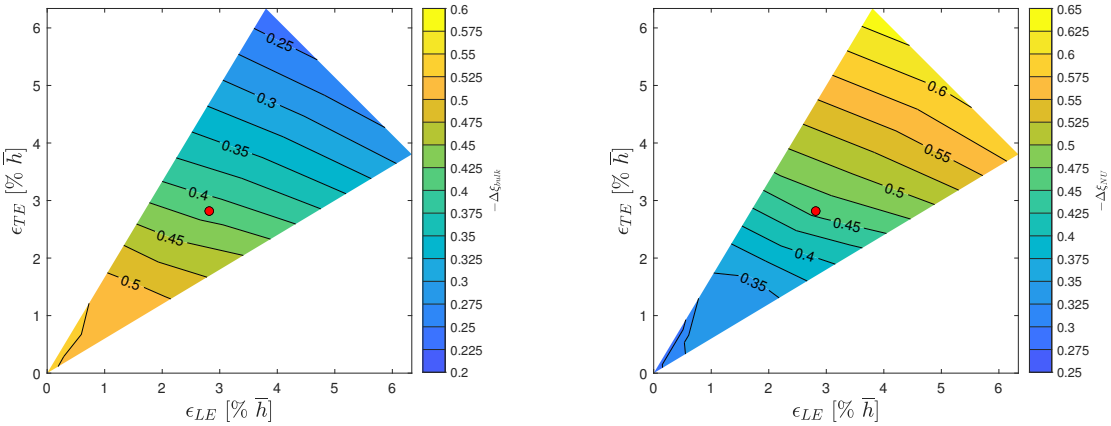

Figure 4.51: Split of ξ for the ORCHID test case: $-\Delta\xi_{bulk}$ (left) & $-\Delta\xi_{NU}$ (right). $C_p = -(\Delta\xi_{bulk} + \Delta\xi_{NU}) - k_{loss}$.

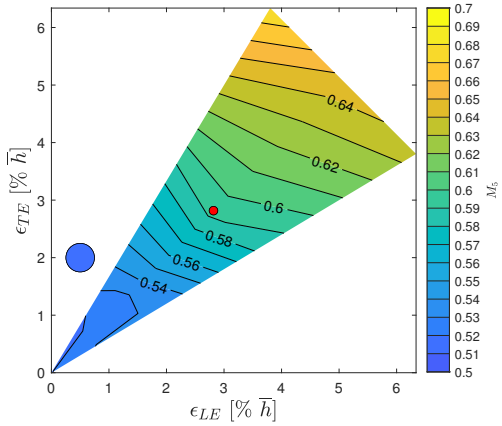

Figure 4.52: Mass flow averaged mach number at the inlet of the diffuser, $\overline{M_5}$.

The spinner recirculating bubble separation and reattachment points are shown by the inflexion points in these curves. However, the biggest tip gap configurations never manage to close the spinner wake and thus the pressure recovery is lower. Note that this involves *losses* and not only blockage: it is not possible to recover this pressure even if the bubble closes further downstream.

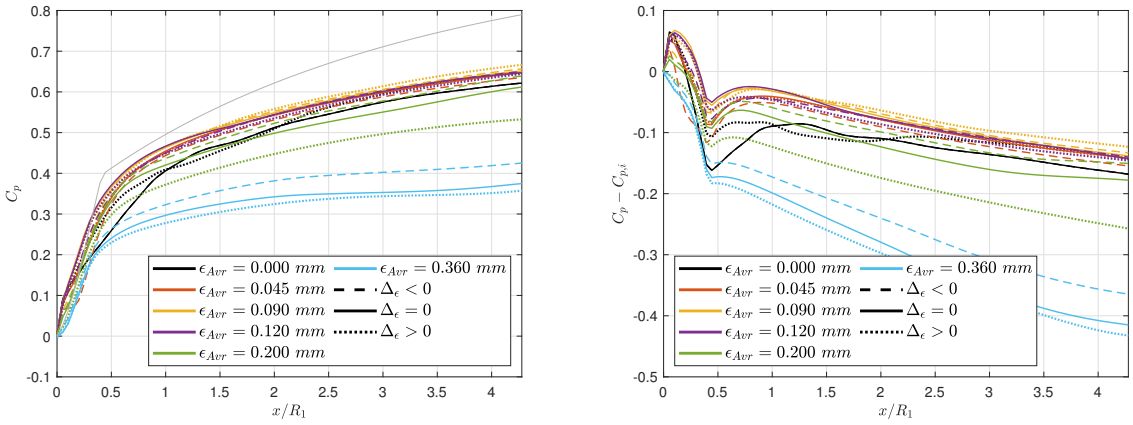

a) $C_p\,(x/R_1)$ **b)** $C_p - C_{p,i}$

Figure 4.53: Evolution of pressure coefficient C_p along the diffuser for different tip gap configurations in the ORCHID turbine.

Rotor flow structures

In order to understand the origin of these discrepancies and also test the generality of the previously discussed RIT flow structures (Section 4.3), the flow-field of the ORCHID turbine is analysed. This is done through the *helicity* field (Figure 4.54, 4.55 and 4.56); the streamlines emanating from the tip gaps (Figure 4.57, 4.58 and 4.59); and the *entropy* field (Figure 4.60, 4.61 and 4.62). The first two plots en every field are the zero tip gap configurations. For the consecutive images the left column is *streamwise decreasing* gaps and the right one is *streamwise increasing* gaps. Furthermore, each plot shows three blades with 10 secondary plane instances. The last instance only shows one passage, and the penultimate one shows two passages. All the views are close to axial, from the outlet towards the inlet of the device, and the suction side of the blades is visible.

Figure 4.54, 4.55 and 4.56 show the helicity field. Red regions represent strong streamwise vorticity directed *downstream*, whereas blue regions are strong streamwise vorticity directed *upstream*. The reader is invited to compare these plots with the streamlines in the following pages to follow where the flow is coming from. The shrouded rotor case already shows bigger and stronger flow structures than the T-100 case, what indicates that the differences in streamline curvature are important. ORCHID turbine is smaller and with a more aggressive design, so this is not surprising. When scraping is added, the *downstream* vortex related to blade boundary layer cross-flow breaks and migrates towards the middle of the channel. In the zero tip gap T-100 case the scraping vortex is always over the blade secondary flow, keeping it away from the diffuser wall. However, in the ORCHID case the scraping flow is stronger and part of the low energy flow from the blade boundary layer is displaced towards the middle of the channel. This behaviour is new and it might be related to the combination of higher blade loading and different flow-path shape. More research is needed on this topic.

The following plots are configurations with non-zero tip gaps. At the inducer region the flow is very similar to that of the T-100 rotor, with scraping flow pushing the leakage vortex towards the mid-span of the blade suction side. This flow structure is constituted by the *scraping vortex*, label **C**, and the *original tip gap vortex*, label **A**. At some point the *scraping vortex*, **C**, breaks the connection between tip gap flow and the *original tip gap vortex*, **A**, and the later is pushed away from the blade. This low energy flow migrates towards the casing around the scraping vortex while a *second tip gap vortex*, label **B**, develops in the shroud-suction side corner. The final structure is constituted by the *upstream* scraping vortex (**C**), and two *downstream* leakage vortex (**A** and **B**). The original one has migrated towards the middle-shroud region of the passage, whereas the second one is confined close to the suction-side casing corner. It is the breaking

of the leakage vortex what differentiates this structure from the counter-rotating pair observed in the T-100 rotor[7]. Note that, in ORCHID, R (Figure 4.48) grows quicker, reaching $R = 1$ for $s = 0.2$, while T-100 rotor needs $s = 0.3 - 0.4$. Also, the ORCHID rotor stays around $R \approx 1$ between $s = 0.2$ and $s = 0.4$, while T-100 continuously increases until its maximum. This implies that the T-100 rotor is continuously increasing relative pressure loading across the tip gap, while with the ORCHID design scraping effects build up without increasing ΔP. This might be the cause of the leakage vortex breaking up: the accumulation of scraping flow.

The biggest tip gaps, Figure 4.56, show a behaviour similar to T-100 with big ϵ_{Avr}. A strong isolated tip leakage vortex (label **A**) dominates the shroud region and the scraping vortex (label **C**) is convected around it. Both vortexes are located roughly at the same radial position and close to the wall. There is also a *downstream* vortex component at the middle of the passage, label **D**. The streamline plots (Figure 4.57, 4.58 and 4.59) show that is exists for every tip gap size and it is flow coming from the inducer tip gap region.

The mid-size gaps (Figure 4.55) show a smooth transition between these two flow regimens. The bigger ϵ_{Avr} is, the later the *original tip gap vortex*, **A**, split occurs, and thus the original tip leakage vortex (**A**) is stronger and closer to the second one (**B**). It is in these configurations where the *downstream* vortex casted at the inducer, label **D**, is the strongest. Note that the change in flow regime both for ORCHID and T-100 happens for the same $\lambda_{Avr} \approx 0.4$, even tough the flow structures are different. The tip gap size distribution affects more the small and medium gaps, and the leakage vortex for *streamwise increasing* gaps breaks up before and thus it appears further away from the blade. This supports the hypothesis that it is the accumulation of scraping flow what breaks this structure, as the effect occurs earlier if scraping builds up due to small leading edge tip gaps.

Finally, the entropy field is shown in Figure 4.60, 4.61 and 4.62. The leakage flow is seen as high entropy regions, labels **A** and **B**. For small tip gaps it is easy to see how the high entropy region moves around a lower entropy pocket (the scraping flow, label **C**); and how a new leakage vortex is casted. The high entropy related to the *downstream* inducer vortex diffuses along the passage and it is difficult to track except for very big tip gaps. Note that the maximum value of entropy is achieved at the inducer for small ϵ_{Avr}, so it can be concluded that it is related to the interaction of scraping and leakage flow. Lastly, even the smallest tip gap shows an *isentropic jet* at the intake region, what is another proof that a single universal value of λ^* [38] might not exist.

The differences between the ORCHID rotor and T-100 rotor flowfields are:

- For small tip gaps, the counter-rotating pair is substituted by one *upstream* scraping vortex (**C**) and two *downstream* leakage vortex. One of these is bellow the scraping vortex and towards the pressure side (**A**), and the second remains close to the wall (**B**).
- As ϵ_{Avr} increases, the leakage vortex divides sooner. The second leakage vortex (**B**) grows and the original one (**A**) is closer to it. There is a point where they do not split anymore and there is a single tip gap vortex (**A**).
- All ORCHID flow-fields for small and medium tip gaps are similar to those of medium size gaps for T-100.
- The ORCHID rotor generates a *downstream* vortex related to inducer tip leakage flow (**D**) not observed in the T-100 case. Its influence is unknown.

[7] This flow structure is similar to the one obtained for tip gaps around $\lambda \approx 0.5$ in the T-100 rotor, Figure 4.22.

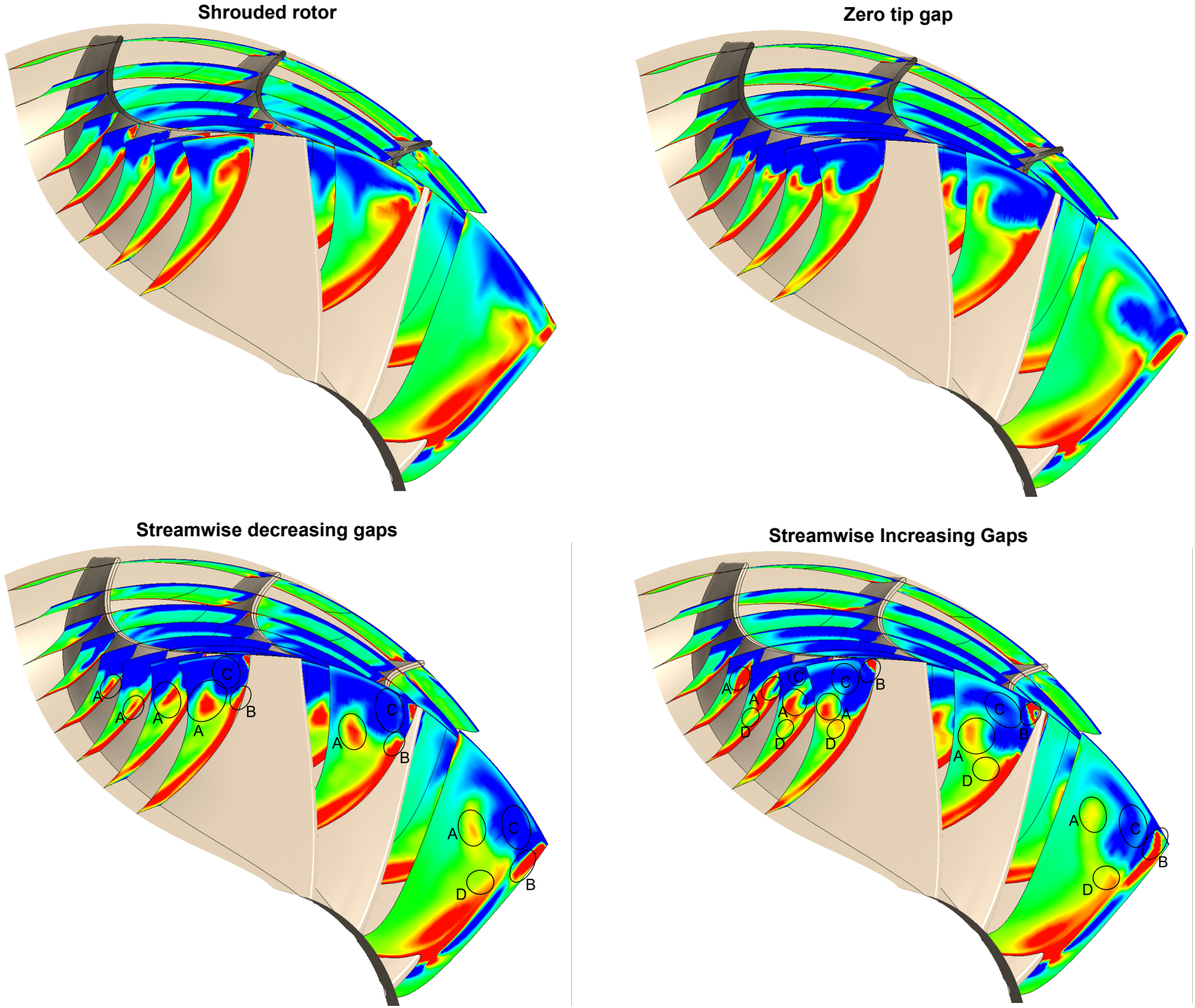

Figure 4.54: Streamwise vorticity field for the ORCHID rotor ($\frac{\vec{\omega}\cdot\vec{v}}{|\vec{v}|}$) (min: $-100000\ s^{-1}$, max: $100000\ s^{-1}$). Second Row: $\epsilon_{Avr} = 0.045\ mm$.

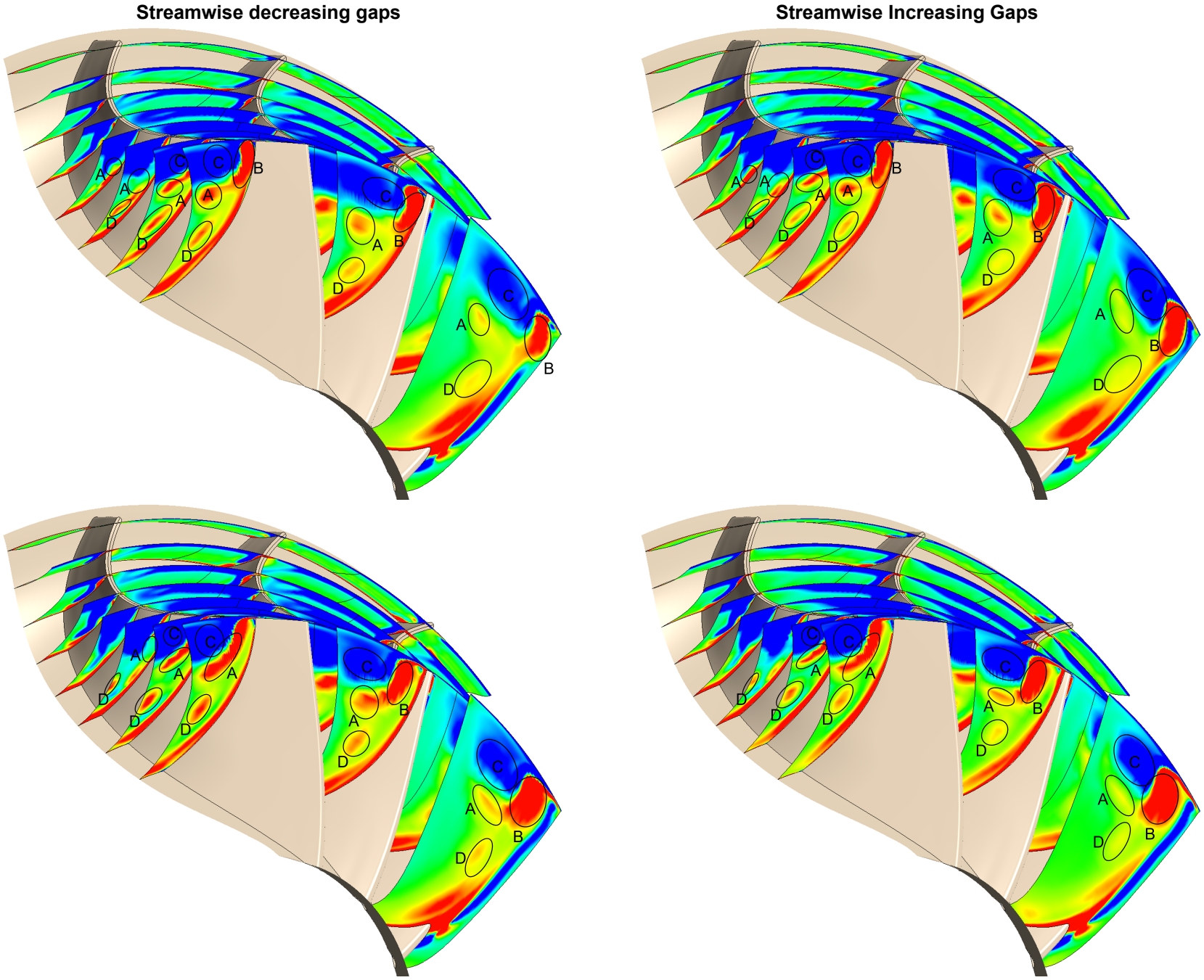

Figure 4.55: Streamwise vorticity field for the ORCHID rotor ($\frac{\vec{\omega}\cdot\vec{v}}{|\vec{v}|}$) (min: $-100000\ s^{-1}$, max: $100000\ s^{-1}$). First row: $\epsilon_{Avr} = 0.090\ mm$; Second Row: $\epsilon_{Avr} = 0.120\ mm$.

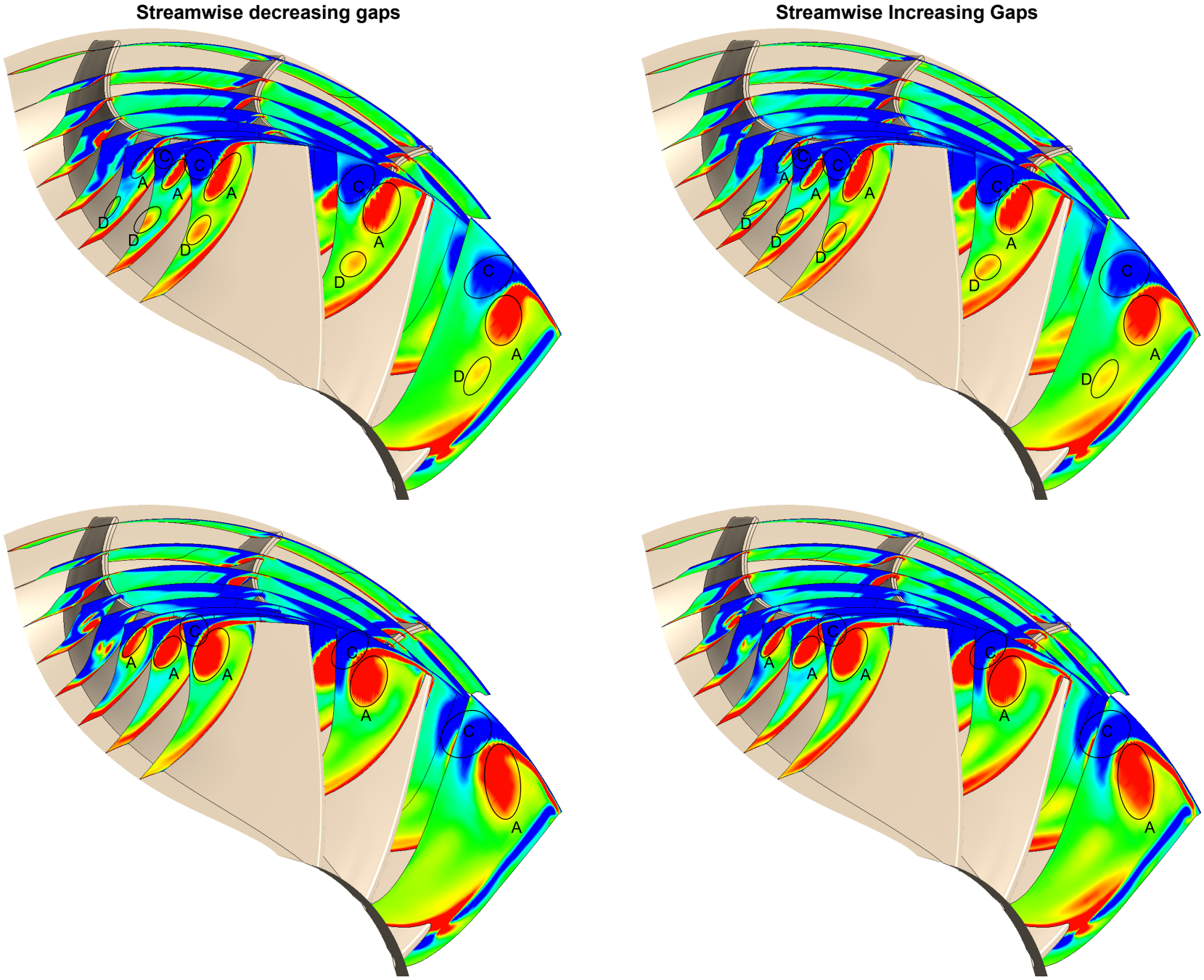

Figure 4.56: Streamwise vorticity field for the ORCHID rotor ($\frac{\vec{\omega}\cdot\vec{v}}{|\vec{v}|}$) (min: $-100000\ s^{-1}$, max: $100000\ s^{-1}$). First row: $\epsilon_{Avr} = 0.200\ mm$; Second Row: $\epsilon_{Avr} = 0.360\ mm$.

Figure 4.57: Streamlines emanating from the ORCHID tip gap cavity. Black regions are *upstream* vortexes and white regions are *streamwise* vortexes. Second Row: $\epsilon_{Avr} = 0.045\ mm$.

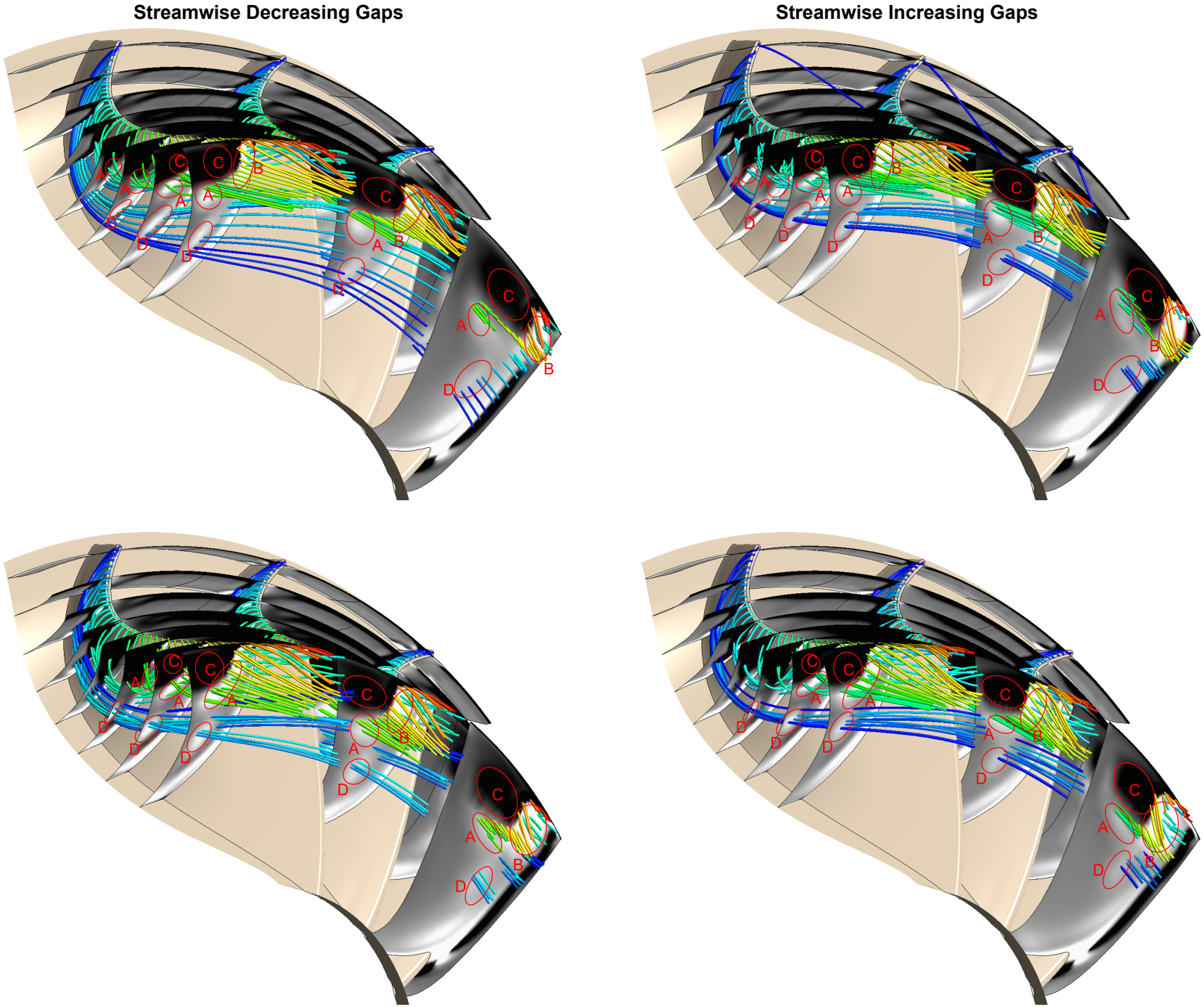

Figure 4.58: Streamlines emanating from the ORCHID tip gap cavity. Black regions are *upstream* vortexes and white regions are *streamwise* vortexes. First row: $\epsilon_{Avr} = 0.090\ mm$; Second Row: $\epsilon_{Avr} = 0.120\ mm$.

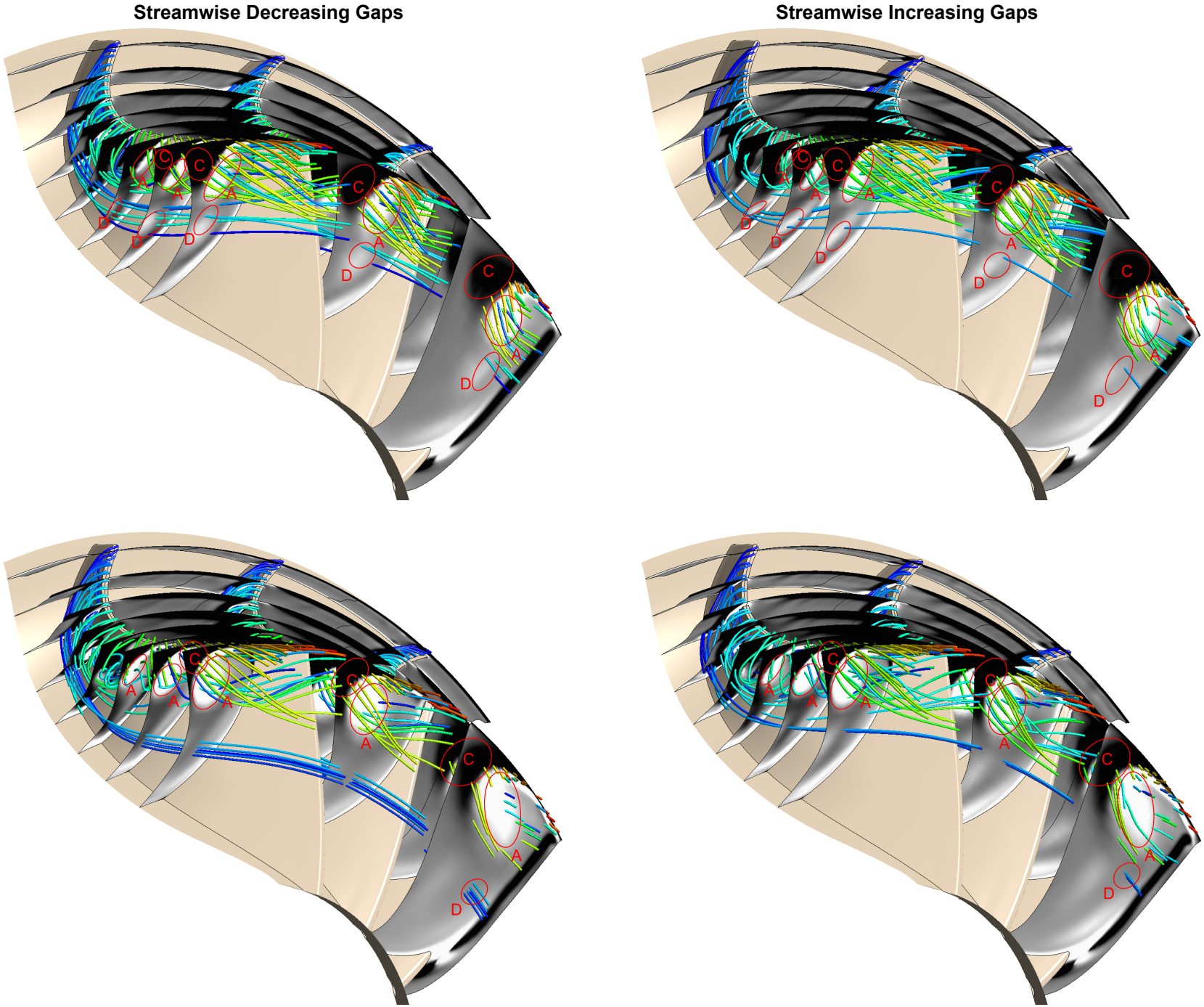

Figure 4.59: Streamlines emanating from the ORCHID tip gap cavity. Black regions are *upstream* vortexes and white regions are *streamwise* vortexes. First row: $\epsilon_{Avr} = 0.200\ mm$; Second Row: $\epsilon_{Avr} = 0.360\ mm$.

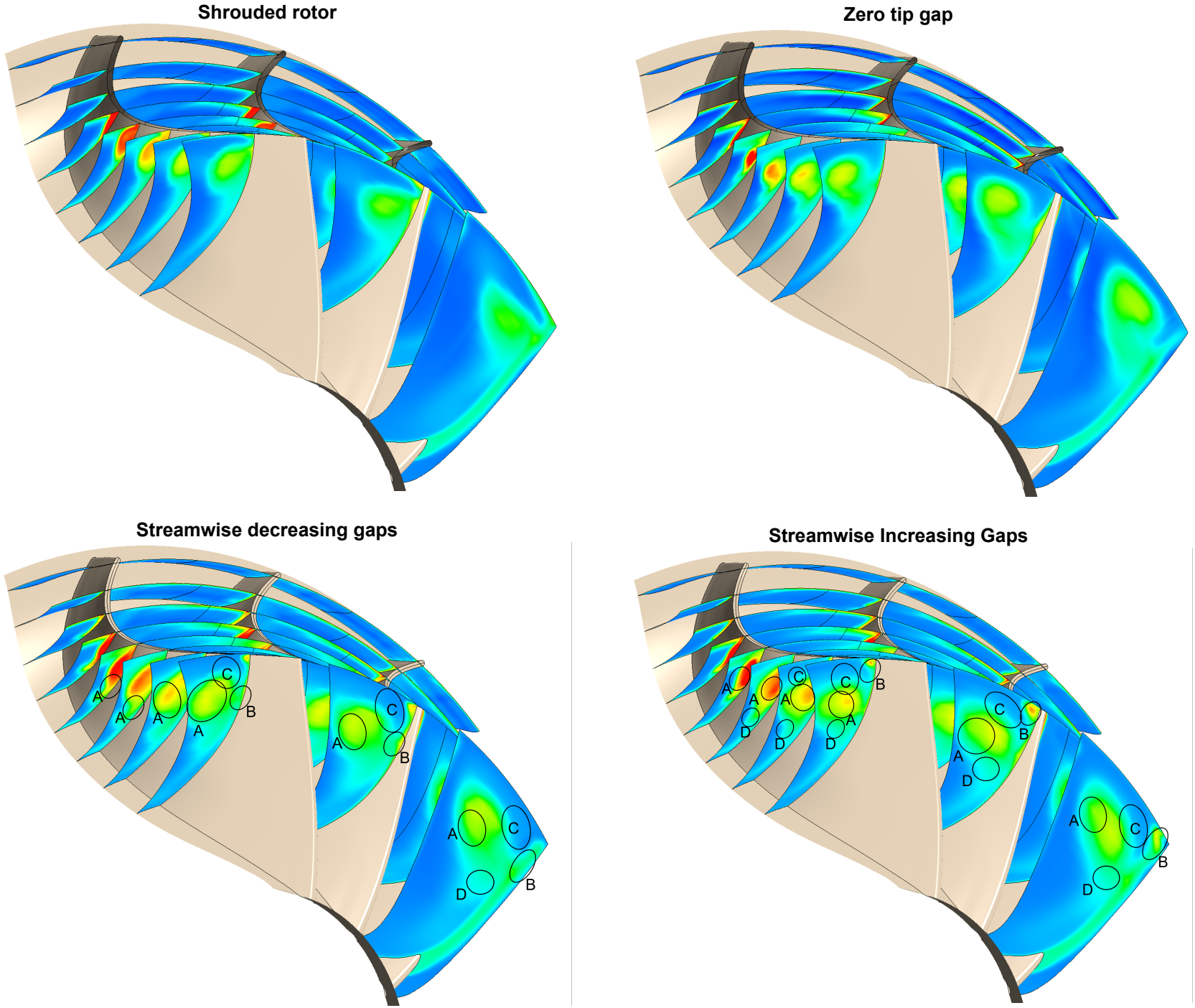

Figure 4.60: ORCHID rotor entropy field (min: $1170\ J/K$, max: $1250\ J/K$)). Second Row: $\epsilon_{Avr} = 0.045\ mm$.

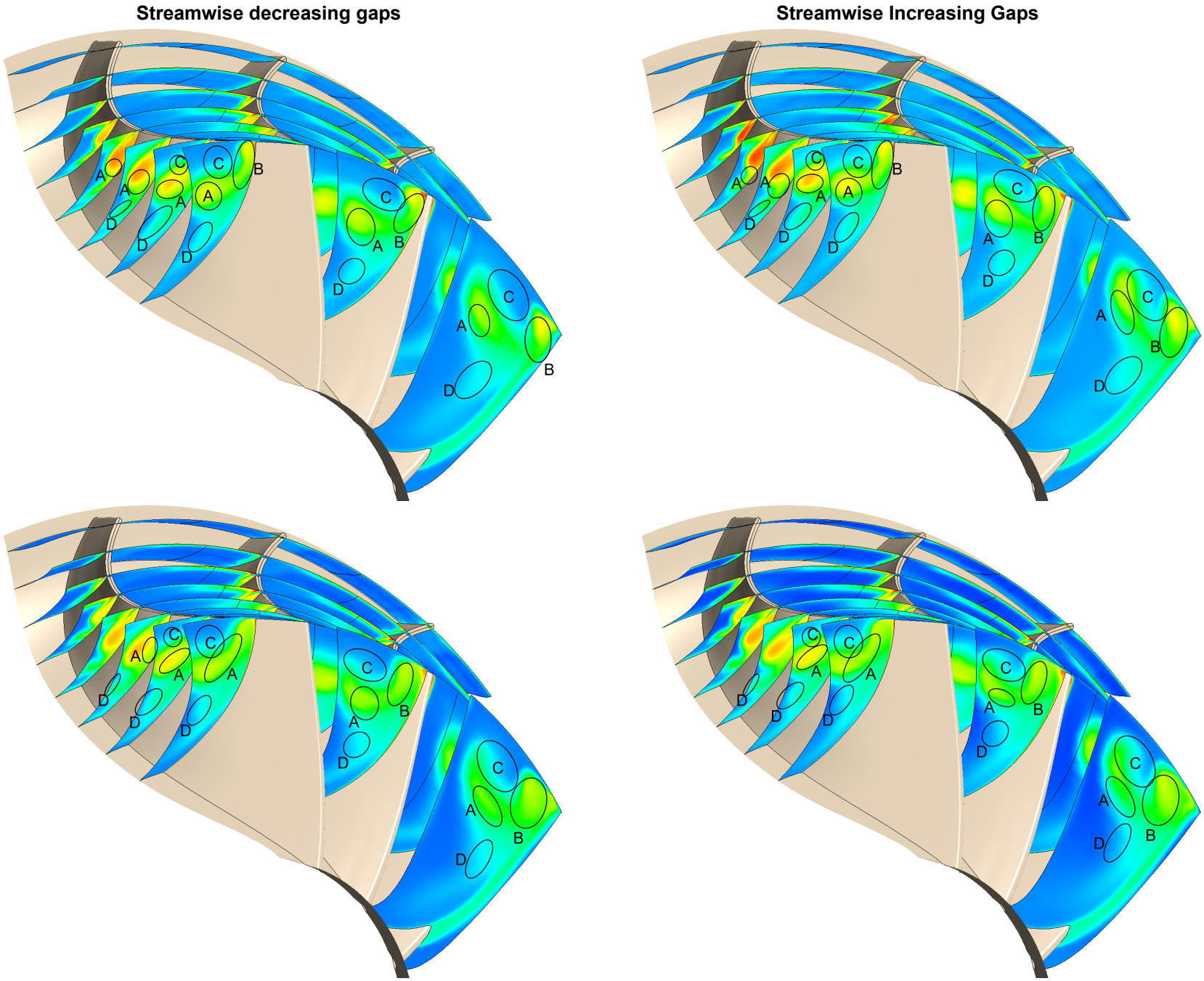

Figure 4.61: ORCHID rotor entropy field (min: $1170\ J/K$, max: $1250\ J/K$)). First row: $\epsilon_{Avr} = 0.090\ mm$; Second Row: $\epsilon_{Avr} = 0.120\ mm$.

Figure 4.62: ORCHID rotor entropy field (min: $1170\ J/K$, max: $1250\ J/K$)). First row: $\epsilon_{Avr} = 0.200\ mm$; Second Row: $\epsilon_{Avr} = 0.360\ mm$.

Diffuser flow structures

Figure 4.63 shows a meridional view of different diffuser flowfields. Each column is a different property, and moving down rows is increasing ϵ_{Avr}. Each plot contains $\Delta_\epsilon = +50\%$ ϵ_{Avr} at the top and $\Delta_\epsilon = -50\%$ ϵ_{Avr} at the bottom. The colormap is the same as in the rotor plots, and the limits are stated at the caption. Magenta lines in Mach plots represent isolines of $u_{axial} = 0$. Note how for the ORCHID case there is always vortical structures close to the walls: this is because of the breaking of the leakage vortex analysed previously. These structures avoid the boundary layer separation found in the T-100 diffuser, but they also diffuse in a less efficient way. Mach plots show that it is more difficult to close the wake of the spinner, and for the bigger gaps there is *wake bursting*. As ϵ_{Avr} increases, the velocity at the casing also increases. This finally results in a jet-like structure close to the diffuser casing and a lack of flow to close the spinner wake. This is also related to the radial pressure gradient due to outlet swirl, and it has been reported by another authors in experimental set-ups [5]. Relatively small differences in the rotor flow structures can completely change the diffuser state. Note that when the wake bursts it does not act as a simple flow-path blockage, but it generates a lot of losses: this situation is irreversible further downstream.

4.5.5. Concluding Remarks

It has been found that differences in stream-wise blade loading, as well as flow path curvature can change the way vorticity develops along the rotor channel and thus diffuser performance. For the ORCHID rotor, with higher blade loading and streamline curvature, the tip leakage vortex breaks into two structures, the first one representative of the T-100 case with small tip gaps, and the second one staying close to the wall. The flow structure with big tip gaps is similar in both rotor designs. This change in flow structure implies that the ORCHID diffuser always operates with vortical structures close to the wall, what keeps the boundary layer always attached. Another important parameter is *swirl*. As another authors have reported [41], excessive swirl can generate big low momentum regions at the hub area after *sudden expansions*. This is a process analogous to *wake bursting* in external aerodynamics. With big tip gaps, the ORCHID diffuser operates in this regimen and k_{loss} is very high. Based on this results and the previous literature research, the existence of vorticity close to the walls suggest that ORCHID could operate without stall with a steeper diffuser than a small ϵ_{Avr} T-100 rotor. However, the main issue for ORCHID is the spinner wake. This might be fixed by reducing outlet swirl, but more research is needed to understand this region of the flow.

Lastly, most differences between ORCHID and T-100 rotors are found at the inducer region. The very distinct diffuser operation mode confirms the hypothesis that this region is a very relevant parameter shaping the interaction between turbine and diffuser. Even tough the flow structure is not the same between rotors, it is possible to successfully apply the same concepts to both designs. Furthermore, both rotors present flow structure changes for similar λ_{Avr}.

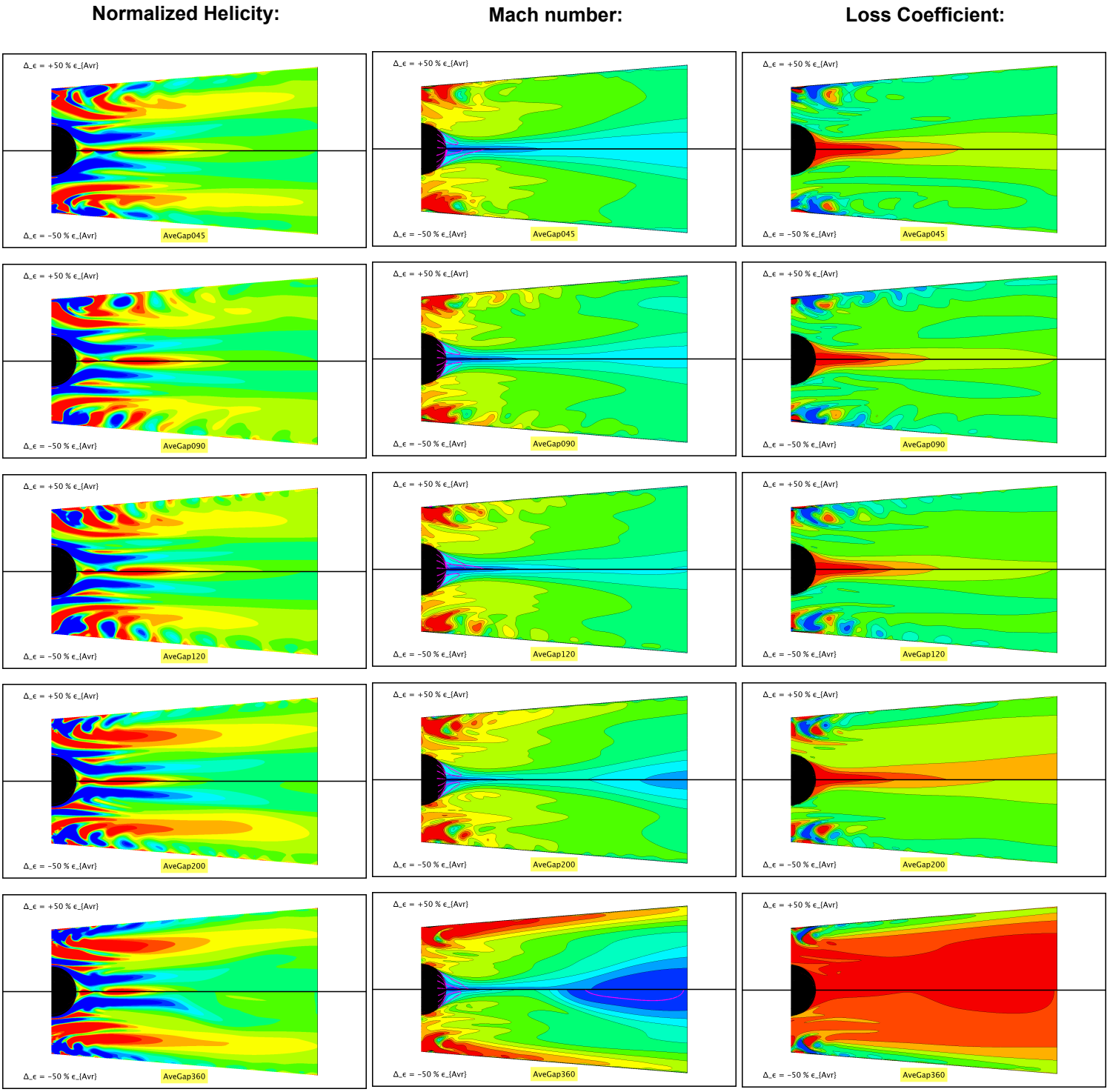

Figure 4.63: Meridional view of the ORCHID diffuser for different tip gap configurations. Helicity: $-10000\ s^{-1}$-$+10000\ s^{-1}$; Mach: 0-0.5; k_{loss}: -0.2-0.6. Each row is $\epsilon_{Avr} = 0.045$, 0.09, 0.12, 0.2, and 0.36 mm. In each diffuser, the upper half is $\Delta_\epsilon = +50\%\ \epsilon_{Avr}$ and the lower half is $\Delta_\epsilon = -50\%\ \epsilon_{Avr}$

5

Conclusion

Along this project a knowledge gap in turbine-diffuser interaction and radial inflow turbines shroud flow structures has been identified and researched. Not a lot was known about the physical mechanisms or even the parameters shaping this interaction.

The conditions under which a diffuser is the most effective have been identified as high subsonic rotor outlet Mach number, and small pressure ratios. The only diffuser parameter affecting work extraction is C_p, and the sensibility depends solely on rotor outlet Mach number. The gains due to a diffuser are smaller for high pressure ratio stages or low rotor outlet Mach numbers.

Regarding turbine diffuser interaction, it has been confirmed that **a)** rotor losses will always outweigh any diffuser enhancement for unstalled devices, and **b)** diffuser pressure coefficient, C_p, changes appreciably with different tip gap configurations. For a given diffuser, C_p can vary as much as 20%; and for a given C_p, diffuser length can vary as much as 100%. The leading edge tip gap size, ε_{LE}, has been identified as the most influential parameter, and this has been related to different flow structures in the rotor. There is an intense interaction between scraping and tip leakage flows, and it is related to tip gap parameters such as $\lambda = \frac{\epsilon}{t_{tip}}$ and $R = \frac{\Delta P}{1/2 \rho U^2 \cos^2(\gamma)}$. Different flow configurations have been studied and qualitative information about the conditions that generate them has been obtained. This work reveals the phenomenology required to develop refined tip gap leakage models predicting vortex structures, what will lead to improved diffuser design and flow control techniques.

In order to test the generality of these results, the main findings have been applied to a very different turbine design (i.e. ORCHID). The flow structures in the rotor changed notably, but the same rationale applies and no new physical mechanisms were needed to explain the flow. This confirms the validity of the previous analysis. Furthermore, the main differences, both in design and in flow structures, were found at the inducer region. This greatly changed turbine-diffuser interaction, what supports the hypothesis that this region of the rotor is the most influential one shaping the interaction. Lastly, it was found that, in the case of the ORCHID turbine, the main effect reducing diffuser performance is spinner wake bursting. This hub region is the most important to work upon if diffuser performance is to be optimised.

5.1. Research Questions: Answers

Research Question 1

What is the potential impact of a diffuser in turbine work extraction, and under which conditions is this device more relevant? (Section 2.4)

Percentage gain in energy extraction can be as high as 10% under the proper conditions. Furthermore, this enhancement is greater for small pressure ratios and high outlet Mach numbers. The work enhancement by the diffuser is independent of the total stage pressure drop, and thus it is relatively bigger for low pressure ratio machines. Furthermore, the diffuser will be more noticeable if rotor outlet Mach number, M_5, is high. Lastly, it has been proven that the only diffuser parameter affecting turbine work extraction (for a given β_{ts}^{Sys}) is the *pressure recovery coefficient*, C_p.

Research Question 2

Which is the simplest set-up able to capture realistic diffuser flow-fields and integral performance? (Section 4.1)

Along this section it has been discovered that in unstalled diffusers the static pressure trend (C_p) can be predicted with quasi-2D flows (only solving the flow in $r-x$). However, the prediction of diffuser losses, K_{loss}, requires the computation of 3D flows. This is because most of the losses are due to mixing, and these tridimensional structures dominate the mixing processes.

This implies that in the rest of the project frozen rotor interfaces will be used. This has important implications when developing low-order models for diffusers. If the losses are to be predicted in a 2D method, 3D effects must be included through some correction coefficient. Note that a 1D model will need to include the hub recirculating region as an input parameter. These results also show that simulations of isolated diffusers (both numerically and experimentally) are not fully representative of the installed operating conditions.

Research Question 3

What is the effect of tip gap size and distribution on the integral performance of the diffuser? (Section 4.2)

It has been found that different tip gap sizes and distributions affect the performance of the diffuser, changing C_p up to 20% for a given geometry, or diffuser length up to 100% for a given C_p. There is an optimal tip gap configuration. Bigger tip gaps are detrimental both to diffuser and rotor performance. Furthermore, the origin of this interaction has been traced back to the pressure recovery due to the dissipation of non-uniform flow structures. Diffuser losses depend on ϵ_{Avr}, and they are mainly driven by mixing. On the other hand, pressure recovery due to non-uniform flow depends both on gap size and distribution. Small gaps perform better, and *streamwise increasing* tip gaps yield the best pressure recovery. If a critical gap size is surpassed, the dependency on distribution is mostly lost and performance drops with ϵ_{Avr}.

It has been attempted to identify the conditions where this change in behaviour occurs by means of tip gap characteristic parameters, as λ and R. No general quantitative trend was found, but lower R parameter requires higher λ to yield the same diffuser integral behaviour. Furthermore, the data obtained shows that it is unlikely to find an universal λ^* value to characterise the tip gap cavity flow, as this also depends on scraping [33].

Finally, it has been also shown than an increment in tip gap size will always reduce power extraction. However, if the design team is given a choice between reducing axial or radial gap, diffuser interaction criteria says that they should reduce the axial (leading edge) one, even at the cost of small increases in the another one.

Research Question 4

What is the physical interaction mechanism between turbine and diffuser? (Section 4.3)

Three kinds of flow modes have been identified depending on tip gap size and distribution. For small gaps two counter-rotating vortexes leave the turbine, located approximately one vortex diameter bellow the casing. This generates a low loss region close to the diffuser wall that avoids the stalling found in shrouded rotors. For the biggest tip gaps, there is only one isolated vortex associated to tip gap leakage, and the scraping flow is convected around it. For medium tip gaps, a gradual mixture between the two flow structures is found. Maximum diffuser performance is obtained when the pair of vortexes is the strongest possible before casting a big isolated vortex, whereas worst diffuser performance is obtained when a strong isolated vortex coexists with the counter-rotating pair. Furthermore, it has been discovered that the value of λ^* that changes performance is the one where the isentropic jet is strong enough as to overcome the scraping flow, and not the one when it appears for the first time.

The disipation of all vortical structures generates a static pressure rise. The isolated vortex generates high mixing losses when dissipating in the diffuser. However, the counter-rotating pair generates lower losses than the isolated vortex. It is the dissipation of these vortexes what drives turbine-diffuser interaction, and the counter-rotating vortex is more efficient in doing this. Furthermore, the scraping vortex in the case of big tip gaps is convected close to the diffuser wall, while for small tip gaps it stays at the centre. This implies that, even though the structures for small tip gaps are more *effective*, they might not be as good as the others in avoiding boundary layer separation. More research is needed in this topic.

Finally, the greater influence of the leading edge tip gap is explained by the higher scraping in this region. The structures casted at the inducer region can leave the rotor, and they affect the evolution of all the shroud processes further downstream along the rotor.

5.2. Future Work

Along the project further knowledge gaps have been found. They are stated here as recommendations for future research.

- **Rotor outlet hub region:** the biggest entropy generation in the diffuser is due to the recirculating region in the separated flow at the hub. It has been shown theoretically and in practise that diffuser losses do not directly affect total to static efficiency. However, as the ORCHID test case showed, the wake of the spinner can be problematic and great diffuser performance improvements can be achieved by controlling the separation bubble.
- **Characterization of tip gap cavity flows for radial machines**: It has been found that the tip gap leakage can result in different flow structures, and which one is generated seems to be related to tip gap parameters such as R and λ. However, it was not possible to find any general trend that allows the prediction of flow regime *a priori*.
- **Detailed model of tip leakage:** There are several models for radial inflow turbine tip gap flow and leakage. However, none of them properly includes the physical phenomena at the tip gap cavity, or offer the capability to predict the size and strength of the vortex. The present work initiates the research needed to develop such a model capable to take into account scraping and tip gap geometry. Predicting vortex structure and strength is the first step towards a really coupled low order diffuser model.
- **Extension of the study to another operation points:** It is known that in off-design conditions the inducer of the rotor can stall, and this results in different vortexes being casted. In order to fully characterize turbine-diffuser interaction this new vortexes must be also included.
- **Evaluation of the unsteady case:** Given the importance of the rotor inducer region, it is fair to expect some changes when including the unsteady interaction with the stator vanes.
- **Exploration of unconventional diffusing methods:** This experience has shown that the sudden expansion reaches acceptable static pressure rises in very short distances. This opportunity might be exploited by a detailed study of the flow structures leading to the shortest sudden expansion possible, or using *vortex controlled diffusers* [54]. This topic is tightly coupled with hub spinner design.

References

[1] Sydney Lawrence Dixon et al. *Fluid mechanics and thermodynamics of turbomachinery*. Butterworth-Heinemann, 2013.

[2] Saeed Farokhi. “A trade-off study of rotor tip clearance flow in a turbine/exhaust diffuser system”. In: *Turbo Expo: Power for Land, Sea, and Air*. Vol. 79238. American Society of Mechanical Engineers. 1987, V001T01A084.

[3] Reinhard Willinger et al. *The role of rotor tip clearance on the aerodynamic interaction of a last gas turbine stage and an exhaust diffuser*. Vol. 78620. American Society of Mechanical Engineers, 1998.

[4] Olaf Sieker et al. “Effects of rotating blade wakes on separation and pressure recovery in turbine exhaust diffusers”. In: *Turbo Expo: Power for Land, Sea, and Air*. Vol. 43161. 2008, pp. 1921–1931.

[5] Olaf Sieker et al. “Influence of rotating wakes on separation in turbine exhaust diffusers”. In: *Journal of Thermal Science* 17.1 (2008), pp. 42–49.

[6] Dajan Mimic. “Phd thesis: Turbine diffuser interaction”. In: *Institutionelles Repositorium der Leibniz Universität Hannover* (2021).

[7] David Japikse et al. *Diffuser design technology(Book)*. 1998.

[8] Stephen Jay Kline et al. “Optimum design of straight-walled diffusers”. In: *Journal of Basic Engineering* 81.3 (1959), pp. 321–329.

[9] Dajan Mimic et al. “Correlation between total pressure losses of highly loaded annular diffusers and integral stage design parameters”. In: *Journal of the Global Power and Propulsion Society 2 (2018)* 2 (2018), I9AB30.

[10] Gino Sovran. “Experimentally determined optimum geometries for rectlinear diffusers with rectangular, conical or annular cross section”. In: *Fluid mechanics of internal flow* (1967), pp. 270–319.

[11] Katsuya Ishikawa et al. “Performance chart and optimum geometries of conical diffusers with uniform inlet flow and free discharge”. In: *JSME international journal. Ser. 2, Fluids engineering, heat transfer, power, combustion, thermophysical properties* 32.4 (1989), pp. 559–567.

[12] SJ Stevens et al. “The influence of inlet conditions on the performance of annular diffusers”. In: *Journal of Fluids Engineering* (1980).

[13] Y Senoo et al. “Prediction of flow separation in a diffuser by a boundary layer calculation”. In: *Transactions of the ASME* (1977).

[14] William Burns Nicoll et al. “Performance of conical diffusers with annular injection at inlet”. In: *Journal of Basic engineering* (1970).

[15] Lloyd Back et al. “Experimental investigation of turbulent walljets in the presence of adverse pressure gradients in a rectangular diffuser”. In: *International Journal of Heat and Mass Transfer* 25.6 (1982), pp. 871–887.

[16] H Kruse et al. “Experimental investigations on annular diffusers downstream of turbine stages”. In: *Motortech. Z.;(Germany, Federal Republic of)* 44.1 (1983).

[17] V Vassiliev et al. “Experimental and numerical investigation of the impact of swirl on the performance of industrial gas turbines exhaust diffusers”. In: *Turbo Expo: Power for Land, Sea, and Air*. Vol. 36894. 2003, pp. 19–29.

[18] Vladimir Vassiliev et al. “Impact of the inflow conditions on the heavy-duty gas turbine exhaust diffusers performance”. In: *Turbo Expo: Power for Land, Sea, and Air*. Vol. 44021. 2010, pp. 1401–1412.

[19] Marcus Kuschel et al. “Influence of unsteady turbine flow on the performance of an exhaust diffuser”. In: *Turbo Expo: Power for Land, Sea, and Air*. Vol. 54679. 2011, pp. 1551–1561.

[20] Dajan Mimic et al. “Correlation between pressure recovery of highly loaded annular diffusers and integral stage design parameters”. In: *Journal of Turbomachinery* 140.7 (2018).

[21] Dajan Mimic et al. “Increasing Boundary Layer Stability for Varying Degrees of Diffuser Loading”. In: *Proceedings of GPPS Forum 18*. Zug: Global Power and Propulsion Society. 2018.

[22] Gunnar Heskestad. “A suction scheme applied to flow through sudden enlargement”. In: (1968).

[23] RC Adkins. “A short diffuser with low pressure loss”. In: (1975).

[24] E Floyd Valentine et al. *Effects of Some Primary Variables of Rectangular Vortex Generators on the Static-pressure Rise Through a Short Diffuser*. Tech. rep. 1952.

[25] Alan C Brown et al. “Subsonic diffusers designed integrally with vortex generators.” In: *Journal of Aircraft* 5.3 (1968), pp. 221–229.

[26] S Grundmann et al. “Sensitivity of an asymmetric 3D diffuser to plasma-actuator induced inlet condition perturbations”. In: *Experiments in Fluids* 50.1 (2011), pp. 217–231.

[27] R Blanco et al. “Performance analysis of an axial exhaust diffuser downstream of an un-shrouded turbine”. In: *Advances in Fluid Mechanics* 10 (2014), p. 419.

[28] Edward M Greitzer et al. *Internal flow: concepts and applications*. Cambridge University Press, 2007.

[29] Chung-Hua Wu. “A general theory of three-dimensional flow in subsonic and supersonic turbomachines of axial, radial, and mixed-flow types”. In: *Transactions of the American Society of Mechanical Engineers* 74.8 (1952), pp. 1363–1380.

[30] John D Coull. “Endwall loss in turbine cascades”. In: *Journal of Turbomachinery* 139.8 (2017).

[31] M Zangeneh-Kazemi et al. “Three dimensional flow in radial-inflow turbines”. In: *Turbo Expo: Power for Land, Sea, and Air*. Vol. 79184. American Society of Mechanical Engineers. 1988, V001T01A046.

[32] R Dambach et al. “An experimental study of tip clearance flow in a radial inflow turbine”. In: *Turbo Expo: Power for Land, Sea, and Air*. Vol. 78620. American Society of Mechanical Engineers. 1998, V001T01A110.

[33] ROGER Dambach et al. “Tip leakage flow in a radial inflow turbine with varying gap height”. In: *Journal of Propulsion and Power* 17.3 (2001), pp. 644–650.

[34] Aurélien Marsan-Stéphane Moreau. “Analysis of the flow structure in a radial turbine”. In: *Proceedings of 11th European Conference on Turbomachinery Fluid dynamics & Thermodynamics* (2015).

[35] FA Lyman. “On the conservation of rothalpy in turbomachines”. In: *Transactions of the ASME* (1993).

[36] Delft High Performance Computing Centre (DHPC). *DelftBlue Supercomputer (Phase 1)*. `https://www.tudelft.nl/dhpc/ark:/44463/DelftBluePhase1`. 2022.

[37] JP Johnston. “Review: Diffuser design and performance analysis by a unified integral method.(Data Bank contribution)”. In: *J FLUIDS ENG TRANS ASME* 120.1 (1998), pp. 6–18.

[38] Juan G Bardina. “Computation of Straight Walled Diffusers at Low Mach Number Incorporating an Improved Correlation for Turbulent detachment and Reatachment.” In: (1982).

[39] V Vassiliev et al. “CFD analysis of industrial gas turbine exhaust diffusers”. In: *Turbo Expo: Power for Land, Sea, and Air*. Vol. 3610. 2002, pp. 995–1013.

[40] Dragan Kozulovic et al. “Modelling the streamline curvature effects in turbomachinery flows”. In: *Turbo Expo: Power for Land, Sea, and Air*. Vol. 4241. 2006, pp. 1239–1248.

[41] David Kluß et al. “Effect of wakes and secondary flow on re-attachment of turbine exit annular diffuser flow”. In: *Journal of Turbomachinery* (2009).

[42] A Hirshmann et al. “Influence of the Total Pressure Profile on the Performance of Axial Gas Turbine Diffuser”. In: *GT2010-22481* (2010).

[43] Marius Mihailowitsch et al. “Numerical investigations of an axial exhaust diffuser coupling the last stage of a generic gas turbine”. In: *Journal of Engineering for Gas Turbines and Power* 141.3 (2019).

[44] Simon Hummel et al. “Study of gas turbine exhaust diffuser flow and performance characteristics at off-design conditions”. In: *14 th European Conference on Turbomachinery Fluid dynamics & Thermodynamics*. EUROPEAN TURBOMACHINERY SOCIETY. 2021.

[45] Florian R Menter. “Two-equation eddy-viscosity turbulence models for engineering applications”. In: *AIAA journal* 32.8 (1994), pp. 1598–1605.

[46] NA Cumpsty et al. “Averaging non-uniform flow for a purpose”. In: *Turbo Expo: Power for Land, Sea, and Air*. Vol. 47306. 2005, pp. 1–14.

[47] AC Jones. “Design and test of a small, high pressure ratio radial turbine”. In: *Transactions of the ASME* (1996).

[48] Emilie Sauret. “Open design of high pressure ratio radial-inflow turbine for academic validation”. In: *ASME International Mechanical Engineering Congress and Exposition*. Vol. 45233. American Society of Mechanical Engineers. 2012, pp. 3183–3197.

[49] Yves Dubief et al. “On coherent-vortex identification in turbulence”. In: *Journal of turbulence* 1.1 (2000), p. 011.

[50] Sebastian Bahamonde et al. “Method for the preliminary fluid dynamic design of high-temperature mini-organic rankine cycle turbines”. In: *Journal of Engineering for Gas Turbines and Power* 139.8 (2017).

[51] Nitish Anand et al. “Design methodology for supersonic radial vanes operating in nonideal flow conditions”. In: *Journal of Engineering for Gas Turbines and Power* 141.2 (2019).

[52] Carlo M De Servi et al. “Design method and performance prediction for radial-inflow turbines of high-temperature mini-organic rankine cycle power systems”. In: *Journal of Engineering for Gas Turbines and Power* 141.9 (2019).

[53] Alessandro Cappiello et al. “On the Influence of Stator-Rotor Radial Gap Size on the Fluid-Dynamic Performance of Mini-ORC Supersonic Turbines”. In: *Turbo Expo: Power for Land, Sea, and Air*. Vol. 86106. American Society of Mechanical Engineers. 2022, V10BT35A015.

[54] D Japikse. “A new diffuser mapping technique—part 1: studies in component performance”. In: *Transactions of the ASME* (1986).

[55] Patrick J Roache. *Verification and validation in computational science and engineering*. Vol. 895. Hermosa Albuquerque, NM, 1998.

A

Grid Convergence Study

This appendix deepens in the topic of grid convergence study, used to assess the spatial discretization convergence order.

A.1. General Theory: Richardson's extrapolation

This section is based on the Richardson's extrapolation, retrieved from NASA website and based on Roche (1998, [55]). The main idea of the method is that any CFD result can be written as:

$$f = f_{h=0} + g_1 \cdot h + g_2 \cdot h^2 + g_3 \cdot h^3 + ... \tag{A.1}$$

where f can be a local property of a functional of the simulation (as turbine efficiency, η_{tt}), $f_{h=0}$ is the (unknown) exact solution for a zero spacing grid, and h is a measure of the grid spacing. Note that $h \to 0$, so the smallest non-zero addend sets the order of the method. In general:

$$f = f_{h=0} + A \cdot h^p + O(h^{p+1}) \tag{A.2}$$

Where p is the spatial order of convergence, and it might not be an integer. This order will be at most as high as the solver order, and in general it is reduced due to non-ideal grid spacings, boundary conditions, non-linearities, etc.

Calling f_j to the (computed) solution with spacing h_j, it is possible to obtain:

$$f_{h=0} = f_1 + \frac{f_1 - f_2}{\left(\frac{h_2}{h_1}\right)^p - 1} \tag{A.3}$$

which is a $p+1$ order estimator of the exact solution. Note that in general p is unknown. This estimator can be used to extrapolate values from coarse grids, or as a convergence metric. In order to get the order of convergence, it is necessary to use at least 3 different grids, obtaining:

$$\frac{f_3 - f_1}{f_1 - f_2} = \frac{h_1^p - h_3^3}{h_2^p - h_1^p} \tag{A.4}$$

In the case of uniform grid ratios, $r = \frac{h_{j+1}}{h_j} = const.$, this expression simplifies to:

$$p = \ln\left(\frac{f_3 - f_2}{f_2 - f_1}\right) / \ln(r) \tag{A.5}$$

Note that with three grids it is also obtained:

$$A = \frac{f_2 - f_1}{h_2^p - h_1^p} \tag{A.6}$$

And the line Equation A.2 can be reconstructed.

The convergence trend given in Equation A.2 is an idealized case. For very fine grids another kind of errors (round errors) can appear and the convergence order p will be reduced.

A.2. T-100 Convergence Study: details

Figure 3.8 shows the convergence of turbine total to total efficiency as a function of the number of grid nodes. This is an useful view, because it shows the real computational cost of the grid. However, it is mathematically difficult to evaluate errors based on number of nodes. Figure A.1 shows the convergence of η_{tt} against a metric of grid spacing. In this case, maximum grid spacing was chosen, and this is computed as $h_{grid}^{max} = \sqrt[3]{\max V_{cell}}$. The convergence trend parameters are computed with the 3 biggest grid spacings. Another metrics and computations were tested and this gave the best match because:

1. It is expected to find the biggest errors close to the biggest cells.
2. The bigger cells are more or less isotropic, whereas the small volume cells are in the boundary layer and they are highly skewed. These cells have a dimension way smaller than the others and thus it is not trivial to extract a length scale from them.
3. The smallest cells have the constraint $y^+ \approx 1$, so they are not refined in a isotropic manner.
4. Mean cell volume gives a lot of weight to the boundary layers, where the cell count is high. This generates the issues from the previous points.
5. Using root mean square error, $\sqrt{\frac{1}{N}\sum_j(\eta_j - \eta_{h=0})^2}$, instead of the first three points, gave a convergence order higher than the numerical scheme. The method was trying to also match the finest grids that do not follow the same trend.

Note that when obtaining this curve all three parameters $\eta_{h=0}$, A, and p are computed simultaneously.

The plot shows that the convergence order of the numerical method in this grid is $p = 1.74$, lower than the ideal 2^{nd} order but aligned with references in open literature. Also, the order of the solver is not necessarily 2^{nd} order *globally* (Section 3.3). The extrapolated value of efficiency is also reported as $\eta_{h=0} = 0.928$. Note that the convergence trend changes for smaller grids, so it is unlikely that this is the *real* value. This is a common caveat in Richardson's extrapolation.

It is thought that for smaller grids other kinds of errors start to appear in the smallest cells, and thus the convergence rate drops. Note that the selected grid is the last one in the fast convergence region: from this point on reducing grid spacing provides diminishing returns.

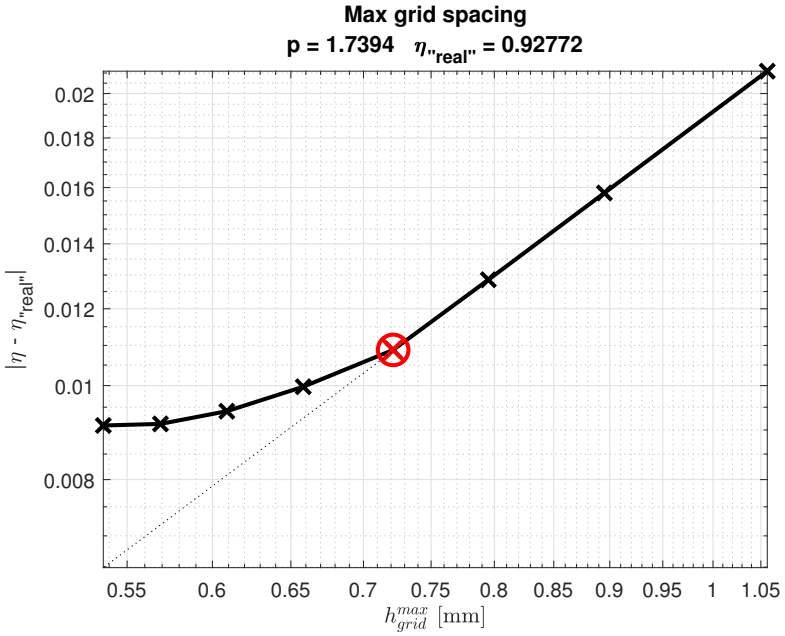

Figure A.1: Error between the computed and extrapolated values of turbine efficiency, $\frac{\eta_{tt}-\eta_{tt,real}}{\eta_{tt,real}}$, as a function of grid maximum spacing, h_{grid}^{max}.

[1] One coarser, and two finer than the used one.

A.3. Diffuser Convergence Study: details

The computation of the diffuser case is more costly as it involves the stator, rotor, and diffuser domains. For this reason, the study was kept at a minimum with only 4 grids[1]. The number of elements in the diverging sections for these grids is reported in Table A.1. The different values of C_p and K_{loss} at the outlet are reported in the main text (Figure 3.9). Due to the characteristics of the grid and the refinement strategy, there is no meaningful way of obtaining a characteristic cell length: In the refinement steps only the diverging section was treated, so the extension outlet cells are always the biggest and they do not affect the reported results. Similarly, smallest cells are always in the boundary layer and influenced by the constraint $y^+ \approx 1$. Finally, mean cell volume is polluted by the extension region. Using a metric such as $\overline{h} = \sqrt[3]{\frac{Volume\ diverging\ section}{\#\ nodes\ diverging\ section}}$ did not provide satisfactory results, and thus the order of convergence and the extrapolated values are unknown.

It is relevant that C_p is almost independent of grid spacing (Figure 3.9). Note that it is this parameter what drives the turbine enhancement, Section 2.4. The changes in k_{loss} appear to be very big, but they are small when compared to the value of C_p or ξ.

Another pertinent question is the effect at different locations of the diffuser. This is shown in Figure A.2. It is possible to see how the used grid and the finer ones are practically indistinguishable. The coarser grid is slightly different. The plot at the right shows the difference with the finest grid in every axial position. Note how the biggest difference is located where the sudden expansion is: there are a lot of steep gradients and more cells are needed to properly solve this region of the flow-field.

Figure A.3 shows the differences in loss coefficient. Again, the coarse grid does not follow the proper trends and the two finer grids are practically overlapped. The grid used in the study is slightly too coarse to accurately predict k_{loss}. Interestingly enough, all 3 fine grids correctly predict K_{loss} at the inlet of the diffuser. This gives confidence in predicting mixing losses and the most direct turbine-diffuser interactions.

Table A.1: Number of elements in the diverging section for each diffuser grid.

Name	*Coarser*	*Used*	*Refinement 1*	*Refinement 2*
Number of elements	14 700	37 400	87 000	212 000

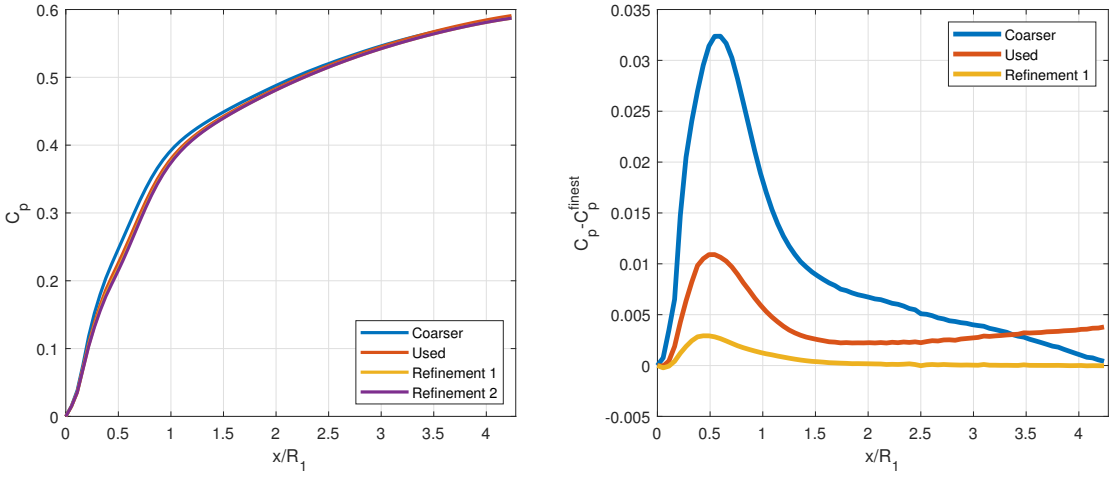

Figure A.2: Evolution of C_p along the diffuser for different grid spacings.

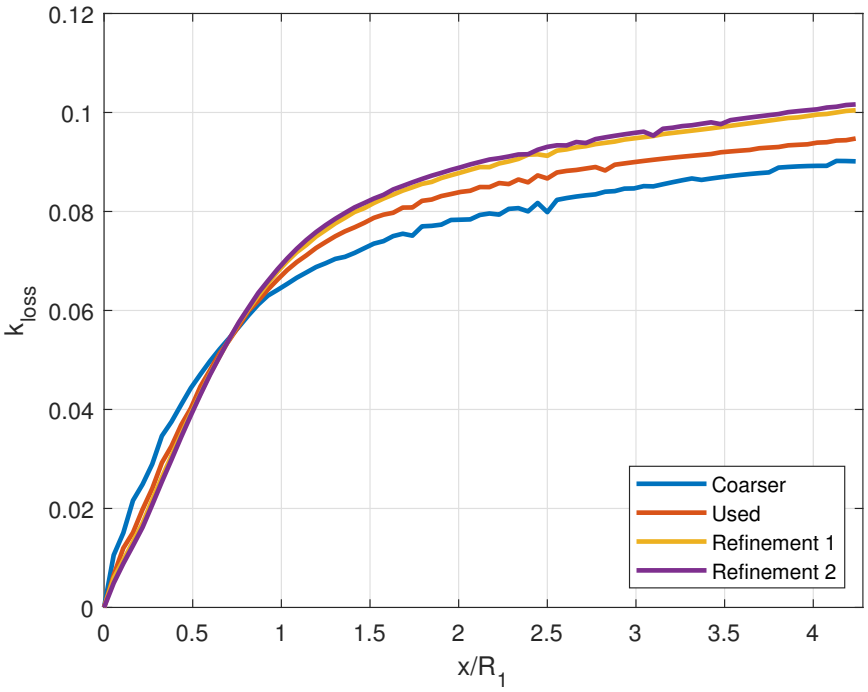

Figure A.3: Evolution of k_{loss} along the diffuser for different grid spacings.